Chapter 14
Dynamics of Saturn's Dense Rings

Jürgen Schmidt, Keiji Ohtsuki, Nicole Rappaport, Heikki Salo, and Frank Spahn

Abstract The Cassini mission to Saturn opened a new era in the research of planetary rings, bringing data in unprecedented detail, monitoring the structure and properties of Saturn's ring system. The question of ring dynamics is to identify and understand underlying physical processes and to connect them to the observations in terms of mathematical models and computer simulations. For Saturn's dense rings important physical processes are dissipative collisions between ring particles, their motion in Saturn's gravity field, their mutual self-gravity, and the gravitational interaction with Saturn's moons, exterior to or embedded in the rings.

The importance of the rings' self-gravity became strikingly clear from the identification of gravitational wakes in Cassini data nearly everywhere in the A and B rings. Self-gravity wakes imply that the rings are in a flat, dynamically cold state, ring particles colliding very dissipatively, being densely packed in the ring plane, continuously forming transient gravitationally bound opaque clumps, that are disrupted again by shear on the orbital timescale. Current mathematical dynamical models usually treat self-gravity in an approximate manner, which does not lead a wake state.

The dense packing of ring particles, in turn, strongly influences the collisional dynamics, since the mean free path of the particles is then comparable to or smaller than the particle size. This leads to a strong nonlocal component of pressure and momentum transport, which determines the viscous evolution of the rings, the damping of density waves, as well as the stability properties of the ring's flow. A strong nonlocal contribution to viscosity is, for instance, favorable for viscous overstability, leading to axisymmetric waves of about 100 m wavelength. Such wavelike perturbations in the ring's opacity, consistent with overstability, are seen in Cassini stellar and radio occultations.

A classical topic of ring dynamics is the interaction of moons and rings. On the one hand, there are exterior moons with resonances in the rings, creating numerous density and bending waves. With the large sets of Cassini occultation and imaging data, improved estimates of the ring surface mass density and viscosity are obtained from fits of the observations to dynamical models. On the other hand, the embedded moons Pan and Daphnis open the Encke and Keeler gaps, respectively, and moonlets in the rings, too small to open a circumferential gap, are found to produce a characteristic propeller structure.

Comparison between theoretical studies and Cassini observations of thermal emission from the rings provides constraints on spin rates of ring particles, which are otherwise not directly observable. The size distribution of particles and small moonlets embedded in the rings, together with the observed shapes and internal densities of small moons just exterior to the rings, underline the importance of accretion and fragmentation for the dynamical evolution of Saturn's ring system.

14.1 General Theory and Recent Advances

In this section we outline elements of the theoretical modelling of dense planetary rings. We start with a basic description of the physical processes that crucially influence the steady state properties of the rings – dissipative collisions and shear – and discuss the importance of the elastic properties of ring particles. Section 14.1.3 then gives an introduction to self-gravity in Saturn's rings.

J. Schmidt and F. Spahn
Universität Potsdam, Germany

K. Ohtsuki
University of Colorado, CO, USA

N. Rappaport
JPL, Pasadena, CA, USA

H. Salo
University of Oulu, Finland

AQ1

M. Dougherty et al. (eds.), *Saturn from Cassini-Huygens*,
DOI 10.1007/978-1-4020-9217-6_14,

14.1.1 Steady-State of a Dense Non-gravitating Particle Disk

The dynamics of an unperturbed planetary ring consisting of macroscopic particles is basically determined by inelastic binary particle collisions and the shearing motion in the gravitational field of the central planet. In this section we discuss how these processes determine the energy budget of a dense planetary ring.

14.1.1.1 Dissipative Collisions

Inelastic physical collisions of the ring particles continuously dissipate energy from the particles' random motion. The dissipation can be quantified by the normal coefficient of restitution ε_n, defined as the ratio of the post-collisional to pre-collisional normal component of the relative velocity of the colliding particles[1]. Particles will collide with an impact speed on the order of the velocity dispersion c of the ring so that the kinetic energy (per unit mass) dissipated in a single collision can be estimated as $c^2\left(1-\varepsilon_n^2\right)$. The rate of collisional energy loss is then

$$\left.\frac{\partial c^2}{\partial t}\right|_{loss} \propto -\Omega_c c^2\left(1-\varepsilon_n^2\right) \tag{14.1}$$

with the collision frequency Ω_c. In dilute planetary rings (where $c \gg D\Omega$, with the dominant particle diameter D), we have

$$\Omega_c \approx 3\Omega\tau, \tag{14.2}$$

with Kepler frequency $\Omega(r) = \sqrt{GM_{plan}/r^3}$ (angular velocity on a circular orbit at distance r from a planet of mass M_{plan}, where G is the gravitational constant). This expression does not depend on the velocity dispersion, although in principle $\Omega_c \propto n_{space} D^2 c$, where n_{space} is the ring particles' space number density. The explicit c dependence cancels out, however, since the space density for a given τ is inversely proportional to c, due to collisional coupling between horizontal and vertical motions. For very flattened systems ($c \sim D\Omega$) the impact frequency can exceed significantly the value implied by Eq. 14.2 (Salo 1992b).

14.1.1.2 Shear Stress

In viscous shear flow, energy is transferred from the systematic motion to the random motion of the particles. There is a transport of angular momentum (related to this energy transfer), i.e. momentum in flow direction is transported perpendicular to the flow. In a system of particles with finite diameter D there are two different modes of transport, local and nonlocal, both connected to collisions and coupling to the shear rate.

In a local frame rotating at distance r_0 around the planet with Kepler frequency $\Omega(r_0)$, the Keplerian orbital velocity reads $v = [\Omega(r) - \Omega(r_0)]\, r$. Introducing $x = r - r_0$ this may be approximated as

$$v = -\frac{3}{2}\Omega(r_0)\, x + O\left[(x/r_0)^2\right] \tag{14.3}$$

and the shear rate s reads

$$s \equiv \frac{\partial v}{\partial x} = -\frac{3}{2}\Omega(r_0)\,. \tag{14.4}$$

The rate of gain of kinetic energy (per unit mass) is given by the kinematic viscosity ν and shear rate s as

$$\left.\frac{\partial c^2}{\partial t}\right|_{gain} \propto \nu s^2 \tag{14.5}$$

Local Shear Viscosity

Local shear stress is connected to the particles' radial random motions (Fig. 14.1a). This kind of momentum transport is labeled 'local' since it is not necessary to distinguish the particle positions in a collision. Let an imaginary line L separate the flow radially into an inner and outer region (Fig. 14.1). When particles cross the line between collisions (Fig. 14.1a) they carry across the line the mean momentum per particle of the ring region they come from. Since (due to shear) the mean velocity at the new position is slightly different, the particles have, on average, a small amount of excess momentum with respect to the surrounding particles, which is transferred to the flow in the subsequent collisions. In this way, neighboring ring regions are effectively coupled by a drag force: The inner part of the ring tends to accelerate the outer part, and vice versa.

For the local kinematic shear viscosity Goldreich and Tremaine (1978c) derived the formula

$$\nu_l = \frac{c^2}{\Omega}\frac{\tau}{1+\tau^2}. \tag{14.6}$$

For large optical depth $\nu_l \propto 1/\tau$, which is reminiscent of the density dependence $\nu \propto 1/\rho$ of hydrodynamics (Chapman and Cowling 1970). For low optical depth we have $\nu_l \propto \tau$. This deviation from the hydrodynamic density dependence results from the motion in the central gravity field: In a dilute system the radial excursions of a particle are limited by the

[1] In addition, kinetic energy may be lost in surface friction, reducing the tangential relative velocity between colliding particles and transferring energy of random motions into the particles' spin and vice versa. For simplicity we restrict the discussion here on normal restitution.

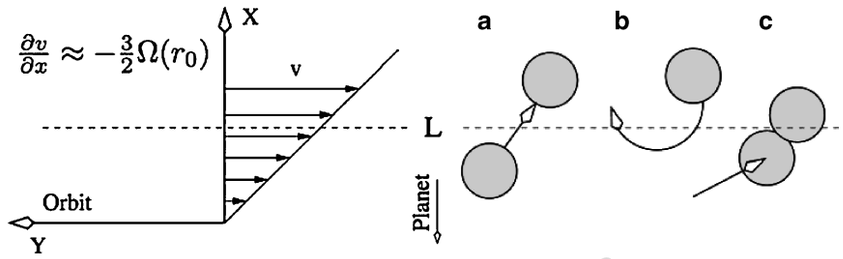

Fig. 14.1 *Left panel*: Velocity profile of the ring in a local frame co-rotating at distance r_0 from the planet. The X-axis points radially outward, the Y-axis in the direction of orbital motion. *Right panel*: Typical particle paths and collisions. (**a**) Momentum transport across the (*dashed*) imaginary line L by a crossing particle (local transport). (**b**) Particle moving on an epicycle (no transport). (**c**) Momentum transport across L in a collision (nonlocal transport)

epicyclic length (Fig. 14.1b), which reduces the momentum transport $\propto \tau$.

Non-Local Shear Viscosity and Pressure

In a dense collisional system the mean free path is on the order of the particle dimensions and the momentum transferred by a collision (Fig. 14.1c) over the distance of one particle diameter is important. Describing this process statistically (Shukhman 1984; Araki and Tremaine 1986), the positions of particle centers in a collision must be distinguished, and hence the corresponding stress is labeled *nonlocal*.

From mean-free path arguments the nonlocal kinematic shear viscosity can be estimated to be on the order of (Shukhman 1984)

$$\nu_{nl} = \Omega D^2 \tau. \tag{14.7}$$

Consider the transport of momentum across the dashed line in Fig. 14.1, counting only binary collisions where particle centers are on opposite sides of the line (Fig. 14.1c). The number of particles crossing the line per unit length and unit time is roughly $J = (\sigma/m)\, c$, with surface mass density σ and particle mass m. To count only those particles actually intersected by the line, we multiply this particle flux density by the factor D/l, where l is the mean free path $l = c/\Omega_c$. The maximal momentum transported over a radial distance of one particle diameter is $\Delta p = mDs$. Given the (vertically integrated) shear stress by $P_{xy} = J\Delta p$ and identifying it with the hydrodynamic relation $P_{xy} = \sigma \nu_{nl} s$, we obtain Eq. 14.7. The significance of nonlocal viscosity for planetary rings was first pointed out by Brahic (1977). Similar arguments lead to an order of magnitude estimate for the nonlocal (vertically integrated) pressure as

$$p_{nl} = \sigma \tau c \Omega D. \tag{14.8}$$

Total Shear Viscosity and Pressure

Summing up the local and non-local viscosities we obtain

$$\frac{\nu}{\Omega D^2} = k_1 \left(\frac{c}{\Omega D}\right)^2 \frac{\tau}{1+\tau^2} + k_2 \tau, \tag{14.9}$$

with constants k_1, k_2, and with the local pressure $p = \sigma c^2$ we obtain the total pressure

$$\frac{p/\sigma}{(\Omega D)^2} = \left(\frac{c}{\Omega D}\right)^2 + \frac{c}{\Omega D}\tau. \tag{14.10}$$

14.1.1.3 Steady State and Thermal Stability

Summing up the cooling (Eq. 14.1) and heating (Eq. 14.5) rates one obtains the energy budget of the ring particle ensemble

$$\frac{\partial c^2}{\partial t} = s^2 \left[k_1 \frac{c^2}{\Omega} \frac{\tau}{1+\tau^2} + k_2 \Omega D^2 \tau\right] - k_3 \Omega \tau \left(1-\varepsilon_n^2\right) c^2 \tag{14.11}$$

where k_1, k_2, k_3 are positive dimensionless constants (e.g. Stewart et al. 1984; Morishima and Salo 2006). For a velocity independent coefficient of restitution this equation has the fixed point solution

$$\left(\frac{c^*}{\Omega D}\right)^2 = \frac{k_2 (s/\Omega)^2 \left(1+\tau^2\right)}{k_3 \left(1-\varepsilon_n^2\right)\left(1+\tau^2\right) - k_1 (s/\Omega)^2} \tag{14.12}$$

which is stable for

$$\varepsilon_n < \varepsilon_{crit} = \sqrt{1 - \frac{k_1}{k_3} \frac{(s/\Omega)^2}{1+\tau^2}} \tag{14.13}$$

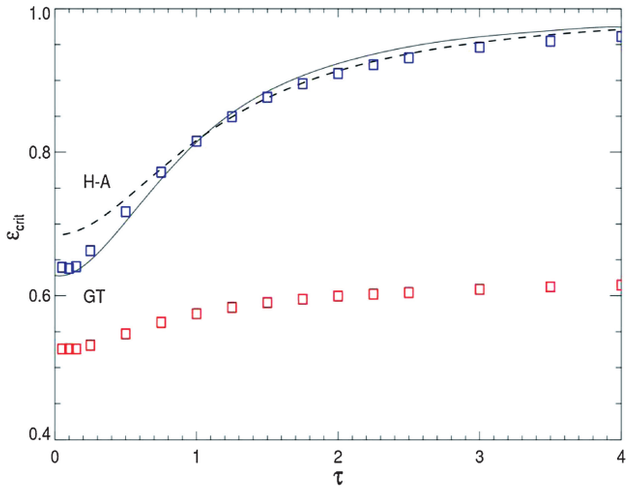

Fig. 14.2 Theoretical thermal stability boundary $\varepsilon_{crit}(\tau)$, from Hämeen-Anttila (1978); Goldreich and Tremaine (1978c), who used different approximations in the evaluation of the collision integrals. Also shown are effective steady-state values of ε_n from two series of simulations, performed with velocity-dependent coefficient of restitution: upper points correspond to a 'hot' simulation with velocity dispersion $c \gg D\Omega$ (this dilute 'mass-point' limit approximates the assumptions behind the theoretical curves), while the lower points correspond to simulations performed with the Bridges et al. (1984) elasticity formula. The average ε_n in simulations is measured by weighting each impact with the square of the normal component of impact velocity, $< \varepsilon_n {v_n}^2 > / < {v_n}^2 >$. Redrawn from Salo

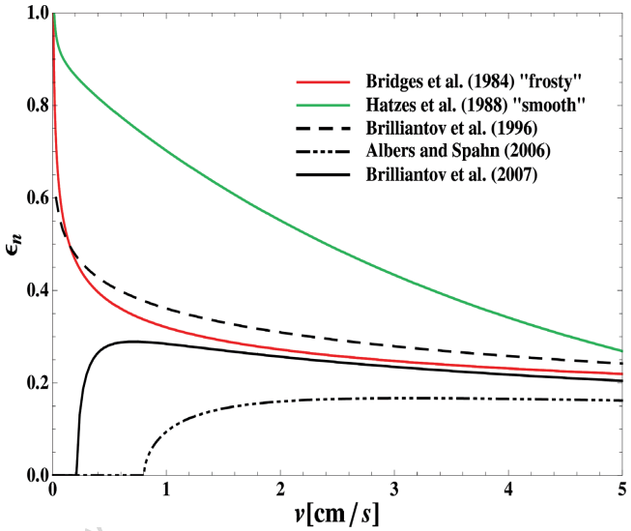

Fig. 14.3 The normal coefficient of restitution from theoretical models (black curves) and measurements for frosty ice particles (radius 2.75 cm, *red curve*) by Bridges et al. (1984) and larger ice particles with compacted frost surface-layers (radius 20 cm, *green curve*) by Hatzes et al. (1988). The triple-dotted dashed curve shows results from visco-elastic models including adhesion (Albers and Spahn, 2006) and the thick solid curve is derived from an extension of this model (Brilliantov et al., 2007). The dashed curve is from a visco-elastic model (Brilliantov et al., 1996)

and unstable otherwise. This critical value ε_{crit} was first derived by Goldreich and Tremaine (1978c) and an equivalent expression (Fig. 14.2) was given by Hämeen-Anttila (1978). In systems with constant $\varepsilon_n < \varepsilon_{crit}$ the particles establish a thermal equilibrium mainly due to the non-local viscous gain. This steady state corresponds to a flattened system with a geometric thickness of a few particle diameters only and a velocity dispersion $c \sim \Omega D$. For $\varepsilon_n > \varepsilon_{crit}$ the local viscous gain always dominates the dissipation, no energy balance can be achieved, and the system inevitably disperses via continuously growing random velocities. With increasing τ the reduced mean free path between impacts limits the local viscous gain and ε_{crit} increases (Fig. 14.2). For rough particles tangential friction adds to the dissipation and ε_{crit} is shifted closer to unity (Shukhman 1984; Araki 1988).

For realistic materials ε_n is a decreasing function of impact velocity (Fig. 14.3), or, on average, of velocity dispersion. In this case the stability behavior of Eq. 14.11 is different. Systems with $\varepsilon_n(c) > \varepsilon_{crit}$ will heat up, so that $\varepsilon_n(c)$ decreases until an equilibrium of collisional energy loss and viscous gain is established (Goldreich and Tremaine 1978c). Due to non-local shear stress, however, this equilibrium value of $\varepsilon_n(c)$ is generally smaller than ε_{crit}. Only mass point systems ($D \to 0$) can establish $\varepsilon_n(c) = \varepsilon_{crit}$. The exact value of the steady-state velocity dispersion is determined by the dependence of ε_n on v, and, at least in principle, a ring's configuration can range from a thick multilayer of particles to a near monolayer ring. In the latter case the steady-state is in practice indistinguishable from the case of constant $\varepsilon_n < \varepsilon_{crit}$.

14.1.1.4 Mechanical Properties of Particles

The coefficient of restitution of ice particles was determined experimentally at the low temperature and pressure appropriate for the planetary ring environment. The laboratory measurements by Bridges et al. (1984) and Hatzes et al. (1988) indicated that the normal restitution coefficient ε_n decreases monotonically with the normal component of impact speed v_n, as required for thermal balance of the ring (Section 14.1.1.3). Measurements yielded the dependencies (Fig. 14.3)

$$\varepsilon_n(v_n) = (v_n/v_c)^{-0.234}, \text{ (frosty)} \tag{14.14}$$

$$\varepsilon_n(v_n) = 0.90\exp\{-0.22\left(v_n/1\,\mathrm{cm\,s^{-1}}\right)\} + 0.01\left(v_n/1\,\mathrm{cm\,s^{-1}}\right)^{-0.6}, \text{(smooth)}. \tag{14.15}$$

Relation 14.14 was widely used in computer simulations of planetary rings. It was obtained for frosty ice

spheres of radius 2.75 cm (Bridges et al. 1984) with $v_c = 0.0077\,\mathrm{cm\,s^{-1}}$ ($\equiv v_B$) and it corresponds to fairly inelastic impacts, or, to very flattened rings. The relation 14.15 was obtained for ice particles (radius 20 cm) covered by a compacted frost layer (Hatzes et al. 1988). We have chosen this formula from the results of Hatzes et al. (1988) to display the effect of more elastic particles in the following.

The functional dependence $\varepsilon_n\,(v_n)$ is sensitive to the surface properties of the particles. Higa et al. (1996, 1998) measured ε_n for a much wider range of impact velocities (1–1000 $\mathrm{cm\,s^{-1}}$). They found that fracture of the ice ball occurs and ε_n decreases significantly when v_n is larger than a critical value. Experiments with glancing collisions showed that tangential velocities are decreased by about 10% for collisions at $v_n \geq 0.1\,\mathrm{cm\,s^{-1}}$ (Supulver et al. 1995).

Impact experiments under micro-gravity suggest that normal and tangential rebound velocities are significantly smaller if ring particles are covered by regolith (Colwell and Taylor 1999; Colwell 2003). If ring particles are covered by a frost layer cohesive forces may even cause sticking of colliding particles at low-velocity impacts (Hatzes et al. 1991; Bridges et al. 1996; Supulver et al. 1997).

Considerable effort has been invested to derive theoretical expressions for the restitution coefficient. Dilley (1993) proposed an empirical damped oscillator model to describe dissipative collisions, which can be tuned to reproduce, for instance, the experimental results for the Bridges et al. (1984) velocity-dependence of ε_n, as well as the mass-dependence determined in later experiments (Dilley 1993; Dilley and Crawford 1996). Brilliantov et al. (1996) generalized the nonlinear elastic collision model by Hertz (1882) to the case of visco-elastic dissipation. Adjusting one single parameter, characterizing the viscous properties of the particle, the model reproduces the measurements of Bridges et al. (1984) fairly well (Fig. 14.3). Albers and Spahn (2006) included cohesive forces between elastic solids in contact (Johnson et al. 1971) in the visco-elastic model (Brilliantov et al. 1996). Their ε_n is consistent with Bridges et al. (1984) for high impact velocities, where cohesion is negligible. For low impact speeds the cohesive force becomes dominant and particles stick for impact velocities smaller than a critical value (Albers and Spahn 2006; Brilliantov et al. 2007) as observed in experiments.

Although the actual mechanical properties of particles in Saturn's rings are poorly known, comparison between observations and dynamical investigations suggests that they are fairly dissipative and under-dense (Section 14.1.3).

14.1.1.5 Steady State Dynamical Properties

A difference in the elastic properties of particles is reflected in the predicted steady-state properties of the ring, and it leads to qualitative differences in the stability properties of the system. A system of fairly elastic particles, dynamically hot at low optical depth τ, exhibits a large reduction of the steady-state velocity dispersion as the optical depth increases, basically because the local viscous gain becomes less effective as the mean free path between impacts is reduced. In the left panel of Fig. 14.4 this is illustrated in terms of the effective geometric thickness: for the'smooth' particle model (Eq. 14.15, Fig. 14.3) the thickness may drop by as

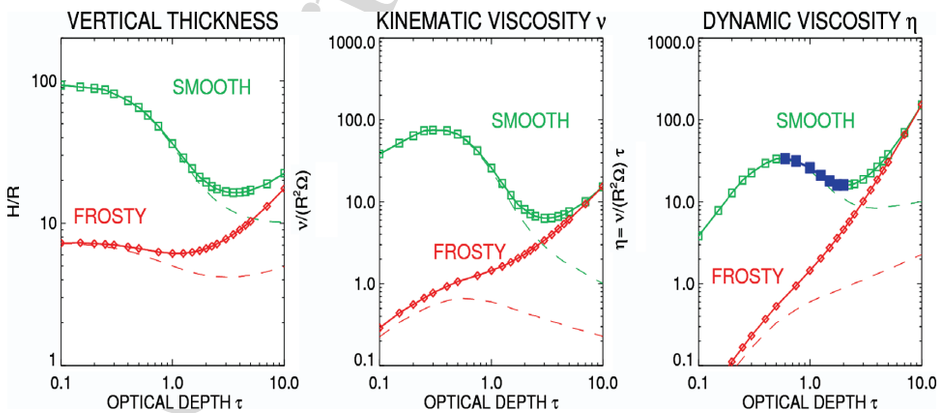

Fig. 14.4 Steady-state geometric thickness and viscosity for the 'smooth' and 'frosty' elasticity models (Eqs. 14.14 and 14.15), Fig. 14.3). Left frame: Symbols show the simulated effective geometric thickness $H = \sqrt{12\,\langle z^2\rangle}$, in units of particle radius R (H corresponds to the full thickness of a homogeneous layer with the same vertical dispersion as the actual distribution). The dashed line is the effective thickness estimated from the vertical velocity dispersion, $\sqrt{12}c_z/\Omega$; in the case of low filling factor these two measures are identical. Middle frame: Kinematic viscosity ν; the contribution from local viscosity is shown separately (*dashed lines*). Right frame: Dynamic viscosity $\tau\nu$ (τ is used instead of σ since surface density is unspecified in non self-gravitating simulations). Filled blue squares indicate the τ-regime with negative $\partial\nu\tau/\partial\tau$, susceptible to viscous instability (Section 14.2.2). A particle size $R = 1$ m and Saturnocentric distance $a = 100{,}000$ km are assumed. Adapted from Salo

much as a factor of five as optical depth increases from zero to above unity. On the other hand, the 'frosty' particle model (Eq. 14.14, Fig. 14.3) leads to a nearly constant velocity dispersion. The different steady-state velocity dispersion alters the local and, to a lesser degree, non-local contribution to viscosity. For a cool system the dynamic viscosity, given by the product $\tau\nu$, is monotonically increasing. For a hot system it decreases for some range of optical depths (marked by filled squares in Fig. 14.4), if the aforementioned reduction of ν_l with τ is strong enough. A negative $\mathrm{d}(\tau\nu)/\mathrm{d}\tau$ should lead to viscous instability (Section 14.2.2), whereas a strong enough positive slope may indicate overstability (Section 14.2.1).

Since the mechanical properties of ring particles are uncertain, all equilibrium states sketched above might be possible in different parts of Saturn's ring system. For ring particles covered with regolith one may expect even smaller ε_n values than those obtained in the Bridges et al. (1984) laboratory experiments. In any case, at very large optical depth the simulated steady-state properties in non-gravitating systems with viscosity are dominated by effects of finite particle size and are practically independent of the elastic model.

In systems with a particle size distribution the steady-state velocity dispersion of smaller particles generally exceeds the one of larger particles, implying a larger vertical scale height for small particles (e.g. Cuzzi et al. 1979a, b; Salo 1992b; Salo and Karjalainen 2003). For low optical depth rings this was shown by solving the evolution equation for the velocity dispersion (Ohtsuki 1999, 2006b)

$$\frac{dc_m^2}{dt} = \int n_s\left(m'\right)\left\{C_{VS} + \left(m'c_{m'}^2 - mc_m^2\right) C_{DF}\right\} dm', \tag{14.16}$$

where c_m and $n_s\,(m)$ are the velocity dispersion and surface number density of particles with mass m, and C_{VS} and C_{DF} are the rate coefficients related to the viscous stirring and dynamical friction due to inelastic collisions (and gravitational encounters in the case of gravitating particles). Owing to the contribution of viscous stirring and the effect of inelastic impacts, the system remains far from energy-equipartition: for example for the 'frosty' elasticity model the velocity dispersion of the smallest particles is at most a few times larger than for the largest ones, regardless of the width of the size-distribution (Salo 1992b). More elastic particles allow for a wider range of velocity dispersions, the maximum ratio still staying below about five. For a system with extended size size distribution, similar to the one inferred from observations, the dynamics is governed by the largest particles. In this case the overall velocity dispersions scale proportionally to that particle size, as in the case of identical particles. The size distribution and dynamical factors affecting its evolution are discussed in more detail in Section 14.4.

14.1.2 Balance Equations for Dense Rings

14.1.2.1 Kinetic Theory

Kinetic theory describes the evolution of the local velocity distribution function of an ensemble of particles in terms of the Boltzmann equation (Chapman and Cowling 1970) or a suitable generalization of it, like Enskog's theory of hard sphere gases. The kinetic equation can be derived from Liouville's theorem (Binney and Tremaine 1987; Resibois and DeLeener 1977), appearing as the leading equation in a hierarchy of equations describing n-particle distribution functions in phase space and neglecting correlations between particle pairs. Taking moments of the kinetic equation gives a set of balance equations for particle number density, momentum, and the components of the pressure tensor (see e.g. Goldreich and Tremaine (1978c); Araki and Tremaine (1986)).

Kinetic theory allows us to incorporate the full complexity of the dynamics of a planetary ring in a statistical description, such as the effects of the motion of ring particles on curved orbits between inelastic collisions, their finite size, the anisotropy of the velocity dispersion, and in principle also coagulation and fragmentation of the ring particles.

The first approach to extend kinetic theory to a system of inelastically colliding particles was undertaken by Trulsen (1972), aiming at a description of clustering and possible focusing of streams of inelastic grains in a protoplanetary disk. Goldreich and Tremaine (1978c) investigated the steady state properties of a disk consisting of point masses, assuming a (triaxial) Gaussian velocity distribution. In this limit they derived the relation between the coefficient of restitution of the particles and optical depth of the disk shown in Fig. 14.2 and the expression given by Eq. 14.6 for the local viscosity of the ring.

Shukhman (1984) included effects of the finite size of particles in the kinetic description of a steady state ring. The importance of such effects had been noted by Brahic (1977) in his collisional ring simulations. In the collision integrals Shukhman (1984) explicitly took into account the difference of the positions of particle centers in the moment of a collision. He derived an expression for the nonlocal viscosity (Eq. 14.7) and described how the disk settles into a nonlocal equilibrium with a vertical thickness on the order of only a few particle diameters (see Eq. 14.12). In addition, in Shukhman's work rotational degrees of freedom of ring particles and surface friction are incorporated.

Shu and Stewart (1985) used a Krook collision term to avoid the mathematical complexity of the solution of the collision integrals. In this way they obtained a closed solution for the pressure tensor of an unperturbed planetary ring. The enhancement of collision frequency in dense disks is pointed out in their work.

Araki and Tremaine (1986) extended the theory of Goldreich and Tremaine (1978c) and Shukhman (1984) for the steady state of a planetary ring in the spirit of Enskog's kinetic theory of hard spheres (Chapman and Cowling 1970). This goes beyond Shukhman's approach in that it also takes into account the finite volume occupied by particles, limiting the space available for the particles' motion, in terms of the Enskog factor in the collision integral. This effect leads in a dense system to a drastic increase of the collision frequency. Araki (1988) investigated the effect of particle spin and surface friction in a kinetic treatment of dilute rings and Araki (1991) presented a combined kinetic theory for dense and spinning particle disks.

Araki (1991) analytically reduced the collision integrals to a fourfold integration that had to be carried out numerically, which made an application to dynamical problems infeasible. Further progress was made by Latter and Ogilvie (2006) who developed a kinetic theory for dilute rings carrying out all collision integrals analytically. Their work was extended by Latter and Ogilvie (2008) to dense systems, studying stability properties of a dense ring.

An alternative statistical description of planetary rings was formulated in a series of papers by Hämeen-Anttila (Hämeen-Anttila 1978, 1981, 1982; Hämeen-Anttila and Salo 1993) improving and generalizing an earlier approach (Hämeen-Anttila 1975, 1976, 1977a, b). It uses a kinetic equation of Boltzmann type for the description of the evolution of the one-particle phase space distribution function, in a similar manner as gas-kinetics. Hämeen-Anttila gives analytical solutions for the collision integrals, where necessary in terms of appropriate approximations. The theory presented in Hämeen-Anttila and Salo (1993) can treat systems of non-identical, rotating, inelastic particles in a Keplerian field. Arbitrary (velocity dependent) collision laws can be applied to describe translational and rotational energy losses in an impact. The effect of self-gravity is taken into account in a self-consistent manner in the local vertical gravity field of the disk and in its effect on close particle encounters. In principle the theory can treat the average effect of particle surface irregularities stochastically and it is formulated so that it can be extended to describe particle fragmentation and coagulation. The biggest advantage is that the balance equations for mass, stress, and scale hight of the ring, are given analytically as partial differential equations. Thus, the theory can be applied to investigate the dynamical evolution of a planetary ring.

14.1.2.2 Hydrodynamics

The dynamic equations resulting from kinetic theory are of great complexity. For instance the kinetic approach developed by Goldreich and Tremaine (1978c), Araki and Tremaine (1986), and Araki (1988) (1991) gives insights into steady state properties of a planetary ring, but the important question of spatial and temporal evolution is not addressed. The approaches by Latter and Ogilvie (2008) and Hämeen-Anttila and Salo (1993) allow the application to dynamical problems but the equations are so involved that even the solution of small-scale dynamical problems would require a large computational effort.

Hence, for simplicity hydrodynamic models are often employed to investigate the dynamical evolution of rings. The hydrodynamic equations, introduced below, describe the balances of mass, momentum, and energy. They can be derived from the moment equations of kinetic theory (Chapman and Cowling 1970; Stewart et al. 1984), relating the stress and the heat flow to the gradients of velocity and temperature via the concept of the transport coefficients. In dynamical studies parameterizations, suitable for a planetary ring, for the density dependence of these transport coefficients and the equation of state are often employed. These are motivated by simulations (Wisdom and Tremaine 1988; Salo et al. 2001; Schmidt and Salo 2003) or kinetic theory (Goldreich and Tremaine 1978c; Shukhman 1984).

For reference we give here vertically integrated hydrodynamic balance equations in cylindrical coordinates (r, φ) for a vertically thin planetary ring with surface density σ, planar components u_r, u_φ of velocity, and the granular temperature T (energy of particles' random motion)[2]:

$$\left(\frac{\partial}{\partial t} + u_r \frac{\partial}{\partial r} + \frac{u_\varphi}{r}\frac{\partial}{\partial \varphi}\right)\sigma = -\sigma\,\nabla\cdot\vec{u} \tag{14.17}$$

$$\left(\frac{\partial}{\partial t} + u_r \frac{\partial}{\partial r} + \frac{u_\varphi}{r}\frac{\partial}{\partial \varphi}\right)u_r - \frac{u_\varphi^2}{r} = -\frac{\partial \Phi_{Planet}}{\partial r} - \frac{\partial \Phi_{Disk}}{\partial r} - \frac{1}{\sigma}\left(\nabla\cdot\hat{\mathbf{P}}\right)_r \tag{14.18}$$

$$\left(\frac{\partial}{\partial t} + u_r \frac{\partial}{\partial r} + \frac{u_\varphi}{r}\frac{\partial}{\partial \varphi} + \frac{u_r}{r}\right)u_\varphi = -\frac{1}{r}\frac{\partial \Phi_{Disk}}{\partial \varphi} - \frac{1}{\sigma}\left(\nabla\cdot\hat{\mathbf{P}}\right)_\varphi \tag{14.19}$$

$$\frac{3}{2}\sigma\left(\frac{\partial}{\partial t} + u_r \frac{\partial}{\partial r} + \frac{u_\varphi}{r}\frac{\partial}{\partial \varphi}\right)T = -\hat{\mathbf{P}} : \nabla\vec{u} - \nabla\cdot\vec{q} - \Gamma, \tag{14.20}$$

[2] The temperature $T = \mathrm{Tr}\,\hat{\mathbf{C}}/3$ is defined as the trace of the velocity dispersion tensor $\hat{\mathbf{C}} = \langle c; \overrightarrow{\ } c; \overrightarrow{\ } \rangle$, where $\vec{c} = \vec{v}\text{-}\vec{u}$, $\vec{u}$ is the hydrodynamic velocity and $\vec{v}$ the instantaneous velocity of a ring particle (Chapman and Cowling, 1970). The average $\langle\cdot\rangle$ is over the particle velocity distribution function $f(\vec{v})$.

where

$$\nabla \cdot \vec{u} = \frac{1}{r}\frac{\partial\left(r u_r\right)}{\partial r} + \frac{1}{r}\frac{\partial u_\varphi}{\partial \varphi} \tag{14.21}$$

$$\left(\nabla \vec{u}\right)_{rr} = \frac{\partial u_r}{\partial r}, \quad \left(\nabla \vec{u}\right)_{\varphi\varphi} = \frac{1}{r}\frac{\partial u_\varphi}{\partial \varphi} + \frac{u_r}{r} \tag{14.22}$$

$$\left(\nabla \vec{u}\right)_{r\varphi} = \frac{\partial u_\varphi}{\partial r}, \quad \left(\nabla \vec{u}\right)_{\varphi r} = \frac{1}{r}\frac{\partial u_r}{\partial \varphi} - \frac{u_\varphi}{r} \tag{14.23}$$

$$\left(\nabla \cdot \hat{\mathbf{P}}\right)_r = \frac{1}{r}\frac{\partial\left(r P_{rr}\right)}{\partial r} + \frac{1}{r}\frac{\partial P_{r\varphi}}{\partial \varphi} - \frac{P_{\varphi\varphi}}{r} \tag{14.24}$$

$$\left(\nabla \cdot \hat{\mathbf{P}}\right)_\varphi = \frac{1}{r}\frac{\partial\left(r P_{r\varphi}\right)}{\partial r} + \frac{1}{r}\frac{\partial P_{\varphi\varphi}}{\partial \varphi} + \frac{P_{r\varphi}}{r} \tag{14.25}$$

$$\nabla \cdot \vec{q} = \frac{1}{r}\frac{\partial\left(r q_r\right)}{\partial r} + \frac{1}{r}\frac{\partial q_\varphi}{\partial \varphi}. \tag{14.26}$$

The disk's self-gravity potential Φ_{Disk} couples to the surface mass density through Poisson's equation

$$\frac{1}{r}\frac{\partial}{\partial r}\left(r\frac{\partial \Phi_{Disk}}{\partial r}\right) + \frac{1}{r^2}\frac{\partial^2 \Phi_{Disk}}{\partial \varphi^2} + \frac{\partial^2 \Phi_{Disk}}{\partial z^2} = 4\pi G\sigma\delta\left(z\right), \tag{14.27}$$

and the gravitational potential of the planet is denoted by Φ_{Planet}. In Eqs. 14.17–14.26 $\hat{\mathbf{P}}$ is the vertically integrated symmetric pressure tensor and $\vec{q}$ the heat flux. The term Γ accounts for the cooling due to dissipative collisions (see Section 1.1.1, Salo et al. (2001)). It does not appear in the hydrodynamic description of molecular gases, but it is common for granular flows (Brilliantov and Pöschel 2004).

If specifically $\hat{\mathbf{P}}$ is of Newtonian form then

$$P_{rr} = p - 2\eta\frac{\partial u_r}{\partial r} + \left(\frac{2}{3}\eta - \xi\right)\nabla \cdot \vec{u} \tag{14.28}$$

$$P_{r\varphi} = -\eta\left(\frac{\partial u_\varphi}{\partial r} + \frac{1}{r}\frac{\partial u_r}{\partial \varphi} - \frac{u_\varphi}{r}\right) \tag{14.29}$$

$$P_{\varphi\varphi} = p - 2\eta\left(\frac{1}{r}\frac{\partial u_\varphi}{\partial \varphi} + \frac{u_r}{r}\right) + \left(\frac{2}{3}\eta - \xi\right)\nabla \cdot \vec{u}. \tag{14.30}$$

Fourier's law affords

$$q_r = -\kappa_D\frac{\partial T}{\partial r}, \quad q_\varphi = -\frac{\kappa_D}{r}\frac{\partial T}{\partial \varphi}. \tag{14.31}$$

The system of Eqs. 14.17–14.20 and Eqs. 14.28–14.31 is closed by an equation of state $p = p\left(\sigma, T\right)$ and by the prescription of the dependence of the transport coefficients $\eta\left(\sigma, T\right), \xi\left(\sigma, T\right)$, and $\kappa_D\left(\sigma, T\right)$ – dynamic coefficients of shear viscosity[3], bulk viscosity, and heat conductivity – on density and granular temperature (i.e. velocity dispersion). It is important to note that for the description of a planetary ring, in general, neither the approximation of incompressibility can be adopted, nor can the transport coefficients assumed to be constant.

Further simplifying assumptions allow us to construct models that use only a part of these equations. For instance, often the approximation of an isothermal ring is applied and one deals with Eqs. 14.17–14.19 while Eq. 14.20 reduces to

$$0 = \hat{\mathbf{P}} : \nabla\vec{u} + \Gamma, \tag{14.32}$$

i.e. to the balance of collisional cooling and viscous heating, which sets the steady state velocity dispersion of the ring (Eq. 14.12). Although thermal excitations are important (Spahn et al. 2000; Salo et al. 2001; Schmidt et al. 2001) for specific problems (Section 14.2.2), isothermal models usually provide a good qualitative description of many dynamical problems in planetary rings (Ward 1981; Lin and Bodenheimer 1981; Schmit and Tscharnuter 1995; Spahn and Sremčević 2000; Spahn et al. 2000; Schmidt et al. 2001; Schmidt and Salo 2003; Tremaine 2003).

Most instability mechanisms proposed for planetary rings (Section 14.2) aim describing axisymmetric patterns on scales that are short compared to the dimensions of the ring. In this case, one can neglect curvature terms and restrict the analysis to radial perturbations, so that the isothermal Eqs. 14.17–14.19 and 14.27 read in a frame that co-rotates in the rings with local Kepler frequency $\Omega_0 \equiv \Omega\left(r_0\right)$ at a radial distance r_0 from the planet

$$\dot{\sigma} = -\left(\sigma u\right)' \tag{14.33}$$

$$\dot{u} = -uu' + 2\Omega_0 v - \frac{p'}{\sigma} + \frac{1}{\sigma}\left(\left[\frac{4}{3}\eta + \xi\right]u'\right)' - \Phi'_{Disk} \tag{14.34}$$

$$\dot{v} = -uv' - \frac{\Omega_0}{2}u + \frac{1}{\sigma}\left(\eta v'' + \eta'\left[v' - \frac{3}{2}\Omega_0\right]\right) \tag{14.35}$$

$$\frac{\partial^2 \Phi_{Disk}}{\partial r^2} + \frac{\partial^2 \Phi_{Disk}}{\partial z^2} = 4\pi G\sigma\delta\left(z\right). \tag{14.36}$$

[3] Dynamic quantities are defined as the product of the kinematic quantities and density, e.g. $\eta = \sigma\nu$, with the kinematic shear viscosity ν.

Here v is the deviation of the tangential velocity from the systematic Kepler speed (approximated by Eq. 14.3). The dots and primes denote the derivatives with respect to time and radial coordinate $r - r_0$, respectively. A further simplification results from the assumption that the dynamic bulk viscosity ξ has the same dependence on the ring's surface density as the dynamic shear viscosity η. If ξ_0, η_0 denote their constant unperturbed values then

$$\xi = \alpha\eta, \quad \alpha \equiv \frac{4}{3} + \frac{\xi_0}{\eta_0} = const. \tag{14.37}$$

This assumption is neither justified by kinetic theory, nor by simulations, nor is there a satisfactory understanding of the particular effect of bulk viscosity in a planetary ring at all. Generally, bulk viscosity ξ is tied to internal degrees of freedom in molecular systems (vibration and rotation). It accounts for the effect of a (small) relaxation time necessary to establish energy equipartition, say, the translational degrees of freedom (Chapman and Cowling 1970). But in dense systems a non-zero bulk viscosity arises already due to non-local effects (Chapman and Cowling 1970). Salo et al. determined values for the bulk viscosity, fitting the theoretically expected dynamic pressure to a simulated low amplitude compression wave. Although the values of the bulk viscosity found this way[4] led to a quantitative description of the stability boundary and the growth rates of overstable modes in simulations in dense rings (Schmidt et al. 2001; Schmidt and Salo 2003), it was noted later that the same procedure failed to describe the physics of a dilute planetary ring. The values of the bulk viscosity determined from dilute simulations would lead to overstability in the theoretical model, which is not seen in the simulations. The reason for this failure is out-of-phase oscillations of the components of the pressure tensor, described in terms of kinetic theory by Latter and Ogilvie (2006). This non-Newtonian behavior of the pressure tensor they labeled as 'non-local in time'. In the limit of a dense uniform system with large collision frequency these oscillations are damped on a time scale that is faster than the orbital time (Latter and Ogilvie 2008), and one is left with a small relaxation time necessary for the adjustment of excitations between different components of the pressure tensor, i.e. a situation which is similar to the effect of bulk viscosity in a molecular system. In this case (Eqs. 14.33–14.37) provide a good qualitative description of the radial viscous evolution of a uniform dense ring.

In a dense ring non-axisymmetric self-gravity wakes will form. This will generally lead to strong non-Newtonian gravitational stresses, not included in Eqs. 14.33–14.37. However, for dynamical problems on length-scales that are much larger than the wavelength of the wakes, the approximation of gravitational viscosity can then be adopted (Section 14.1.3).

[4] Exceeding a dense ring's shear viscosity by a factor of $\xi_0/\eta_0 = 2-3$.

14.1.3 Self-gravity of the Ring

In Section 14.1.1 the local steady-state properties of planetary rings resulting from the balance between viscous heating and the collisional dissipation of random energy have been discussed. The inclusion of particles' mutual gravitational forces modifies the local dynamics in several, partially competing ways, depending on the mass density of the ring and the distance from the planet.

At low optical depth collective effects of self-gravity are negligible and the main effect stems from gravitational heating via close binary encounters (Cuzzi et al. 1979a, b; Hämeen-Anttila 1984; Petit and Hénon 1987; Ohtsuki 1992). For higher densities, the mean vertical self-gravity can become comparable to or even exceed the corresponding component of the central force, causing a strongly enhanced impact frequency and a reduced ring thickness (Salo and Lukkari 1982; Araki and Tremaine 1986; Wisdom and Tremaine 1988). However, in this case the ring is also susceptible to gravitational instability in the plane, which manifests in the formation of transient trailing density enhancements, called *self-gravity wakes* or *Toomre wakes* (Salo 1992a; see also Julian and Toomre 1966; Toomre and Kalnajs 1991). With increasing distance from the planet, tidal forces get weaker and eventually the direct gravitational sticking of particles becomes possible, causing the particles in the wakes to degrade into local aggregates (Salo 1995, Section 4); a similar clumping may take place at low optical depth via pairwise sticking of particles. In general, the inclusion of self-gravity leads to a strong enhancement of ring viscosity, due to increased impact frequency and gravitational stirring of the particle ensemble, and most importantly, due to gravitational torques exerted by the wakes, and the collective motion associated with them (Daisaka et al. 2001).

A convenient parameter characterizing the importance of self-gravity relative to the disrupting tidal force is the ratio of the mutual Hill-radius for a pair of particles to the sum of their physical radii (Daisaka et al. 2001):

$$r_h \equiv \frac{R_{Hill}}{R_1 + R_2} = \left(\frac{\rho_0}{3\rho_{plan}}\right)^{1/3} \left(\frac{a}{r_{plan}}\right) \frac{(1+\mu)^{1/3}}{1+\mu^{1/3}}, \tag{14.38}$$

where a is the semi-major axis and $R_{Hill} = \{(m_1 + m_2)/3M_{plan}\}^{1/3} a$, $\mu = m_1/m_2$ with $m_i = (4\pi\rho_0/3)R_i^3$ being the mass of particle i of density ρ_0, and M_{plan}, r_{plan}, and ρ_{plan} denote mass, radius and density of the planet. In the case of

identical particles ($R_i \equiv R_0, m_i \equiv m_0$), r_h can be expressed in terms of physical parameters as

$$r_h = 0.82 \left(\frac{M_{plan}}{5.69 \cdot 10^{26}\, kg} \right)^{-1/3} \left(\frac{\rho_0}{900\, kgm^{-3}} \right)^{1/3} \times \left(\frac{a}{100{,}000\, km} \right), \quad (14.39)$$

and values of r_h based on Eq. 14.39 are used in the following (e.g., Figs. 14.7–14.9). With this formula the results for a given r_h can be scaled to other distances and internal densities of particles. Assuming solid ice density for the ring particles, the main rings of Saturn correspond to $r_h = 0.6 - 1.1$, from the inner C ring to the outer A ring, respectively. Similarly, Uranian rings extend between 0.65 and 0.8 if made of ice. Note that instead of r_h, $r_p \equiv r_h^{-1}$ is also often employed to parameterize gravity (Ohtsuki 1993; Salo 1995); the advantage of using r_h is that larger values correspond to stronger gravity; also the limit $r_h = 0$ corresponds to non-gravitating particles.

14.1.3.1 Gravitational Encounters

For low τ the main effect of gravity comes from close binary encounters, which act like totally elastic impacts: the kinetic energy of the encountering pair is conserved, while the deflection of mutual orbits transfers energy from the systematic velocity field to random motions. This extra heating is efficient if the velocity dispersion c is smaller than the mutual escape speed $v_{esc} = \sqrt{2Gm_0/R_0}$ of particles, but becomes inefficient for $c > v_{esc}$. Thus, encounters, if acting alone, would establish a state with $c \sim v_{esc}$ (Safronov 1969; Cuzzi et al. 1979a, b). However, if the physical impacts are able to maintain $c > v_{esc}$, then the effect of encounters is negligible. The condition for the importance of encounters can be written in terms of an upper limit for the vertical thickness, $H < H_{esc}$, where the effective geometric thickness defined by $H = \sqrt{12\langle z^2 \rangle}$ denotes the full thickness of a uniform layer with the same vertical dispersion as the actual distribution. For low optical depths we have $H \approx 2c/\Omega$. Writing $v_{esc} = \sqrt{24} r_h^{3/2} R_0 \Omega$ implies

$$\frac{H_{esc}}{R_0} \approx 10 {r_h}^{3/2} \quad (14.40)$$

In the case of constant coefficient of restitution $\varepsilon_n \square \leq 0.5$, the impacts alone maintain $H/R_0 \approx 5$, which implies that gravitational encounters dominate over physical impacts for $r_h > 0.7$.

14.1.3.2 Vertical Self-gravity

In very dense systems (high optical depth τ and filling factor ρ/ρ_0) the collective effects of self-gravity become increasingly important. First of all, the vertical component of self-gravity, F_z, may exceed the corresponding component of the central force, $F_c = -\Omega^2 z$. For simplicity, assume an infinite homogeneous layer of identical particles with an effective geometric thickness H. Inside the layer, with given density ρ, Poisson's equation gives for the vertical self-gravity

$$F_z(z) = -2\pi G \int_{-z}^{z} \rho(z')\, dz' = -\frac{4\pi G \sigma z}{H}$$

so that

$$\frac{F_z}{F_c} = \frac{4\pi G\sigma}{H\Omega^2} = 48\tau {r_h}^3 \frac{R_0}{H} \quad (14.41)$$

Assuming a Gaussian vertical mass distribution, the vertical self-gravity near the equatorial plane is a factor $\sqrt{;6/\pi}$ larger if F_z/F_c is parameterized in terms of H as defined above. Analogous to H_{esc} we define H_{fz} as a thickness of the system for which $F_z \sim F_c$,

$$\frac{H_{fz}}{R_0} \approx 65\tau\, {r_h}^3, \quad (14.42)$$

(for the case of a Gaussian mass distribution). For typical values of Saturn's B-ring, $r_h \sim 0.8$, $\tau \sim 1.5$, the vertical self-gravity exceeds the central component, unless $H/R_0 > 50$. As shown in simulations (Wisdom and Tremaine 1988; Salo 1991) the extra vertical force tends to reduce H quite markedly, both due to the increased vertical frequency itself and also indirectly via the enhanced dissipation (see Fig. 14.5). This implies a strongly enhanced viscosity for any given τ. However, there are other effects of self-gravity which will lead to an even more drastic enhancement of viscosity.

14.1.3.3 Gravitational Wakes

Intuitively, the planar components of self-gravity might be expected to have less importance than the vertical component, due to partial cancellation of forces. However, as shown by Toomre, a self-gravitating differentially rotating particle disk is locally unstable against the growth of axisymmetric disturbances if its radial velocity dispersion falls below the critical value

$$c_{cr} = \frac{3.36 G\sigma}{\kappa}, \quad (14.43)$$

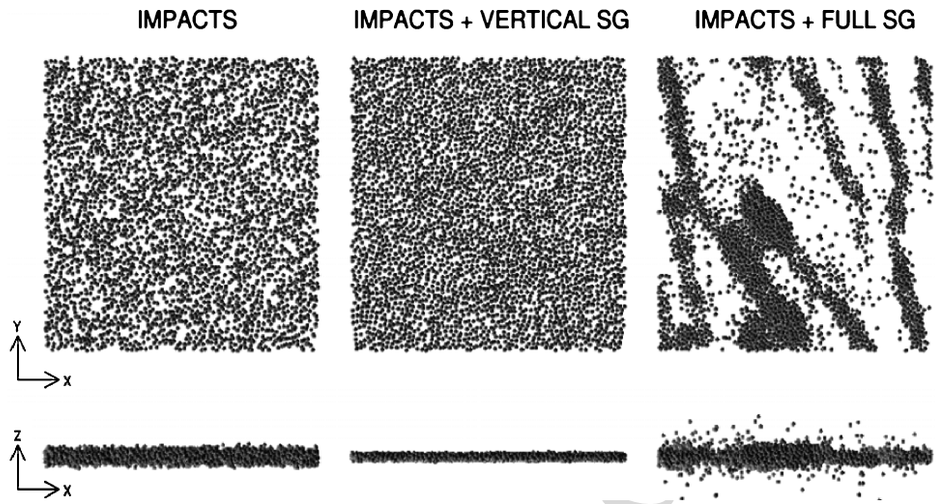

Fig. 14.5 Comparison between vertical and full self-gravity in simulations. In the left panel only physical collisions between particles are taken into account, for a simulated ring with $\varepsilon_n = 0.5$, $\tau = 0.75$, $r_h = 0.82$ (corresponding to $a = 100{,}000$ km for a solid ice particle density of 900 kgm^{-3}, or to $a = 126{,}000$ if $\rho = 450\,\mathrm{kgm}^{-3}$). In the middle panel the vertical component of self-gravity is included, calculated in a self-consistent manner from the vertical density distribution (Salo, 1991). Near the central plane the ratio of vertical self-gravity to the vertical component of central force $F_z/F_c \approx 8.8$, corresponding to an enhanced frequency of vertical oscillations by a factor $\Omega_z/\Omega = \sqrt{1 + F_z/F_c} \approx 3.1$: a very similar result would be obtained with the method of Wisdom and Tremaine (1988), who used a constant enhancement factor $\Omega_z/\Omega = 3.6$ to describe the vertical gravity. In the right panel all components of self-gravity are included, leading to the formation of self-gravity wakes. In comparison to the non-gravitating case, the inclusion of vertical gravity reduces the ring thickness in this example from $H/R_0 \approx 5 \rightarrow 3$, and increases the collision frequency by about a factor of 8. Both these effects enhance the viscosity, which in the studied example increases by a factor of two. However, when full self-gravity is included, the viscosity becomes even 30 times larger than in the non-gravitating case. A snapshot from a comoving local simulation region is displayed: the x-axis points away from the planet and the y axis in direction of orbital velocity. Note that the size of the simulation system here corresponds to $2\lambda_{cr} \times 2\lambda_{cr}$, implying that the wake structure is somewhat suppressed in comparison to what would be obtained with larger calculation regions (adapted from Salo (1995))

where κ denotes the epicyclic frequency ($\kappa = \Omega$ for the Keplerian case). This critical value offers a very convenient measure for the closeness of the system to the instability threshold in terms of the *Toomre parameter*, defined as

$$Q = \frac{c_r}{c_{cr}} = \frac{c_r \kappa}{3.36 G \sigma}, \tag{14.44}$$

where c_r denotes the radial velocity dispersion. For identical particles,

$$\frac{c_r}{R_0 \Omega} \approx 10 Q \tau \, {r_h}^3. \tag{14.45}$$

Comparison to Eq. 14.42 indicates that whenever the vertical self-gravity is important, the system is also near the threshold of collective planar instability: $F_z/F_c > 1$ corresponds to $Q < 2.5$.

How does this gravitational near-instability manifest? The gravitational collapse is opposed by the particles' random velocities, washing out small scale agglomeration, and by differential rotation, dissolving large condensations. As long as Q exceeds at least a few times unity ($Q \geq$ 2–3), the collective instability is completely avoided, and the system remains practically uniform: the main effect of gravity comes via pairwise encounters stirring up the velocity dispersion. However, if the optical depth, and thus σ, increases, or alternatively, if a ring location further away from the planet is inspected, Q could fall below about 2–3. In this case, the collective gravity, together with differential rotation, leads to the formation of shearing tilted wake structures, with individual wakes forming and dissolving in a time scale of about one orbital period (Fig. 14.5). The prominence of these structures stems from the swing amplification process Goldreich and Lynden-Bell; Toomre which significantly enhances the tiny kinematic wakes triggered by small density fluctuations.

The resulting self-gravity wakes correspond to a superposition of numerous Julian–Toomre wakes excited around each individual ring particle. Although the features are transient, in contrast to the steady response around an orbiting mass enhancement in a stellar disk studied by Julian and Toomre, this analogue is demonstrated by the similar autocorrelation function; this correspondence also justifies calling these features as *wakes*, even in the absence of any prominent individual perturber. Self-gravity wakes have also been discussed as models of flocculent spiral structure in late type galaxies (Toomre 1991; Toomre and Kalnajs 1991), in which context, however, some form of ad hoc dissipation is needed to balance the gravitational heating induced by the wakes themselves, which heating otherwise would rapidly suppress the swing amplification. In planetary rings, the dissipation via partially inelastic impacts

provides a natural cooling mechanism, leading to a statistical steady-state with $Q \sim 1$–2, characterized by a continuous regeneration of new wakes. The formation of wakes for plausible Saturn ring parameters was first demonstrated in simulations of Salo (1992a) and has thereafter been confirmed in several studies (Richardson 1994; Daisaka and Ida 1999; Ohtsuki and Emori 2000). Moreover, spatial auto-correlation analysis of simulated wakes (Salo 1995; see also Toomre and Kalnajs (1991); Salo et al. 2004 see also Toomre and Kalnajs (1991)) confirms the close correspondence to Julian–Toomre stellar wakes.

AQ3 For Saturn's rings, the approximative condition for the formation of wakes, $Q < 2$, corresponds to (see Salo (1995), Ohtsuki and Emori (2000), Salo et al. (2004))

$$\tau > \tau_{\min} \approx 0.2 \left(\frac{a}{10^8 m}\right)^{-3} \left(\frac{\rho_0}{900 kgm^{-3}}\right)^{-1}, \qquad (14.46)$$

implying $\tau_{\min} \approx 0.3 - 0.1$, from the inner C ring to the outer A ring, respectively, if the internal density of solid ice is assumed for ring particles. This $\tau_{\min}$ gives a conservative *lower* limit, since Eq. 14.46 is based on the assumption of fairly dissipative identical particles that in the absence of self-gravity would concentrate in a very thin ring, just a few particle diameters thick. This is the expected behavior of particles if they follow the Bridges et al. (1984) formula for the coefficient of restitution. In regions with $\tau > \tau_{\min}$, wakes *may* form, depending on the actual particle elasticity, with more elastic impacts implying an increased $\tau_{\min}$ (see Fig. 14.6, comparing the 'frosty' and'smooth' impact models). However, $\tau > \tau_{\min}$ is not a strict boundary for wake formation: autocorrelation analysis reveals that weak wakes are always present regardless of the value of Q. Wake formation is also affected by the particle size distribution: large particles provide seeds for strong wakes. This effect is counteracted by the larger velocity dispersion achieved by small particles (Salo 1992a, b), which acts as a stabilizing factor. As a net result the wake structure is stronger among the largest particles whereas the small particles tend to have a smoother distribution (Salo et al. 2004).

The tilt angle of wakes with respect to tangential direction is determined mainly by the shear rate: for the Keplerian case the asymptotic tilt angle of the tails of the wakes is ∼15° (Julian and Toomre 1966). However, the inner portions of wakes have larger pitch angles, depending on the physical parameters. As an effective mean value ∼20° can be adopted. The typical radial spacing between wakes found in simulations (Salo 1995; Daisaka and Ida 1999) is close to Toomre's critical wavelength (Toomre 1964)

$$\lambda_{cr} = 4\pi^2 G\sigma/\kappa^2. \qquad (14.47)$$

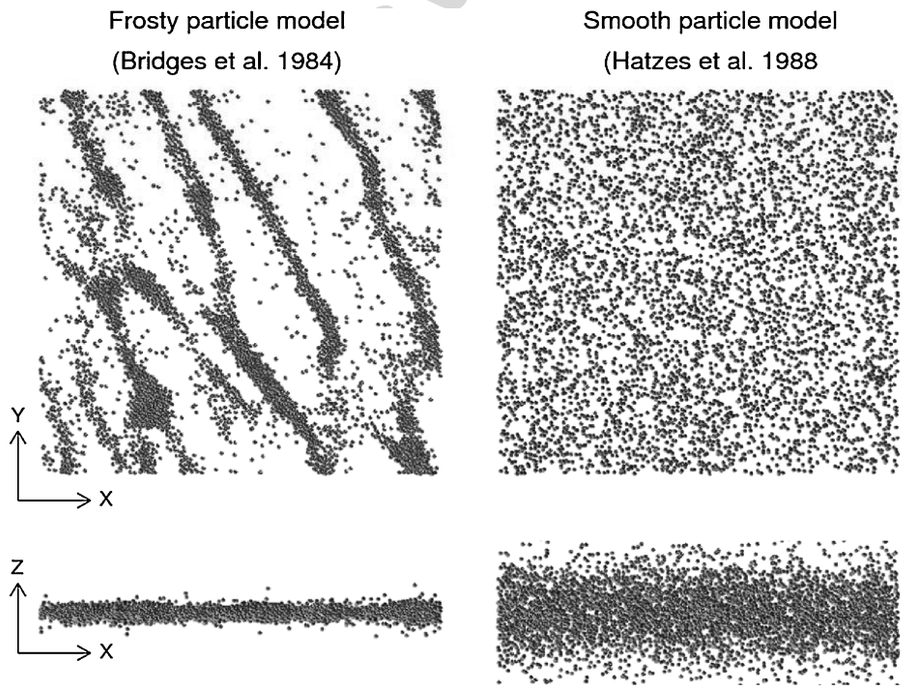

Fig. 14.6 The dependence of simulated self-gravity wakes on the assumed elasticity. In the left panel Bridges et al. (1984) formula ('frosty') is used, while in the right panel a formula from Hatzes et al. (1988) for more elastic'smooth' particles is assumed (Fig. 14.3). In both cases a system with $\tau = 0.5$ and $r_h = 0.85$ is simulated, using a $4\lambda_{cr} \times 4\lambda_{cr}$ region. For more details of the effect of particle elasticity on the wake structure, see Fig. 11 in Salo (1995)

For uni-sized particles this can be expressed in terms of the optical depth and the parameter r_h as

$$\frac{\lambda_{cr}}{R_0} = 48\pi\tau\, r_h^3 \tag{14.48}$$

For Saturn's A-ring the expected spacing is $\lambda_{cr} \sim 50$–100 m.

14.1.3.4 Survey of Self-gravity Wake Structures

Figure 14.7 displays a simulation survey of wake structures expected for different planetocentric distances. The figure illustrates clearly the gradual increase in the strength of wakes as the assumed distance or optical depth is increased, as well as the increase in the clumpiness of the wakes, and their eventual collapse into aggregates at large distances (see Section 14.4 for detailed discussion of gravitational accretion of ring particles). Changes of the appearance of the wakes are also visible. For instance, at large r_h the simulated wakes are narrow structures separated by wide gaps, whereas for large τ and intermediate $r_h \sim 0.6$ the gaps and wake widths are more comparable. The regime of overstable oscillations ($r_h < 0.6$, $\tau > 1$) is also noticeable: apparently in this regime the self-gravity is sufficiently strong to lead to a strong increase of viscosity with density, as required for the onset of overstability (Section 14.2.1), but simultaneously the non-axisymmetric wakes are not yet too strong to suppress the coherence of axisymmetric oscillations.

14.1.3.5 Gravitational Viscosity

In the case of strong wakes the total viscosity is dominated by the angular momentum transfer related to the gravitational torques exerted by the inclined wakes (gravitational viscosity), and by the transfer associated with the large scale motion of the wakes (adds to the local viscosity, whose other

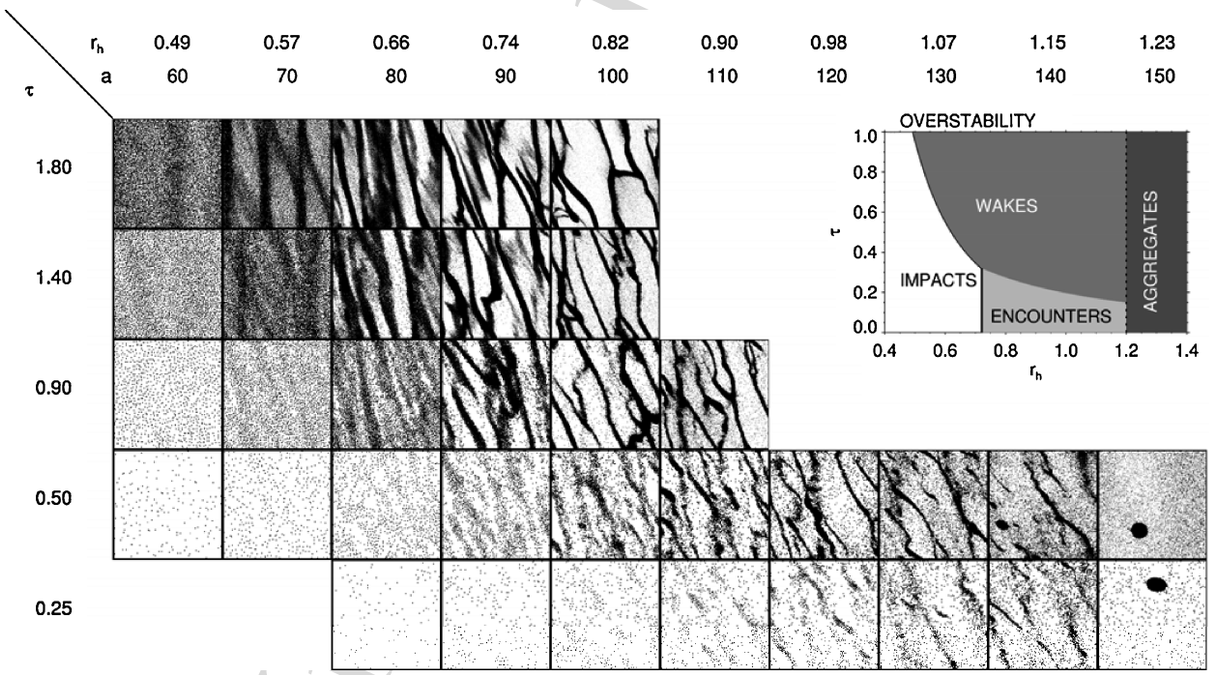

Fig. 14.7 The dependence of self-gravity wakes on optical depth τ, and the strength of gravity relative to the tidal force, quantified in terms of the r_h parameter. Also indicated are those values of Saturnocentric distance a (in units of 1000 km) to which r_h corresponds for $\rho = 900\,\mathrm{kgm}^{-3}$. Simulations use identical particles with $\varepsilon_n = 0.5$. The size of the calculation area covers $4\lambda_{cr} \times 4\lambda_{cr}$ region, thus scaling proportional to expected scale of wakes (physical size scales according to $\lambda_{cr}/R_o \sim r_h^3\tau$, varying from 35 to 600 particle radii). Note the region in the upper left ($\tau > 1$, $r_h \sim 0.6$) where axisymmetric overstable oscillations (Section 14.2.1) coexist with the inclined gravity wakes. Also note that τ here refers to the average geometric optical depth of the system (the total area of particles divided by the calculation area). The photometric optical depth would be generally different, its value also depending on the observing direction (Salo et al., 2004; Porco et al., 2008; Robbins et al., 2009). The insert shows schematically the dynamical regimes where physical impacts, pairwise gravity, and collective gravity dominate, based on a simple estimate of which ingredient alone would maintain the largest radial velocity dispersion ($c_r = 2R\Omega$ for impacts, $c_r = v_{esc}$ for encounters, or $Q = 2$ for wakes; see Salo (1995), Ohtsuki and Emori (2000), Daisaka et al. (2001). Also indicated is the region where overstability occurs in simulations, and the boundary beyond which particles clump into local aggregates in simulations ($r_h \approx 1.2$, see Salo (1995) and Karjalainen and Salo (2004))

contribution is associated with random motions[5]). Compared to these, the nonlocal (collisional) viscosity has a minor contribution. Based on dimensional arguments, the gravitational viscosity is expected to be of the order of $L^2\Omega$, where L is the typical radial scale of momentum transport and $L\Omega$ is the associated (specific) tangential momentum. Using $L = \lambda_{cr} \propto G\sigma/\Omega^2$ and including a semi-empirical correction factor $C(r_h) = 26r_h^5$ obtained by fits to viscosities determined from simulations, Daisaka et al. (2001) derived the formula

$$\nu_{grav} \approx \frac{1}{2} C(r_h) \frac{G^2\sigma^2}{\Omega^3}. \quad (14.49)$$

Moreover, they showed that in the case of strong wakes ($r_h > 0.7$) the local viscosity associated with the streaming motion related to wakes is of the same order of magnitude as the gravitational viscosity; in this case the numerical value of total (kinematic) viscosity can be approximated as

$$\nu \approx \nu_{grav} + \nu_l \approx C(r_h) \frac{G^2\sigma^2}{\Omega^3}. \quad (14.50)$$

Similar formulae, but without the correction factor, have been discussed for example by Ward and Cameron (1978) and in the context of spiral torques in galaxy disks by Lynden-Bell and Kalnajs (1972). As discussed by Daisaka et al. (2001), the strong distance-dependence implied by the correction factor $C(r_h)$ is likely to be associated with the particulate nature of the system now in question. Namely, the maximal density of a gravitationally perturbed region is limited by the internal density of particles: this limitation is increasingly severe as r_h is decreased, since the scale of wakes is then reduced compared to the particle size (see Eq. 14.48). No such limitation is present in the analysis of a continuum fluid where the surface density perturbations can at least in principle be of the order of the surface density itself.

The values for the viscosity determined by Daisaka et al. were fully confirmed by Tanaka et al. who showed that the most convenient way of measuring the total viscosity in self-gravitating particle simulations is via the associated energy loss in impacts. When the wake amplitude has reached a statistical steady-state, the time averages of energy loss and viscous gain are equal, and ν is obtained from Eq. 14.5. Similar method was used in the nongravitating simulations of Salo et al. (2001) to check the viscosities measured with the Wisdom and Tremaine (1988) method.

[5] These two kinds of local viscosity formally correspond to a stress tensor which is split into two terms as $P_{xy} = \sigma \bar{v}_x \bar{v}_y + \Pi_{xy}$. Here $\bar{v}$ is the mean velocity of (a large number of) ring particles in a (still small) Lagrangian surface element of the rings. The componenent Π_{xy} (the pressure tensor) then corresponds to the random motion of particles *in* this Lagrangian element. With shear rate s the viscosities are defined as $\sigma\, s\, \nu = P_{xy}$.

Figure 14.8 displays the dependence of the total viscosity on τ and r_h in simulations. The dependence of various contributions are shown separately (upper panels), illustrating the dominance of ν_{grav} and the close agreement in numerical values $\nu_l \approx \nu_{grav}$ in the case of strong wake structure ($r_h > 0.7$). The lower panel displays the total viscosities (gravitational + local + nonlocal contributions), also indicating the good agreement with Eq. 14.50. Strictly speaking, this formula was obtained by fits to simulations assuming constant elasticity $\varepsilon_n = 0.5$. However, for the plausible frosty particle elasticity laws, the total viscosities are not extremely sensitive to the applied elasticity. According to Fig. 14.9, the viscosity varies less than a factor of two for a constant $0 < \varepsilon_n < 0.6$; for the Bridges et al. (1984) formula the viscosity varies at most by three if the scale factor $v_c/v_B < 10$.

14.1.3.6 Observational Signatures of Self-gravity Wakes

Self-gravity wakes, trailing by $\sim 20°$ with respect to tangential direction, offer a straightforward explanation for the long-known quadrupole azimuthal brightness variation of Saturn's rings, i.e. the fact that in Earth-bound observations the post-elongation quadrant of each ansa appears brighter than the pre-elongation quadrant. This variation results as the reflecting surface area is the smallest when the wakes are seen more or less along their long-axis (at ring longitudes $\sim 20°$ before ansae), and largest when seen edge-on (see Fig. 14.10). The effect was first noted for the A ring – where it amounts to even 35% – in ground-based photographs (Camichel 1958; Lumme and Irvine 1976; Thompson et al. 1981) and was later analyzed in detail from Voyager data (Franklin et al. 1987; Dones et al. 1993).

The realization that trailing inhomogeneities would account for such variations is due to the seminal paper Colombo et al. where the probable connection to Julian and Toomre (1966) wakes was first suggested (see also Franklin et al. (1987); Dones and Porco 1989). First detailed photometric modeling of self-gravity wakes was carried out in Salo et al., demonstrating that N-body wake models (with Bridges et al. (1984) elasticity law and particle internal density one-half of solid ice density), can account in a robust manner for the overall longitude and elevation dependence of the A ring brightness variations, as seen in ground-based observations, and in Voyager observations in both reflected and transmitted light. This conclusion was confirmed by the comparison to the extensive Hubble Space Telescope data set in French et al., where the observed asymmetry amplitude and longitude of minimum brightness were characterized as a function of Saturnocentric distance for a full range of geometries accessible from Earth. It was also shown that there is a trade-off between various dynamical parameters: AQ4

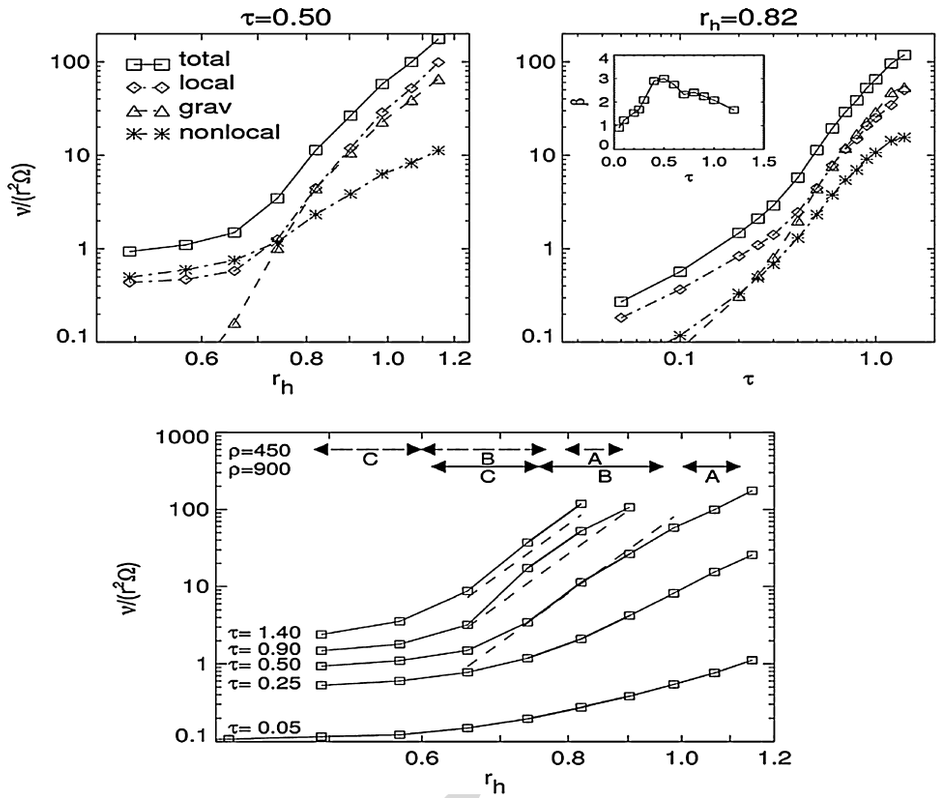

Fig. 14.8 Upper left panel: The dependence of various contributions to viscosity on r_h ($\tau = 0.5$ and $\varepsilon_n = 0.5$) from simulations. The gravitational viscosity ν_{grav} becomes dominant for $r_h > 0.7 - 0.8$, which increase is accompanied with an increased ν_l. This regime corresponds to the emergence of strong wake structure (Fig. 14.7). Upper right panel: Dependence on τ for fixed $r_h = 0.82$, $\varepsilon_n = 0.5$. The inset shows the slope $\beta = \partial \log \nu / \partial \log \tau$, rising from $\beta = 1$ at low τ to $\beta > 2$ due to the increased contribution of gravitational viscosity. Lower panel: Total viscosity as a function of τ and r_h (for $\varepsilon_n = 0.5$). Ring regions corresponding to the values of r_h are indicated (for internal particle densities $\rho = 900\,\mathrm{kg\,m^{-3}}$ and $\rho = 450\,\mathrm{kg\,m^{-3}}$). The dashed line indicates the Daisaka et al. (2001) fitting formula $\nu_{tot}/\left(R_0^2\Omega\right) \approx 380 {r_h}^{11}\tau^2$, expected for the case of strong wakes; this formula is the same as Eq. 14.50, now written in terms of r_h and τ. In physical units, the simulated viscosity for $a = 130{,}000\,\mathrm{km}$ corresponds to about $100\,\mathrm{cm^2 s^{-1}}$ (for $\sigma = 400\,\mathrm{kg\,m^{-2}}$ and $\rho = 900\,\mathrm{kg\,m^{-3}}$)

the modeled asymmetry is reduced for more elastic particles, lower internal density, or smaller optical depth, and vice versa (these dependencies are qualitatively consistent with the dynamical strength of wakes, measured in terms of ν_{grav} in Figs. 14.8 and 14.9); also, assuming an extended size distribution reduces the modeled asymmetry. Nevertheless, the fact that maximum asymmetry amplitude is seen in the mid A-ring ($a \sim 129{,}000\,\mathrm{km}$) favors underdense particles: for example, for solid ice density the modeled asymmetry would peak at mid B-ring and fall sharply at the A ring region (see Fig. 14.23 of French et al. (2007)). The HST data also showed that a weak azimuthal brightness asymmetry is present in the inner B ring, with an amplitude of roughly one-quarter of the maximum amplitude in the mid A-ring: this reduced amplitude is consistent with the weaker self-gravity wakes forming closer to the planet, even when allowing for the presumably larger surface density of the B ring. The B ring asymmetry was also inferred from the rings' radar echo (Nicholson et al. 2005); altogether the A ring asymmetry amplitude appeared about twice larger in radar signal (12.6 cm) compared to optical, while being consistent with the longitude dependence: this can be interpreted as a evidence that the wake structure is more dominant in the population of large particles as compared to smaller ones. Azimuthal variations are also present in Saturn's microwave radiation reflected and transmitted by the rings (Dunn et al. 2004, 2007).

An even more striking demonstration of gravity wakes in Saturn's rings is offered by stellar occultations observed by the Cassini Ultraviolet Imaging Spectrograph (UVIS) (Colwell et al. 2006a, 2007), the Visual and Infrared Mapping Spectrometer (VIMS) (Hedman et al. 2007) and occultations recorded by the Radio Science Subsystem (RSS) (Marouf et al. 2006). These studies indicate a significant longitude-dependence of optical depth throughout the A and B rings, consistent with the brightness asymmetry (the non-detection of ground-based reflection asymmetry in the dense B ring is due to low brightness contrast in the case of high τ). The apparent optical depth depends also strongly on elevation (Colwell et al. 2006a, 2007), consistent with the

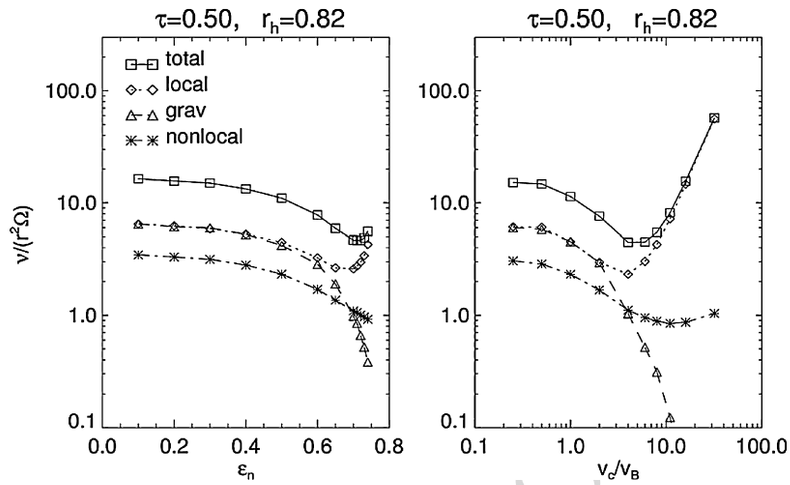

Fig. 14.9 Effect of particle elasticity on viscosity. In the left frame different values of the constant coefficient of restitution are compared, while in right frame a Bridges et al. (1984) type velocity-dependent formula is applied with different scale factors (see Eq. 14.14). In the case of constant ε_n, the local viscosity diverges for $\varepsilon_n > 0.75$, since then no thermal equilibrium is possible in the system (see Fig. 14.2 for $\varepsilon_{crit}(\tau)$): when this limiting ε_{crit} is approached, the steady-state velocity dispersion increases and the role of self-gravity becomes insignificant. Similarly, an increase of the scale factor in the velocity-dependent ε_n (v_n) leads to hotter systems, reducing all other contributions to viscosity in comparison to local viscosity

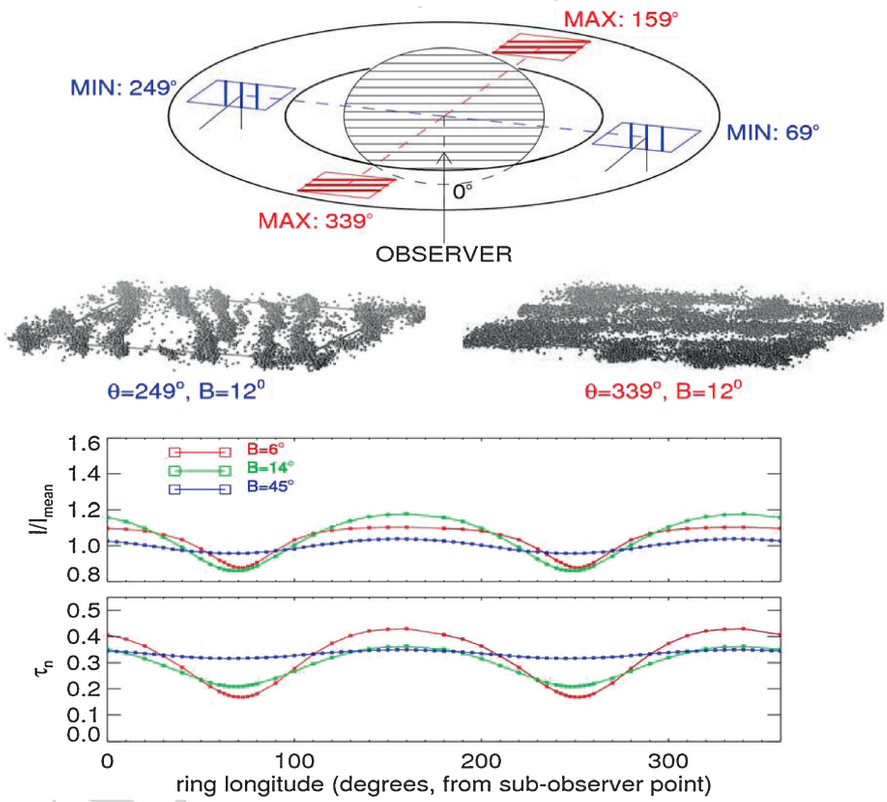

Fig. 14.10 Schematic presentation of self-gravity wakes and azimuthal brightness asymmetry (from Salo et al. (2004)). At low elevation angles B the wakes, trailing here by about 21° with respect to the local tangential direction, are seen roughly along their long axis at ring longitudes of 249° and 69°, and perpendicular to their long axis at longitudes of 339° and 159°. In the former case the rarefied regions between wakes are visible, reducing the reflecting surface area: this corresponds to minimum brightness. In the latter case rarefied regions are hidden by the wakes in low tilt angle images, maximizing the reflecting area. A similar effect is seen in the apparent optical depth observed in occultations, which is smallest when viewed along the wakes. In reflected light at low phase angle the modeled asymmetry amplitude for the A ring has a maximum at $B \sim 10 - 15°$, consistent with HST observations (French et al., 2007); similar maximum is seen also in CIRS observations of ring thermal emission (Ferrari et al., 2009). For the optical depth the expected variation increases toward smaller elevations: VIMS occultations at $B = 3.45°$ indicate a very strong longitude-dependence in the A ring transmission (Hedman et al., 2007)

predictions of the wake models (Salo et al. 2004). The azimuthal brightness variations based on observations with Cassini Imaging Subsystem (ISS) have been recently analyzed in Porco et al., also favoring very dissipative, underdense particles. Azimuthal variations have also been observed in the ring's thermal radiation by the Cassini Composite and Infrared Spectrometer (CIRS) instrument (Ferrari et al. 2009), implying a striking agreement with the amplitude of reflected light variations.

Some poorly understood observations relevant to wake structure remain. For example, the A ring asymmetry drops significantly beyond the Encke gap. One possibility (French et al. 2007) is that wakes become clumpier at larger radial distances (before collapsing to aggregates) which reduces the longitude dependence of ring reflectivity or opacity. However, the observed drop is even more rapid than models predict. A more likely explanation is a wider particle size distribution in the regions beyond the Encke gap, which would reduce the contrast of wakes (Salo et al. 2004; French et al. 2007). Both factors may contribute also simultaneously: Robbins et al. suggest that clumpier wakes can stir up smaller particles, leading to apparently wider size distribution. Stronger wakes also lead to increased maximal impact velocities, which may lead to enhanced release of impact-debris, if regolith-covered particles are assumed (Salo and Schmidt 2007). This in turn would reduce the wake contrast; a similar model helps to account for the propeller brightness contrast (Section 14.3.3). Another poorly understood observation (Dones et al. 1993; French et al. 2007) is the very rapid rise in the brightness asymmetry amplitude from the inner to the mid A ring (amplitude peaks at $a \sim 129{,}000$ km), in comparison to the much shallower rise in the modeled amplitude, when fixed particle properties are assumed (French et al. 2007). Again, radius-dependent size distribution could account for this, but no self-consistent models yet exist.

The extensive set of Cassini occultation profiles has made it possible to probe the gravity wake properties as a function of radial location. To facilitate this, the wake structure has been modeled as an alternating sequence of dense wakes and rarefied inter-wake regions, describing the wakes as parallel, infinitely long slabs with a rectangular (Colwell et al. 2006a; see also Dunn et al. (2004); Colwell et al. 2007, see also Dunn et al. (2004) or ellipsoidal (Hedman et al. 2007) cross section, defined by the wake's radial width W and geometric thickness H. The UVIS and VIMS occultations suggest (see also Chapter 7.7) that the A ring wakes have $H/L \sim 0.1$, where L is the radial separation between adjacent wakes. Identifying L with the Toomre wavelength $\sim$50 m, this suggest that the geometric thickness of A ring wakes is only of the order of 5 m (Hedman et al. 2007; Colwell et al. 2006a). The UVIS observations imply $W/L \sim 0.4$ for the A ring wakes (thus the inferred gaps are wider than wakes). On the other hand, the deduced W/L approaches even unity for the optically thickest parts of the B ring (densely packed wakes with only narrow gaps); in fact Colwell et al. (2007) suggest that the photometric optical depth reflects mainly the density of packing between the wakes.

The density wave estimates of total viscosities seem consistent with the expected total viscosity in the presence of gravity wakes. In particular Tiscareno et al. (2007) estimated surface densities and viscosities of the A ring from low amplitude density waves observed in Cassini ISS images, and found a very good agreement with Eq. 14.50, for both the magnitude of the derived viscosity and its radial increase with Saturnocentric distance. However, the agreement in magnitude can be partly fortuitous, since it was obtained by assuming a solid ice density for particles, whereas all the aforementioned studies of the A ring azimuthal brightness variations favor under-dense particles; low internal densities were deduced also in Robbins et al., based on modeling UVIS observations of ring transmission. According to Eqs. 14.39 and 14.49, $\nu_{grav} \propto \rho^{5/3}$ for a fixed distance and σ; reducing ρ by one-half would thus imply a factor of three smaller viscosity. Nevertheless, Eq. 14.49 refers to a identical particles and a specific elastic law ($\varepsilon_n = 0.5$); releasing these assumptions might easily compensate for the difference.

14.2 Instabilities

A classical problem of planetary ring dynamics is the stability of the ring flow. It addresses dynamical processes on time-scales that are small compared to the secular viscous evolution of the disc. If the ring is in a steady state then small perturbations are unavoidable (for instance through the gravitational force of the satellites of the planet). The question of stability theory is whether the perturbed ring will return to the steady state, i.e. whether the ring is stable with respect to the perturbation, or, if the perturbation will grow. In the latter case the steady state is unstable. If the flow is unstable, the steady state is destroyed by perturbations of arbitrarily small magnitude and it will eventually be replaced by another configuration which is stable, and, in general more complex and structured.

The wealth of radial structure of Saturn's B ring revealed by the Voyager observations (Smith et al. 1982; Lane et al. 1982) stimulated the search for mechanisms of intrinsic instability, that could produce at least part of the observed structure. Prominent models proposed in the literature are the viscous (diffusion) instability (Lukkari 1981; Lin and Bodenheimer 1981; Ward 1981), ballistic transport models (Durisen 1995), angular momentum and mass transport related to electromagnetic effects on small grains (Goertz et al. 1986; Goertz and Morfill 1988; Shan and Goertz 1991), viscous overstability (Schmit and Tscharnuter 1995, 1999;

Spahn et al. 2000; Salo et al. 2001; Schmidt et al. 2001; Latter and Ogilvie 2009), or instability of the radial shear profile due to a certain dependence of shear stress on the shear rate of the flow (Tremaine 2003).

14.2.1 Viscous Overstability

If a planetary ring is overstable, it spontaneously develops axisymmetric waves on a 100 m scale. These waves bear many similarities to density waves although overstable waves develop without external resonant perturbation. A planetary ring becomes overstable if the viscosity is increasing steeply enough with optical depth, which is expected in dense rings. In this case the shear in the compressed phase of the wave can feed back energy from the ring's flow to the oscillations. In contrast to density waves overstability is not strictly bound to self-gravity of the ring, although self-gravity generally alters the conditions necessary for the onset of overstability, and the wavelength and frequency of the oscillations. Axisymmetric 100–200 m wavelike perturbations in Saturn's A and B rings, consistent with overstability, are seen in Cassini RSS (Thomson et al. 2007) and the UVIS data (Colwell et al. 2007).

Viscous overstability was proposed by Borderies et al. (1985), expanding on earlier work (Borderies et al. 1983b), to explain the eccentricity of narrow ringlets observed around Saturn and Uranus (see also Longaretti and Rappaport (1995)). Borderies et al. (1985) also mention the possibility of axisymmetric oscillatory instability of a planetary ring, and Goldreich and Tremaine (1978b) point out that density waves may become overstable. As a spontaneous local instability of Saturn's B ring overstability was investigated in detail in terms of an isothermal hydrodynamic model by Schmit and Tscharnuter (1995) (1999). Spahn et al. (2000) included the thermal balance equation in this concept.

In local simulations of a perturbed dense planetary ring Mosqueira (1996) showed that the condition for viscous overstability derived by Borderies et al. (1985) can be fulfilled. The first direct demonstration of viscous overstability in an unperturbed dense collisional ring was given in self-gravitating local simulations by Salo et al. (2001), using parameters plausible for Saturn's B ring (see also Daisaka et al. 2001). The simulations spontaneously developed axisymmetric oscillations on a length of about 100 m, for an optical depth $\tau > 1$. Generally the oscillatory pattern was found to coexist with self-gravity wakes (Fig. 14.11).

In their local simulations Salo et al. (2001) also used an enhanced frequency of vertical oscillations $\Omega_z/\Omega > 1$ to approximate effects of the ring's vertical self-gravity (Wisdom and Tremaine 1988). For $\Omega_z/\Omega = 3.6$ the stability boundary was again about $\tau \sim 1$ and for $\Omega_z/\Omega = 1$ (i.e. no self-gravity) overstability developed for $\tau > 4$. This suggests that the conditions necessary for overstability are not connected to self-gravity itself but rather to a large collision frequency, which determines the viscous properties. Further, Salo et al. (2001) showed that overstability develops in simulations with a broad distribution of particle sizes. A quantitative comparison of simulations to overstability on the linear level in a hydrodynamic model was carried out by Schmidt et al. (2001), the nonlinear saturation of overstable waves was studied by Schmidt and Salo (2003), and nonlinear wavetrain solutions are derived by Latter and Ogilvie (2009).

14.2.1.1 A Linear Model

Linearizing the isothermal Eqs. 14.33–14.37 about the steady state solution $\sigma = \Sigma$, $u = 0$, $v = 0$ we obtain

$$\dot{\sigma} = -\Sigma u' \tag{14.51}$$

$$\dot{u} = 2\Omega v - \left(\frac{1}{\Sigma}\left.\frac{\partial p}{\partial \sigma}\right|_0 - \frac{2\pi G}{|k|}\right)\sigma\prime + \frac{\alpha}{\Sigma}\eta_0 u'' \tag{14.52}$$

$$\dot{v} = -\frac{\Omega}{2}u + \frac{1}{\Sigma}\left(\eta_0 v'' - \frac{3}{2}\Omega\left.\frac{\partial \eta}{\partial \sigma}\right|_0 \sigma'\right), \tag{14.53}$$

where η_0 denotes the dynamic shear viscosity of the unperturbed flow, α is the constant defined by Eq. 14.37, and we use

$$p(\sigma)' = \left.\frac{\partial p}{\partial \sigma}\right|_0 \sigma', \quad \eta(\sigma)' = \left.\frac{\partial \eta}{\partial \sigma}\right|_0 \sigma',$$

the subscript indicating that the derivative is taken at the steady state. Further, we inserted the solution

$$\Phi_{Disk}(r,z) = -\frac{2\pi G}{|k|}\sigma(r)\exp[-|kz|] \tag{14.54}$$

of the thin disk Poisson Eq. 14.36, valid for harmonic radial modes with wavenumber k (Binney and Tremaine 1987).

We write

$$\nu_0 = \frac{\eta_0}{\Sigma} \tag{14.55}$$

for the unperturbed kinematic shear viscosity and define

$$\left.\frac{\partial \eta}{\partial \sigma}\right|_0 = \nu_0 \left.\frac{\partial \ln \eta}{\partial \ln \sigma}\right|_0 \tag{14.56}$$

to display the proportionality of $\partial\eta/\partial\sigma$ to the kinematic viscosity ν_0 explicitly. For harmonic perturbations

$$u \propto \exp[st + ikx] \tag{14.57}$$

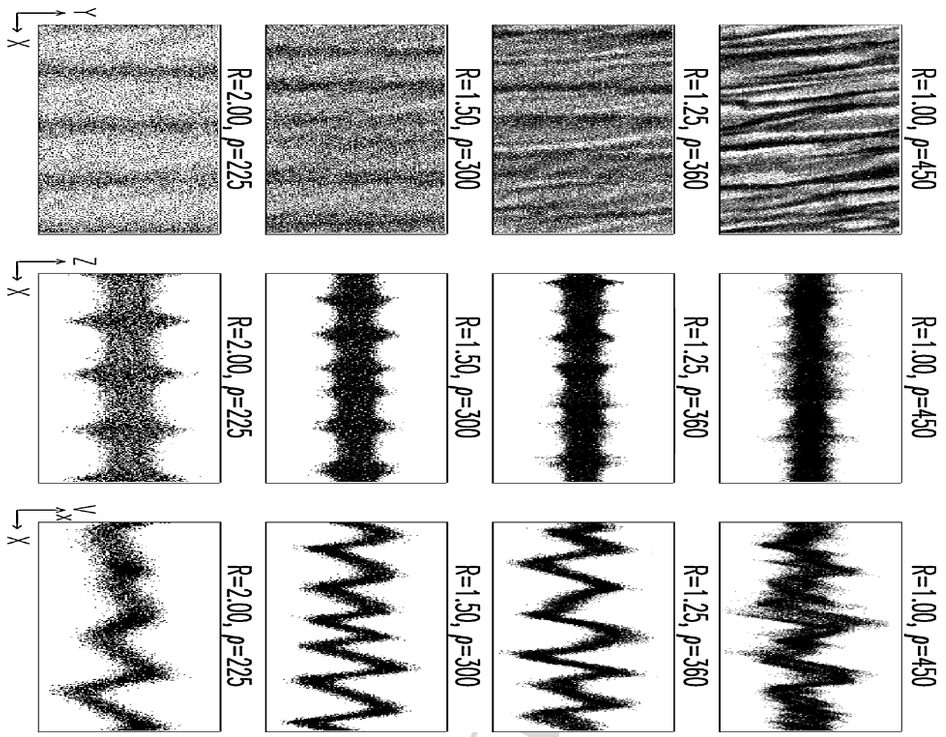

Fig. 14.11 Transition from wake dominated (upper row) to overstability dominated self-gravitating simulations. Optical depth and surface mass density are fixed ($\tau = 1.4$, σ=840kgm^{-2}) while particle radius and internal density are varied (plot labels indicate particle radius in meters and internal density in units of kg/m^3). In the left panels the simulation cell is seen from above and particle centers are plotted as dots. The planet is to the left and the direction of orbital motion is upward. The size of the simulation region is $L_x \times L_y = 10\lambda_{cr} \times 4\lambda_{cr}$ where $\lambda_{cr} = 4\pi^2 G\sigma/\Omega^2$ is Toomre's critical wavelength (Toomre, 1964) (see Section 14.1.3). In the case of strong wake structure the Toomre parameter Q assumes a value of about one. (The relatively small Q is due to the low internal density of the particles. In earlier simulations that used the density of solid ice $Q = 2$ was found.) On the panels in the middle the system is seen from aside. The axisymmetric oscillations are also seen in the profiles of radial velocity (right panels), as well as in tangential velocity and velocity dispersion (not shown). From Salo et al. (2001)

we then obtain from Eqs. 14.51–14.53 the dispersion relation (Schmit and Tscharnuter 1995)

$$s^3 + s^2\nu_0 k^2(1+\alpha) + s\left(\Omega^2 + \left.\frac{\partial p}{\partial\sigma}\right|_0 k^2 - 2\pi G\Sigma|k| + \nu_0^2 k^4\alpha\right) + \nu_0 k^2\left(3\Omega^2\left.\frac{\partial\ln\eta}{\partial\ln\sigma}\right|_0 + \left.\frac{\partial p}{\partial\sigma}\right|_0 k^2 - 2\pi G\Sigma|k|\right) = 0. \quad (14.58)$$

Equation 14.58 has, in the limit of long wavelengths, the approximate roots

$$s^{(1)} = -3\nu_0 k^2\left(\left.\frac{\partial\ln\eta}{\partial\ln\sigma}\right|_0 - \left[\frac{1}{3} - \left.\frac{\partial\ln\eta}{\partial\ln\sigma}\right|_0\right]\frac{2\pi G\Sigma}{\Omega^2}|k|\right) + O\left(k^4\right) \quad (14.59)$$

$$s^{(2/3)} = \pm i\left(\Omega - \pi\frac{G\Sigma}{\Omega}|k| + \left[\frac{1}{2\Omega}\left.\frac{\partial p}{\partial\sigma}\right|_0 - \frac{\pi^2}{2}\frac{G^2\Sigma^2}{\Omega^3}\right] \times\left[1 + \frac{\pi G\Sigma}{\Omega^2}|k|\right]k^2\right) - \frac{3}{2}\nu_0 k^2\left(\frac{1+\alpha}{3} - \left.\frac{\partial\ln\eta}{\partial\ln\sigma}\right|_0 + \left[\frac{1}{3} - \left.\frac{\partial\ln\eta}{\partial\ln\sigma}\right|_0\right]\frac{2\pi G\Sigma}{\Omega^2}|k|\right) + O\left(k^4\right) \quad (14.60)$$

The first root corresponds to the viscous instability mechanism (Ward 1981; Lukkari 1981; Lin and Bodenheimer 1981), for long modes $k \to 0$ being unstable if $\left.\frac{\partial\ln\eta}{\partial\ln\sigma}\right|_0 < 0$ (see Section 14.2.2). The conjugate complex modes correspond to viscously damped or amplified wave solutions. A more rigorous analysis (valid for all k) shows that if

$$\left.\frac{\partial\ln\eta}{\partial\ln\sigma}\right|_0 > \frac{1+\alpha}{3} - \frac{\alpha}{3\Omega^2}\left(2\pi G\Sigma|k| - \left.\frac{\partial p}{\partial\sigma}\right|_0 k^2 - (1+\alpha)\nu_0^2 k^4\right), \quad (14.61)$$

the amplitude of the waves grows, i.e. the system becomes overstable (i.e. it undergoes a Hopf bifurcation) if the viscosity increases steeply enough with the surface density of the ring. For the parameterization $\nu \propto \sigma^\beta$ of the surface density dependence of the shear viscosity often adopted in hydrodynamic studies (Schmit and Tscharnuter 1995; Durisen 1995; Schmit and Tscharnuter 1999; Spahn et al. 2000; Salo et al. 2001; Schmidt et al. 2001; Schmidt and Salo 2003) one recovers the criterion (Schmit and Tscharnuter 1995) for overstability ($k \to 0$)

$$\beta > \beta_{cr} := \frac{2-\alpha}{3} = \frac{1}{3}\left(\frac{\zeta}{\nu} - \frac{2}{3}\right). \tag{14.62}$$

It can be shown that the same criterion follows from the condition for overstability given by Borderies et al. (1983a), namely that their viscous coefficient t_1 is positive, at lowest order in the nonlinearity parameter q. For narrow rings Papaloizou and Lin (1988) derived an equivalent criterion, not taking into account bulk viscosity. Assuming that bulk and shear viscosities are equal ($\alpha = 7/3$) Eq. 14.62 implies $\beta_{cr} = 1/9$; inclusion of axial self-gravity (see Eq. 14.61) leads to β_{cr} even slightly less than zero (Schmit and Tscharnuter 1995). But according to direct simulation the stability limit is rather $\beta_{cr} \approx 1$. It was suggested that this discrepancy could follow from the assumption of isothermality (Spahn et al. 2000; Salo et al. 2001; Schmidt et al. 2001) made in the above analysis: in practice the velocity dispersion also adjusts locally to overstable oscillations, which acts as a stabilizing factor. The value of the bulk viscosity was determined from simulations (Salo et al. 2001; Schmidt et al. 2001) and included to the analysis, improving the agreement with linear growth rates at large optical depth. However what was interpreted as the influence of bulk viscosity is in part related to out-of-phase oscillations of the components of the velocity ellipsoid (see discussion in 1.2.2). This effect cannot be modeled by Newtonian stress (Latter and Ogilvie 2006).

Taking the time derivative of Eq. 14.52, using Eqs. 14.52 and 14.53 to eliminate ν and setting

$$\sigma = -\Sigma \int_{-\infty}^{t} d\bar{t} u'(\bar{t})$$

we can write Eqs. 14.51–14.53 formally as a forced wave equation

$$\ddot{u} + \Omega^2 u - \left(\left.\frac{\partial p}{\partial \sigma}\right|_0 - \frac{2\pi G\Sigma}{|k|}\right) u'' = \nu_0 \left(f(r,t) + \alpha \nu_0 u''''\right) \tag{14.63}$$

where

$$f(r,t) \equiv (1+\alpha)\dot{u}'' + \int_{-\infty}^{t} d\bar{t}\left[3\Omega^2 \left.\frac{\partial \ln \eta}{\partial \ln \sigma}\right|_0 u'' - \left(\left.\frac{\partial p}{\partial \sigma}\right|_0 - \frac{2\pi G\Sigma}{|k|}\right) u''''\right].$$

An approximate solution for the oscillatory mode is obtained by assuming that ν_0 in Eq. 14.63 is a small parameter (compared to Ω/k^2) and using a multi-scale expansion (Kevorkian and Cole 1996). In this case (Eq. 14.63) indeed becomes an equation for a viscously forced inertial-acoustic wave and the dynamics splits on two well separated time scales t and $\theta = \nu_0 t$ so that

$$u(x,t,\theta) = A(\theta)\, u_0(x,t),$$

where A is a slowly variable amplitude and u_0 is the rapidly oscillating solution of the homogeneous problem. At zeroth order in ν_0 one obtains a wave with dispersion relation[6]

$$\Omega = \pm\sqrt{\Omega^2 - 2\pi G\Sigma|k| + \left.\frac{\partial p}{\partial \sigma}\right|_0 k^2}. \tag{14.64}$$

At order ν_0 we get an equation for the evolution of the amplitude A

$$\frac{\partial}{\partial\theta}A = -\frac{3}{2}k^2\left[\frac{1+\alpha}{3} - \left.\frac{\partial \ln \eta}{\partial \ln \sigma}\right|_0 + \frac{2\pi G\Sigma}{\Omega^2}|k| \times \left(\frac{1}{3} - \left.\frac{\partial \ln \eta}{\partial \ln \sigma}\right|_0\right)\right] A + O\left(k^4\right) \tag{14.65}$$

Thus, a solution to the linear Eq. 14.63, applicable to long modes (i.e. neglecting $O\left(k^4\right)$), is

$$u = u(0)\exp\left(-\frac{3}{2}\nu_0 k^2\left[\frac{1+\alpha}{3} - \left.\frac{\partial \ln \eta}{\partial \ln \sigma}\right|_0 + \frac{2\pi G\Sigma}{\Omega^2}|k|\left(\frac{1}{3} - \left.\frac{\partial \ln \eta}{\partial \ln \sigma}\right|_0\right)\right] t\right)\cos(\Omega t + kx) \tag{14.66}$$

This describes a radial wave with exponentially growing or damping amplitude, recovering the growth rate (Eq. 14.60).

From the nonlinear Eqs. 14.33–14.35 one can derive an equation for the amplitude growth which contains a

[6] The same dispersion relation is obtained for tightly wound spiral density waves.

term which is cubic in the amplitude A, in addition to the linear terms in Eq. 14.65. This cubic term, arising from the nonlinearities in the system, leads to a saturation of the growth of overstable modes at a certain amplitude depending on the wavelength (Schmidt and Salo 2003; Latter and Ogilvie 2009). It has been shown analytically and in simulations that generally standing waves are unstable with respect to traveling wave solutions.

14.2.1.2 Overstability and Self-gravity

Self-gravity of the ring has a twofold effect on overstable oscillations. On the one hand, self-gravity promotes overstability by steepening the dependence of viscosity on density (Fig. 14.8). On the other hand, in the case of strong self-gravity, the *nonaxisymmetric* wakes tend to suppress the the growth of *axisymmetric* overstable oscillations, although simulations (Salo et al. 2001) show that the co-existence of both phenomena is permitted (Figs. 14.7 and 14.11). Currently no analytical theory exists to model the formation of overstability in a ring with self-gravity wakes.

Another important effect is related to the axisymmetric component of self-gravity. Namely, in non-selfgravitating models the wavelengths of overstable oscillations are observed to grow with time (Schmit and Tscharnuter 1995, 1999; Schmidt and Salo 2003). It is not clear at present if this growth would eventually be limited by the curvature of the ring flow (which was neglected in the modeling so far) or by nonlinear effects. In contrast, the inclusion of self-gravity leads to a limited regime of wavelengths which can grow. This was noted by Schmit and Tscharnuter (1999) and is in agreement with the results from direct simulations where only axisymmetric gravity is included.

14.2.2 Viscous Instability

AQ5

Viscous instability was discussed after 1980 as a promising candidate to explain the banded structure of Saturn's B ring seen in the Voyager images (Lukkari 1981; Lin and Bodenheimer 1981; Ward 1981; Hämeen-Anttila 1982; Stewart et al. 1984). It is a diffusion instability, developing in sheared collisional systems if the dynamic shear viscosity η fulfills the condition

$$\frac{\partial \eta}{\partial \sigma} < 0, \tag{14.67}$$

which follows from the linearized Eqs. 14.51–14.53 in the non-selfgravitating or long wavelength limit (see Eq. 14.59). In this case the (viscous) collisional flux of particles is directed *away* from ring regions of depleted density, thereby amplifying perturbations in the density profile. Earlier, viscous instability was discussed for accretion discs (Lightman and Eardley 1974).

From the linearized Eqs. 14.51–14.53 one can easily derive a diffusion equation, assuming a slow viscous radial migration of material and $v = 0$ (i.e. purely Keplerian velocity). In this case Eq. 14.53 can be solved for u which gives together with Eq. 14.51

$$\dot{\sigma} = 3 \left.\frac{\partial \eta}{\partial \sigma}\right|_0 \sigma'' \tag{14.68}$$

For harmonic perturbations (Eq. 14.57) we recover the growth-rate (Eq. 14.59).

In Section 14.1.1.5 we demonstrated in terms of simulations that the steady state viscous properties of a planetary ring depend sensitively on the particle elasticity. If the particles are as dissipative as suggested by the Bridges et al. (1984) collision law, then the ring is in a very flat state with high filling factor. Then non-local viscosity will dominate (Wisdom and Tremaine 1988; Araki and Tremaine 1986; Araki 1991) and condition (Eq. 14.67) is not fulfilled (see the curves labeled 'frosty' in Fig. 14.4). Such a flattened and dense ring state is strongly supported by the presence of self-gravity wakes (see Fig. 14.6), which are found in Cassini data, practically all over the A and B rings (chapter by Colwell et al.).

Nevertheless, assuming more elastic collision laws one can in principle expect viscous instability. In this case the ring particles maintain in thermal equilibrium a relatively large velocity dispersion, and thus, form a ring with a vertical scale height that is much larger than the particle diameter. Then the filling factors are small, local viscosity dominates at small optical depth, and the condition 14.67 can be fulfilled at intermediate optical depths, while at large optical depth the non-local viscosity becomes important. Such behavior, leading to viscous instability, is expected for example for the'smooth' elasticity law (Fig. 14.4), for $0.6 < \tau < 2.0$. The instability can be demonstrated in direct simulation (Salo and Schmidt 2009), provided that the calculation region is large enough to cover the smallest unstable wavelengths of the order of hundred particle diameters. An example is shown in Fig. 14.12. After initial growth, the system has saturated to a bimodal quasi-steady state where collisional flux from dense dynamically cool regions is in balance with rarefied dynamically hot regions ($\nu\tau$ is radially constant). At the large wavelength limit the initial linear growth rates agree with Eq. 14.59.

The above example of viscous instability relies on the assumption of probably unrealistically elastic particles, and thus, is of limited interest. However, the studied case of identical particles with fixed elasticity is not necessarily representative of real planetary rings. Indeed, if we take into account a particle size distribution, and allow for size-dependent

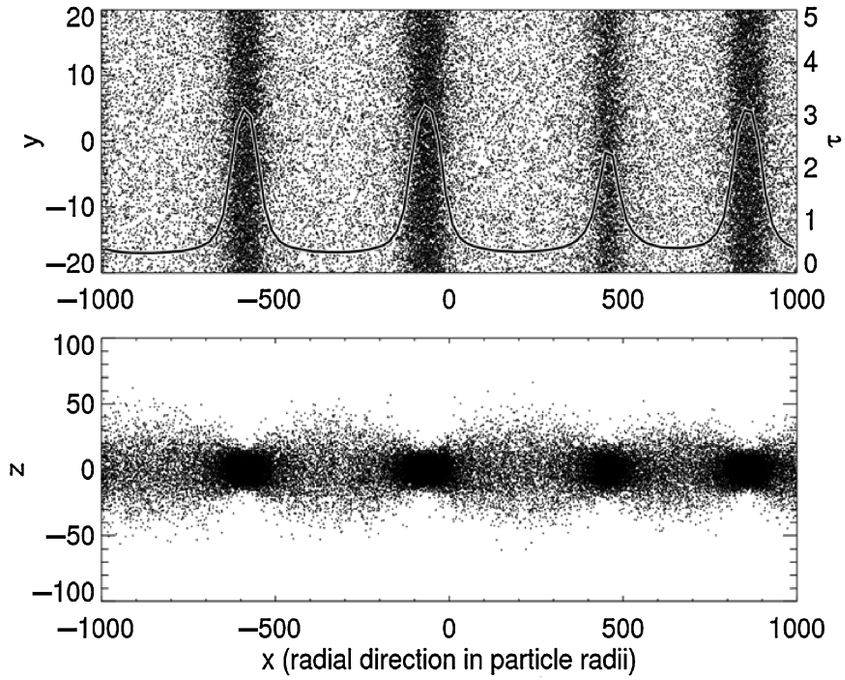

Fig. 14.12 Viscous instability in a non-gravitating simulation with $\tau = 0.94$ using the 'smooth' particle elasticity model of Fig. 14.3. During the first 100 orbital periods the system divides into several ringlets. In the plot a snapshot after 500 orbital periods is displayed. The solid line indicates the optical depth profile (upper frame). The density of the two leftmost ringlets has saturated to an almost constant level. The second ringlet from the right has started to disperse, the material being captured mainly by the rightmost ringlet which is slowly growing and migrating toward the dispersing one. It is likely that more of the ringlets will slowly disperse, and that eventually one large ringlet remains stable in the simulation box. In this way the process could generate a large-scale radial structure over long time scales. (From Salo and Schmidt)

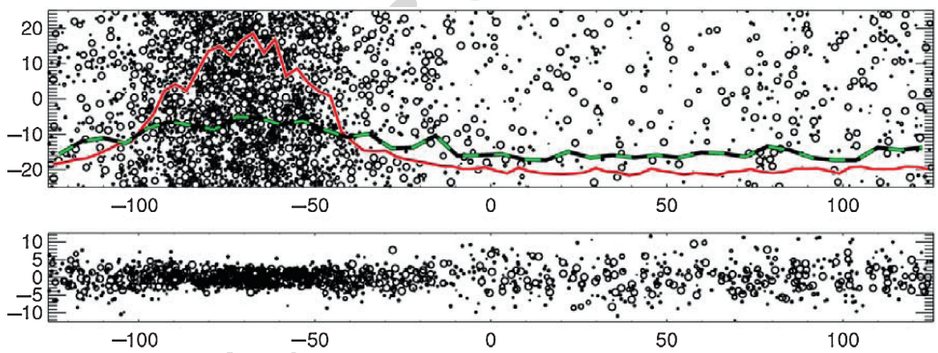

Fig. 14.13 Example of size-selective viscous instability. The non-gravitating simulation system consists of two particle sizes, with radii $R = 0.333\,\mathrm{m}$ and $R = 1\,\mathrm{m}$; both components have $\tau = 0.5$. Initially both particle species were uniformly distributed; here the distribution after 700 orbital periods is displayed. The upper frame shows a slice through the equatorial plane, the lower frame shows a side view. Symbol size corresponds to particle size and 1/5th of all particles are plotted. The solid red and and black-green dashed curves indicate the density profiles of small and large particles, respectively. In this simulation the Bridges et al. (1984) type elasticity model is used, with the scale parameter (see Eq. 14.14) depending on the size group of colliding particles: $v_c/v_B = 0.1, 1, 10$ for collisions of a small-small, small-large, and large-large pair of particles. Note that identical particles with $v_c/v_B = 10$ would not lead to instability. (From Salo and Schmidt)

elastic properties, new interesting possibilities open up. In particular, if the impacts between small particles are more inelastic than those of large particles (this is at least qualitatively in accordance with laboratory experiments (Hatzes et al. 1988; Dilley and Crawford 1996)), simulations indicate that it is possible to obtain selective instability, where the density fluctuations of small particles are enhanced against a more uniform background of large particles (see Fig. 14.13).

Qualitatively, the instability is due to the fact that an increase of the partial concentration of small particles locally reduces their velocity dispersion, since their energy balance becomes dominated by their mutual very dissipative impacts: this makes the viscosity drop with the relative concentration of small particles.

An attractive feature of this kind of selective instability is that the attained density contrast depends on the size ratio and the difference in elastic parameters between the populations: at least in principle this allows for a much richer variety of structures than the simple identical particle model leading to strictly bimodal optical depth variations. Further studies of selective instabilities, including ring self-gravity are in progress (Salo and Schmidt 2009).

14.2.3 Instabilities due to Ballistic and Electromagnetic Transport

Particles of Saturn's main rings are subject to hypervelocity impacts (10 to 50 km/s) of micro-meteoroids (100 μm to mm in size). This process leads to erosion of the ring particles by ejection of dust-sized and larger debris (Durisen 1984; Durisen et al. 1989). If the ejecta are re-absorbed at some distance by the rings it can lead to the (radial) re-distribution of mass and momentum. The latter mechanism is called ballistic transport (Ip 1983; Lissauer 1984).

It was shown by Durisen et al. (1992) that ballistic transport can produce the ramps in optical depths seen interior to the inner edges of the A and B rings (see Fig. 13.1 and discussion in Chapter 17).

As a consequence of ballistic transport Durisen (1995) proposed an instability mechanism for rings of intermediate optical depths $0.1 < \tau < 1$. The idea is that for a given radial throw-distance of ejecta (or given distribution of throw-distances) small radial variations in the optical depth profile of certain length-scales can amplify. In principle this may happen by direct re-distribution of mass and/or by radial migration of ring material due to torques exerted by re-absorbed ejecta. Durisen (1995) investigates the linear stability of a mathematical model coupling the equations for mass and momentum conservation with appropriate gain and loss terms, using models for meteoroid bombardment and ejecta distributions developed earlier (Cuzzi and Durisen 1990).

Durisen (1995) shows that the ballistic transport instability should produce radial undulations in the inner B ring of about 100 km wavelength. In the outer B ring optical depth is too high for this instability to develop. This is consistent with analysis of pre-Cassini data (Horn and Cuzzi 1996) and structure seen in Cassini SOI images (e.g. Fig. 14.5b of Porco et al. (2005)). For conditions plausible for the B ring the instability is driven by ballistic mass transport, momentum transport playing an insignificant role. Durisen (1995) argues that the observed structure can grow in a few million years. His derivation includes the smoothing effect of viscous diffusion but does not take into account gravitational viscosity. The qualitative conclusions, however, are not likely to change.

A conceptually similar instability mechanism was proposed by Goertz and Morfill (1988) (Shan and Goertz 1991). It appears as a consequence of the radial transport of charged sub-micron sized dust grains, lifted from the rings (Morfill et al. 1983; Goertz 1984). Due to their large charge to mass ratio such grains are affected strongly by the planetary magnetic field, which tends to force them to co-rotation. At re-accretion the angular momentum the particles gained from (or lost to) the magnetic field is transferred to the ring.

The dominant process driving this instability is angular momentum exchange of different ring segments with Saturn, mediated by the charged particles. The transported masses are insignificant. The instability should generate radial variations in the ring's surface mass density on a length of hundreds of kilometers (Goertz and Morfill 1988). Near synchronous orbit (at 1.87 planetary radii in the outer third of the B ring), however, the mechanism becomes inefficient since at that location charged grains have zero relative velocity to the corotational magnetic field. The growth rate of the instability is sufficiently large to overcome the smoothing effect of viscous diffusion only if the ring's viscosity is smaller than roughly 50 cm^2/s. The viscosities estimated from the damping of density waves in the A ring are generally larger by a factor of 2 to 4 (Tiscareno et al. 2007). However, the A ring viscosity is probably dominated by self-gravity wakes whose strength depends on the distance to Saturn and surface mass density. Extrapolation of formula (Eq. 14.49) (Daisaka et al. 2001) gives for the inner B ring ($r < 100{,}000$ km) viscosities below 50 cm^2/s if the surface mass density is smaller than 800 kg/m^2 (assuming a particle internal density $900 kg/m^3$).

14.2.4 Shear Rate Instability

The instability model proposed by Tremaine emphasizes the importance of investigating more general forms of the stress tensor in the dynamics of planetary rings than the Newtonian form (Section 14.1.2, Eqs. 14.28–14.30), demonstrating that non-Newtonian stress can lead to interesting dynamical consequences.

The basic idea is to consider shear stress as a non-monotonic function of shear rate $s = |\partial v/\partial x|$ (here x is

the radial coordinate and v is circumferential velocity of the flow), such that the stress-shear curve is generally increasing with s but decreasing over some interval of shear rates. If the Keplerian shear rate $s_k = 3/2\Omega$ lies in this interval, then the flow can assume three different shear rates $s_1 < s_k < s_2$ for the same value of the stress. In this case s_k will be unstable and the flow divides into radial bands of alternating shear rates s_1 and s_2.

In principle, adhesion between particles can lead to such a non-monotonic relation between shear and stress. A solid, rigidly rotating annulus would require a certain amount of tensile stress (P_{xx}) to balance the tidal forces (Tremaine 2003). This stress can be provided by adhesive forces in a state when ring particles stick on each other. More generally, one can imagine that adhesion provides a certain amount of stress also in a non-rigidly rotating ring, so that particles stick temporarily, but are released again in a collision with a third particle, or, by tidal forces, the precise balance of sticking and release depending on the shear rate. This stress would lead to deviations from the purely Keplerian rotation. Whether adhesion can indeed produce the required non-monotonic stress-shear relation in Saturn's rings, such that the Keplerian shear rate lies somewhere in the middle of the interval with decreasing stress, is not clear at present.

For planar, incompressible, viscous shear flow, neglecting self-gravity, we have a nonlinear diffusion equation for the evolution of the shear rate (Tremaine 2003)

$$\frac{\partial s}{\partial t} = -\frac{1}{\sigma}\frac{\partial^2}{\partial x^2} P_{xy}\,(s) \tag{14.69}$$

with the condition that the mean shear rate is fixed at s_k. The constant surface mass density of the ring is denoted by σ.

Stability analysis of Eq. 14.69 demonstrates that any shear rate s_k in the region $\partial P_{xy}/\partial s < 0$ is unstable. Numerical solution shows that the shear profile rapidly evolves to a piecewise linear pattern that alternates between s_1 and s_2. In the long term evolution smaller domains merge, and the typical length of the pattern grows. Thus, the overall behavior of the mathematical model (Eq. 14.69) is similar to the viscous instability model (2.2). In both cases the stress depends non-monotonically on a parameter (here shear-rate s; for viscous instability the optical depth τ) which leads to an instability such that the system develops into a state where the parameter alternates between two given stable values.

The assumption of a constant surface mass density σ, leading to Eq. 14.69, is a very strong one. Since the stress also depends on the surface density, in addition to the shear rate dependence studied here, it seems unavoidable that simultaneously perturbations in σ will develop.

14.3 Ring Moon Interactions and Narrow Rings

Saturn's rings owe a large part of their dynamical structure to the gravitational action of numerous satellites. Large satellites with orbits outside the rings generate resonant gravitational perturbations in the ring at particular radial locations, where combinations of orbital frequencies of the satellites and the ring particles are in a ratio of two integer numbers. The perturbations excite density or bending waves: spiral patterns in the ring, co-rotating with the perturbing satellite (Section 14.3.1). Such waves have been observed at numerous resonance locations mainly in Saturn's A ring. At the strongest resonances, the negative angular momentum carried by a density wave may cause an inward migration of ring particles, opening a gap in the rings.

Another class of structures are generated by small moons (moonlets or ring-moons) embedded directly in the rings. There are gaps (Section 14.3.2) cleared by the embedded satellite, density wakes at the gap edges, and also propeller-shaped features (Section 14.3.3) induced in the ring's density by skyscraper-sized moonlets. Furthermore, embedded small moons may play a crucial role in confining, sustaining and sculpting narrow ringlets (Section 14.3.4) like the F ring and the Encke-gap ringlets.

14.3.1 Spiral Waves

14.3.1.1 Background

Gravitational perturbations by satellites can excite spiral waves in planetary rings. Density waves form in the ring at radial distances where combinations of horizontal frequencies of ring particles and satellite are in the ratio of two integer numbers. They are driven by an interplay of self-gravity and inertial forces, forming a spiral pattern of compression and rarefaction of the ring. If the satellite is exterior to the rings they propagate outward with group velocity $\pi G\sigma_0/\kappa$, where σ_0 and κ are the background surface mass density and the epicyclic frequency, respectively. Such density waves transfer angular momentum from the rings to the satellite, causing the ring particles to spiral inward, while they are damped by a combination of nonlinear and viscous effects. Similarly, spiral bending waves are vertical corrugations, excited at vertical resonances with a satellite. If the satellite is external to the rings, the bending wave propagates inward from the resonance location.

Goldreich and Tremaine predicted spiral density waves excited at locations of strong resonances with satellites

AQ6

such as Mimas and Titan, suggesting that such a wave (excited at the 2:1 inner Lindblad resonance with Mimas) created the Cassini Division. Many density waves associated with resonances of Prometheus, Pandora, Janus, Epimetheus, Mimas, and Iapetus (mostly in the A ring) were discovered in the Voyager data (Cuzzi et al. 1981; Holberg 1982; Holberg et al. 1982; Esposito et al. 1983; Longaretti and Borderies 1986; Rosen et al. 1991a 1991b; Spilker et al. 2004). Bending waves were identified by Shu et al. (1983), who also developed the theory of forced bending waves, and further analyzed by Lissauer (1985) and Gresh et al. (1986). Rosen and Lissauer (1988) studied the bending wave in the C ring at the nodal resonance with Titan, where the satellite's forcing frequency equals the regression rate of the nodes of particles' orbits.

The linear theory (Goldreich and Tremaine 1978a, b, 1979b; Shu et al. 1983; Shu 1984) was often employed to analyze the waves, whereas nonlinear effects are important for most density waves found by Voyager. The nonlinear theory was developed by Shu et al. (1985a, b), and Borderies et al. (1985, 1986), and nonlinear effects were included in the study of observed waves (e.g., Longaretti and Borderies 1986; Rosen et al. 1991a, b). The large number of high resolution occultation profiles obtained by Cassini over a longer period of time led to considerable advances in modeling of density waves (see Section 14.3.1.3).

There are several motivations for analyzing density waves. Simply speaking, in the linear regime, the surface density can be derived from the dispersion relation, which governs the decrease of wavelength with the distance from the resonance and the ring viscosity can be inferred from the damping rate, which is estimated from the decrease in the amplitude of the wave (see, e.g., Goldreich and Tremaine 1978b; Shu 1984).

A motivation to study especially nonlinear density waves is to determine the torques exerted by satellites on the rings. The measurement of the torque is relevant for the dynamical evolution of the satellites that are close to Saturn's rings, and the age of the ring-satellite system that we observe presently.

14.3.1.2 Elements of Theory

Two approaches exist to study spiral density waves in a planetary ring, the fluid dynamical approach and the streamline approach. The fluid model was introduced by Goldreich and Tremaine based on the Euler equations with perturbations arising from the planet, a satellite, and the disk. It was further developed by Goldreich and Tremaine (1978a, 1979b), Shu (1984), and Shu et al. (1985a, b).

The streamline formalism was developed by Borderies et al. and its application to density waves is described in detail in Rappaport et al. Because self-gravity acts as a cohesive force, particles sharing the same semi-major axis are expected to follow the same m-lobe orbit in the reference frame rotating with the pattern speed. The shape of the streamlines is given by:

$$r = a\left[1 - e\left(a\right)\cos\left(m\phi + m\Delta\left(a\right)\right)\right], \tag{14.70}$$

where $e\left(a\right) \ll 1$ is the eccentricity and $\Delta\left(a\right)$ is a phase angle. This description assumes a Lagrangian approach to fluid motion. An unperturbed fluid particle follows a circular orbit and has coordinates a, ϕ. Once perturbed by the satellite, this same particle follows an m-lobe orbit and has coordinates $r\left(a, \phi\right), \zeta\left(a, \phi\right)$. The degree of horizontal compression of the ring material is measured by

$$J = \left.\frac{\partial r}{\partial a}\right|_{\phi} = 1 - q\cos\left(m\phi + m\Delta + \gamma\right), \tag{14.71}$$

where we neglected the small term $e\cos(m\phi + m\Delta)$, and

$$q\cos\gamma = a\frac{de}{da}, \quad q\sin\gamma = mae\frac{d\Delta}{da}. \tag{14.72}$$

Streamline crossing is prevented as long as $q < 1$. We define the phase function as (Rappaport et al. 2009)

$$f(a) = m\Delta\left(a\right) + \gamma\left(a\right). \tag{14.73}$$

Conservation of the mass of a ring element between its unperturbed and perturbed state implies

$$dm\mathrm{T}\sigma\left(r, \zeta\right) rdrd\zeta = \sigma_0(a)adad\phi,$$

so that at lowest order in e

$$\sigma = \frac{\sigma_0}{J} \tag{14.74}$$

where σ and σ_0 are the perturbed and unperturbed (or background) surface mass densities. If the ring particle distribution (with respect to size, spin, shape, etc.) is constant in time, we also have

$$\tau = \frac{\tau_0}{J}, \tag{14.75}$$

where τ_0 is the unperturbed, or background, optical depth.

Based on the above streamline formalism, the nonlinear dispersion relation for tightly wound density waves was derived by Borderies et al. (1986, see also Shu et al. (1985b); Borderies et al. (1985)) as

$$K\frac{a - a_{res}}{a_{res}} = \frac{2\pi G\tau_0|k|C\left(q\right) - 2k^2H'\left(q^2\right)c^2K}{3\left(m-1\right)\Omega^2}, \tag{14.76}$$

where a_{res} is the semi-major axis of the resonance, $K = \tau/\sigma$ is the opacity, and

$$k = \frac{df}{da} \tag{14.77}$$

is the wave number. The expressions

$$C\,(q) = \frac{4}{\pi}\int_0^{+\infty} du\,\frac{\sin^2 u}{u^2}\,H'\left(\frac{q^2\sin^2 u}{u^2}\right),$$

$$H'\left(q^2\right) = \frac{1-\sqrt{1-q^2}}{q^2\sqrt{1-q^2}}$$

result from the derivation of the self-gravitational acceleration via summation of mass-loaded streamlines of the perturbed ring. The dispersion relation (14.76) for free density waves in the linear regime ($q \to 0$) is given by Eq. 14.64 (see also Shu 1984).

14.3.1.3 Advances in Modeling

The Waves Associated with the Co-Orbital Satellites

The density waves associated with Janus and Epimetheus are especially interesting. These two co-orbital satellites swap orbits every 4 years, with the most recent reversal having occurred in January 2006. The resonance locations produced by these bodies typically shift by tens of kilometers at the times where the orbits switch around. Therefore, we expect the density waves excited at the resonances of these satellites to show temporal changes. It turns out that the group velocity is

$$v_g \approx 0.1\left[\frac{\sigma}{100\,\mathrm{g\,cm^{-2}}}\right]\,\mathrm{cm\,s^{-1}},$$

so that the waves propagate over 100 km in a time scale of about 3 years.

Lissauer et al. first studied the long term evolution of Janus and Epimetheus under the influence of ring torques exerted on the satellites. They find that the moons should evolve from their horseshoe-type configuration to a tadpole configuration in only 20 million years. They also note the multiple wavetrain excitation at the resonance locations.

Tiscareno et al. developed a model for the complex morphology of the (linear) second order waves that result from these reversals and compare to ISS images. They assume that the reversal occurs instantaneously while the waves generated at the previous resonance locations continue to propagate and new waves are launched at the new resonance locations. The observed morphology results from superposition of the various wavetrains.

This model shows in general good agreement with Cassini images, with the exception that there are regions where it predicts zero perturbation, while the image scans show oscillations. This may be due to the fact that the reversals are not instantaneous but take several months.

Power Spectrum Density Methods

The application of Power Density Methods to planetary rings was pioneered by Spilker et al. with the Voyager data. Colwell et al. used spectral methods to study density waves in stellar occultation profiles recorded by the Cassini UVIS, using a linear dispersion relation. For the Atlas 5:4 density wave Colwell et al. determined a surface density of 1.6 g/cm^2 and a viscosity of $5 \pm 2\,\mathrm{cm^2/s}$, corresponding to a ring thickness of 10 m. For other waves which have a very short damping scale, they used Fast Fourier Transforms, Maximum Entropy Methods, and Wavelet transforms. They found results roughly consistent with previous published values, but there is considerable scatter between different occultations and different techniques.

Tiscareno et al. applied the continuous Wavelet transform to weak (i.e. nearly linear) density waves in high resolution Saturn Orbit Insertion imaging data. The Wavelet transform is particularly well suited for the detection of weak waves and provides the ability to isolate multiple waves superimposed on top of each other. Tiscareno et al. fitted the wave parameters of 32 density waves, most of them previously unobserved. They found a linear increase of the surface density from the inner to the mid A ring. The ring viscosity they inferred from the wave damping increases monotonically from the Cassini Division to the Encke Gap. This is likely a consequence of the increasing strength of self-gravity wakes in this ring region, which is seen in the increasing amplitude of the brightness asymmetry (Dones et al. 1993).

Application of the Nonlinear Theory

Kinetic parameters $\tau_0\,(a)$, $q\,(a)$, $f\,(a)$, $ae\,(a)$, and $\gamma\,(a)$ are used to describe a density wave in the streamline formalism (Section 14.3.1.2). Rappaport et al. developed an inversion method to derive these parameters as a function of semi-major axis for a given density wave in the nonlinear regime, using multiple ring optical depth profiles. The method is applied to eight RSS radio occultation profiles of the Mimas 5:3 density wave. Figure 14.14a shows the solution for the five wave functions. The dotted lines correspond to the region where the functions for at least one of the profiles were extrapolated. In this extrapolation region, the functions τ_0 and

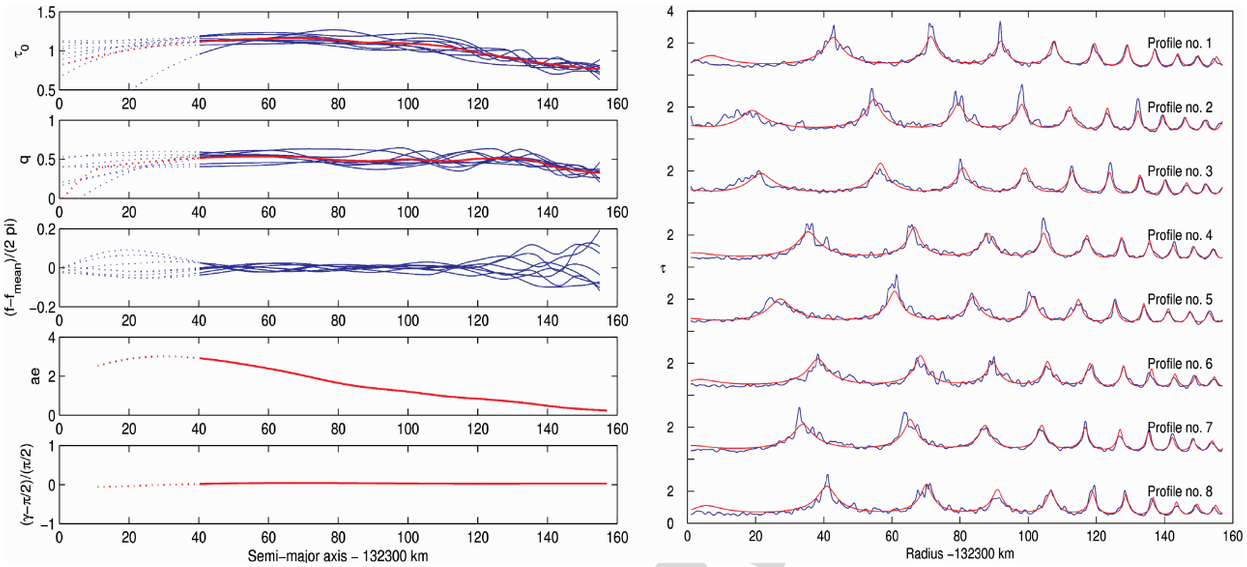

Fig. 14.14 (**a**) Kinematic parameters of the Mimas 5:3 density wave derived from the inversion procedure. The kinematic parameters obtained by considering the profiles independently from each other are shown in blue. The mean solution is displayed in red. The dotted lines refer to the region in which the parameters for at least one profile are simply extrapolated rather than obtained by the inversion method, because the approximation used in the method is not valid in these regions. For e and γ only mean profiles are determined (red lines in bottom panels). (**b**) Radio optical depth profiles for eight occultations (in blue) of the Mimas 5:3 density wave and the solution obtained by the inversion method (in red). The profiles are stacked. For each profile, the vertical scale goes from 0 to 4. Intermediate tick marks represent both the $\tau = 0$ level of the next profile, and the $\tau = 4$ level of the previous one. The resonance radius is 132301 km (Rappaport et al., 2009)

AQ7

q increase. These functions are nearly constant between 50 and 120 km from the resonance radius. In this domain the phase f is very well determined. Figure 14.14b shows the radio optical depth profiles for eight occultations (in blue) of the Mimas 5:3 density wave and the reconstructed profiles (in red). Excellent agreement is found between the observations and the model, considering the large fluctuations in optical depth in the data, notably at the peaks.

From the model the nonlinear dispersion relation 14.76 (with the pressure term quadratic in k) is used to compute the opacity, or equivalently, the surface density and the velocity dispersion. The background surface density σ_0 of this wave is found to be variable between 55 and 66 g cm^{-2}. It is enhanced at the beginning of the wave, which can be understood by considering a uniform ring in which a strong density wave is launched. The viscous angular momentum flux is negative in the region where q is close to unity but positive inward and outward. The result is that ring material is transported to the zone where the wave is strongly nonlinear. The velocity dispersion is $\approx$0.6 cm s^{-1} in the wave region.

The determination of $\tau_0\,(a)$ and $q\,(a)$ in the above example is impaired by the considerable noise in the radio data. Improved results may be possible by application of the method to UVIS data with a better signal to noise ratio. Also an improved treatment of the first wavelength of the wave is needed for an accurate estimate of the mass of a perturbing satellite.

14.3.2 Moonlet Induced Gaps

In the previous section we discussed waves generated at resonances with satellites on orbits outside the rings. With decreasing distance to the perturbing satellite the azimuthal wavenumber m of a resonance increases and neighboring resonances and related structures become more closely spaced. This is the case for instance for the resonances of Prometheus and Pandora in the outer A ring, which, however, remain well separated.

The situation is different for a satellite directly embedded in the rings (moonlet). In the vicinity of the moonlet the resonance order diverges ($m \to \infty$) and the distance between the resonances vanishes ($|\Delta r_m| \to 0$). As a consequence, density waves cannot be excited at these resonances, since, firstly, the radial width W_r of a resonance exceeds the inter-resonant distances $W_m > |\Delta r_m|$ so that the resonance regions overlap (Wisdom 1980; Duncan et al. 1989) and phase-mixing destroys the resonant phase commensurability, leading to chaotic particle motion. Secondly, these distances do not give enough radial space for the waves to develop, i.e. $|\Delta r_m| < \lambda$, (λ – wavelength of resonant waves).

Instead, the gravitational angular momentum exchange between embedded moonlet and surrounding (perturbed) ring material tends to open a gap in the ring. Goldreich and Tremaine (1980) derived the gravitational torque density $dT_{Moonlet}/dr \propto \pm M^2_{Moonlet}/|x|^4$ exerted on a moonlet

by an infinitesimally narrow ring of width dr (still containing a large number of resonances) located at radial distance $x = a - a_0$ from the moonlet at a_0, where a denotes semi-major axes. The signs correspond to ring matter inside and outside the moonlet's orbit, respectively: Angular momentum is transferred to the moonlet (positive sign) by ring material interior to its orbit and ring particles migrate towards the planet. Ring material exterior to the moonlet's orbit gains angular momentum (negative sign), particles are pushed outward. In steady state this transfer of angular momentum is counteracted by a viscous torque $T_\nu \propto 3\pi\nu\sigma r^2\Omega$, mediated by physical collisions (Lissauer et al. 1981) and gravitational interactions (Daisaka et al. 2001) between the ring particles, quantified by the viscosity ν, with the result that a gap of finite size is opened in the ring.

Integrating the torque density (summing all ringlet contributions) and balancing with the viscous torques one obtains for the width of the gap (Lissauer et al. 1981; Petit and Hénon 1988; Spahn et al. 1992a, 1993)

$$W_G \propto \begin{cases} M_{Moonlet}^{1/3} \propto R_{Moonlet}, \; for \;\; M_{Moonlet} < M_0 \\ M_{Moonlet}^{2/3} \propto R_{Moonlet}^2, \; for \;\; M_{Moonlet} > M_0. \end{cases} \tag{14.78}$$

where M_0 corresponds to a kilometer sized moonlet (solid ice density). A comparison of the Encke- and the Keeler gaps, created by Pan and Daphnis, respectively, confirms the scaling $W_G \propto M_{Moonlet}^{2/3}$ for large ring-moons fairly well ($M_{Moonlet}$, $R_{Moonlet}$ – moonlet mass and radius).

Density wakes form at the edges of the gap downstream from the moon (Cuzzi and Scargle 1985; Showalter et al. 1986) as a response to the periodic perturbation by the moon. The moonlet forces an eccentricity $e \propto x^{-2}$ of ring particles and their orbital phases become temporarily synchronized, leading to the formation of a kinematic wake (Showalter et al. 1986). The streamline wavelength $\lambda_w = 3\pi x$ of a wake increases with mean radial distance x from the moon. The wakes are more pronounced for larger moons, because then diffusion ($\propto c^2$ [see Eq. 14.68]) cannot dominate the systematic wake induced velocities $\propto r_0 e\,(x)\,\Omega\,(r_0)$ during one synodic period

$$t_{syn} = \frac{4\pi}{3\Omega\,(r_0)}\left|\frac{r_0}{x}\right|. \tag{14.79}$$

Such density wakes have been found at the edges of the Encke gap (Cuzzi and Scargle 1985; Showalter et al. 1986) and the Keeler-gap (Cooke 1991) which led to the detection of the two embedded ring moons Pan (Showalter 1991) and Daphnis (Porco et al. 2005), respectively.

Cassini cameras revealed a surprising "rope" structure in the Pan wakes in the outer Encke gap edge (Porco et al. 2005, their Fig. 6c). Such features were predicted by Lewis and Stewart (2005) as a consequence of the interaction of the moonlet induced perturbation with the self-gravity of ring. Apparently the compression and stretching of self-gravitating material in the first cycles of the Pan wake leads to magnified self-gravity wakes. On the other hand, further away from the gap edges the moonlet wakes may disrupt self-gravity wakes (Lewis and Stewart 2005), which formed in the unperturbed region upstream from the moon.

The secular evolution of a satellite embedded within a gap in a ring was studied by Hahn (2008) and Hahn (2007). An eccentric satellite should excite resonant low-amplitude density wave in the self-gravitating ring exterior to the gap (Hahn 2008), which in turn tends to damp the moon's eccentricity. In the case of Pan in the outer A ring the wavelength would be on the order of hundreds of kilometer and the amplitude $\Delta\sigma/\sigma < 4\times10^{-3}$. Similarly, an inclined satellite should launch a spiral bending wave in the ring exterior to the gap (Hahn 2007).

14.3.3 Propellers – the Action of Tiny Moons

If an embedded moonlet is smaller than (roughly) a few hundred meters in size (solid ice density), then the gap it induces in the ring can be closed by viscous diffusion before it extends around the complete ring circumference. This competition of gravitational scattering and viscous diffusion creates a typical structure in the rings (Fig. 14.15a) dubbed "propellers" (Spahn and Sremčević 2000; Sremčević et al. 2002). Such an S-shaped density undulation – typically induced in a disk as the local response to an embedded mass – was studied by Julian and Toomre (1966), however, not taking into account physical collisions between particles, which are essential for planetary rings.

The first four propeller features were detected in high resolution Cassini images of the A ring (Tiscareno et al. 2006). Later, a large number of propellers were found preferentially interior to the Encke gap (Sremčević et al. 2007; Tiscareno et al. 2008) and larger propellers also outside the Encke gap (Sremčević et al. 2007; Tiscareno et al. 2008; Burns et al. 2008).

A propeller can form in the rings if the eccentricities forced by the moonlet's gravity are much larger than those implied by the quasi-steady velocity dispersion established by the balance of viscous heating and collisional cooling. The (incomplete) propeller-gaps develop roughly at radial displacement $\pm 1.5 R_{Hill}$ from the moonlet, where

$$R_{Hill} = r_0 \left(\frac{M_{Moonlet}}{3M_{Saturn}}\right)^{\frac{1}{3}}, \tag{14.80}$$

AQ8

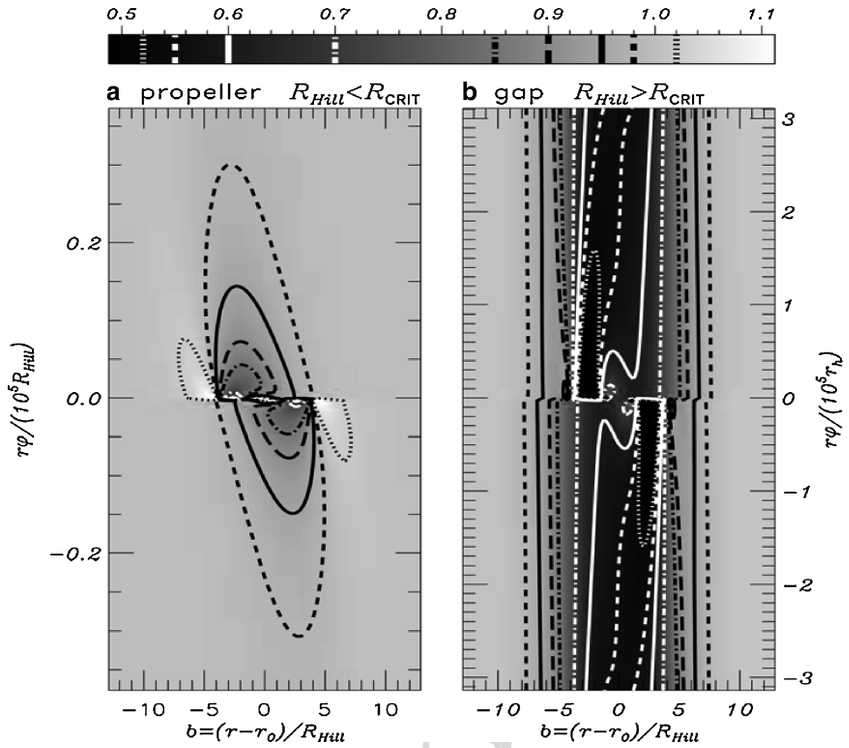

Fig. 14.15 Perturbations of the rings' surface-mass density induced by an embedded moonlet (Sremčević et al., 2002). Panel **(a)**: The characteristic propeller structure induced by a small moonlet ($R = 100$ m; moonlet's density $\rho = 600\,\mathrm{kg\,m^{-3}}$), which does not extend around the whole circumference. Panel **(b)**: A complete gap induced by a moon massive enough to create structure surviving a synodic period t_{syn}

is the Hill scale. Let the mean square radial distance $\langle \Delta r^2 \rangle \approx \nu t$ characterize viscous diffusion of a ring particle performing a random walk mediated by collisions (and gravitational encounters) in the ring. Then the distance $L(t) = \sqrt{\langle \Delta r^2 \rangle}$, arising from Gaussian solutions of the linearized diffusion Eq. 14.68, is the radial scale particles migrate on average during time t. For moonlets with $R_{Hill} < R_{crit} := L\left(t_{syn}\left(R_{Hill}\right)\right)$ all gravity-induced density undulations are smeared out during one synodic period t_{syn} so that the gaps remain incomplete (Fig. 14.15a), while a complete gap is formed when $R_{Hill} > R_{crit}$ (Fig. 14.15b).

The azimuthal extent of these density depletions can be estimated (Spahn and Sremčević 2000; Sremčević et al. 2002) by equating the radial length scales of gap formation and closing

$$R_{Hill} = L\left(t_E\right) \approx \sqrt{\nu t_E},$$

defining the time $t_E < t_{syn}$ necessary to viscously close the moonlet-induced gaps. The time t_E is related to an azimuthal longitude $\varphi_E = 3\Omega_0 t_E/2 < 2\pi$. This simple calculation predicts the radial and azimuthal extent of a propeller-gap as a function of moonlet mass and ring viscosity

$$R_{Hill} \propto M_{Moonlet}^{1/3} \propto R_{Moonlet}; \varphi_E \propto \frac{M_{Moonlet}}{\nu} \propto \frac{R_{Moonlet}^3}{\nu}. \tag{14.81}$$

These scalings have been confirmed with N-body simulations by Seiß et al. (2005) using non-selfgravitating single-sized particles.

The comparison of the scaling (Eq. 14.81) to observations (i.e. the dependence of the azimuthal length of a propeller on the radial separation of the bright propeller streaks) is complicated by several factors. First, in images of the backlit rings, where propellers were first detected (Tiscareno et al. 2006; Sremčević et al. 2007), the interpretation of low brightness is ambiguous since opaque or totally void regions both appear dark. Thus, the bright propeller streaks could be moonlet induced gaps or density enhancements. Second, the propeller should induce density wakes in the ring, which flank the incomplete gaps downstream, similar to the Daphnis and Pan wakes (Fig. 13.4) forming at the edges of the Keeler and Encke gaps. This wake pattern can alter the appearance of a propeller and it will scale differently from (Eq. 14.81). Third, the moonlet induced structure in the ring's density is superimposed on, and may interact with, the self-gravity wakes in Saturn's A ring. As a result, the propeller

induced pattern looks fuzzy (Fig. 14.16). Since the typical length of the self-gravity wakes is independent of the moonlet size this may well affect the observed scaling of the propeller dimensions, especially for small moonlets. Fourth, the perturbation of the moon may locally enhance the collision frequency and collision speeds in the ring, leading to breakup of loosely bound particle aggregates and to the release of debris residing on larger ring particles. This would increase the optical depth, and thus, the observed pattern of brightness does not necessarily correspond directly to the pattern in the surface mass density, thus leading to differences from the scaling (Eq. 14.81). Fifth, the ring viscosity (entering the scaling as a pre-factor) might vary significantly in the propeller region (Tiscareno et al. 2007).

AQ9 Analyzing twelve propeller features Sremčević et al. (2007) found a near linear dependence

$$\varphi_E \propto R_{Moonlet}^{\alpha} \quad \text{with} \quad \alpha \approx 1.1, \tag{14.82}$$

and not the expected cubic scaling (Eq. 14.81). Tiscareno et al. (2008) found a large scatter of the propeller dimensions in their data set (fewer than a hundred resolved propellers) and argue that a cubic scaling should not yet be ruled out. Sremčević et al. (2007) show that a near linear scaling can be understood if the bright propeller-features in the images are associated with the moonlet induced wakes and not the gaps. For 100 m-sized moonlets these wakes are not very pronounced and they are probably perturbed by the pattern of self-gravity wakes in the rings (Fig. 14.16). Nevertheless, the moonlet wakes will be destroyed near the longitude of streamline crossing $\varphi_S \propto R_{Moonlet}$, the longitude where the collision frequency in the streamline rapidly increases (Showalter et al. 1986; Spahn et al. 1994), which would result in the observed linear scaling with the moonlet size. This idea was further quantified by photometric modeling of particle configurations from self-gravitating simulations of a propeller by Sremčević et al. (2007). They showed that release of regolith and a possible destruction of the self-gravity wakes in the perturbed propeller regions in principle offers an explanation of the observed brightness of the propeller-streaks (Fig. 14.16) in backlit geometry. The re-accumulation of the debris is only completed downstream from the streamline crossing point (Sremčević et al. 2007), which would lead naturally to a slightly increased value $\alpha > 1$ in Eq. 14.82. Moreover, for this geometry the gaps are not expected to stand out relative to the ring background brightness, in agreement with observations. Earlier it has been suggested that the bright streaks seen in backlit images are actually the propeller gaps (Tiscareno et al. 2006). However, this interpretation would require fairly large optical depths for the ring and the gap

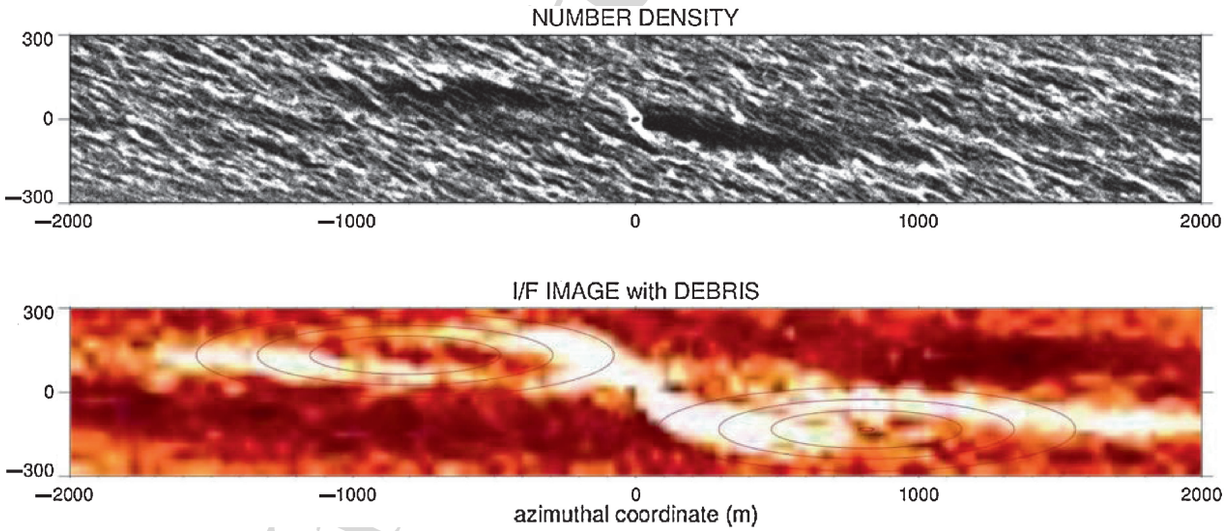

Fig. 14.16 Upper frame: Effect of a 40 m diameter moonlet in self-gravitating simulation. The frame shows a 4km by 0.6km azimuthally elongated simulation region co-moving with the moonlet's orbital motion (the planet is downward and orbital motion is to the right). Two symmetric density enhancements are seen downstream of the moonlet, in addition to smaller scale self-gravity wakes formed by the 1 m ring particles. The simulation also illustrates the limited-accretion mechanism pointed out by Porco et al.: the moonlet with internal density 600 kgm^{-3} was able to accumulate lower density ring particles (450 kgm^{-3}) until its Hill sphere was filled. Lower frame: Synthetic image constructed for the geometry of the Cassini SOI images where the first propellers were detected (Tiscareno et al., 2006). A fair correspondence to observed propellers (contours indicate a fit to the SOI4 propeller feature in Tiscareno et al.; see Fig. 16 in Chapter 13) is achieved if ring particles are covered with loosely-bound regolith, released in the vicinity of the moonlet due to locally enhanced impact speeds: here it is assumed that impacts with $v_{imp} > 1\mathrm{cms}^{-1}$ lead to release of regolith-debris, which is re-accumulated during the subsequent impacts. Even a modest amount of such debris (here $\tau_{debris} = 0.025$ averaged over the calculation region) is able to hide the downstream gaps and enhance the brightness of the density crests. Fig. 14 modified from Sremčević et al. (supplementary online-material); photometric calculations with the method of Salo and Karjalainen, Salo et al.

(see Fig. S12 in Sremčević et al. (2007)), and it is inconsistent with the observation of propellers on the lit side of Saturn's A ring (Tiscareno et al. 2008), since in reflected light the brightness should saturate for optical depths near unity.

Tiscareno et al. (2006) derived a moonlet-size distribution $n(R)\,dR \propto R^{-q}dR$ with $q \approx 5$ including the two known ring-moons Pan and Daphnis in the fit. Sremčević et al. (2007) derived a larger slope $q > 9$, and Tiscareno et al. (2008) obtained $q \approx 6$, both considering Pan and Daphnis to be isolated from the propeller-moonlet population. This perception suggests three families of bodies in the rings: ring-particles (cm $< R <$ 10 m, roughly), propeller-moonlets (10 m $< R <$ 500 m), and ring-moons (0.5 km $< R <$ 100 km). Such a classification seems to be consistent with the scenario of ring-formation in episodic cascades (Esposito et al. 2005) where ringmoons and moonlets are continuously destroyed by meteoroid impacts (Section 14.4.1; see also Chapter 17). Self-gravitating simulations with an extended particle size-distribution (Lewis and Stewart 2009) suggest that a steep moonlet size distribution is essential for the formation of distinct propeller features, since otherwise frequent interaction with neighboring larger moonlets would tend to destroy the propeller.

With a few exceptions the propeller features appear concentrated in a belt (Sremčević et al. 2007) in the mid-A ring (interior to the Encke division) that is divided in three bands of roughly 1000 km width (Tiscareno et al. 2008). It was suggested that the belt represents a younger ring region, formed after the destruction of a ring moon in a catastrophic collision (Sremčević et al. 2007). Tiscareno et al. (2008) argue that the perturbations induced by the strong Pandora 7:6 and Janus/Epimetheus 5:4 resonances, both lying in the propeller belt, might locally hamper the formation of the propeller structure, in this way splitting the propeller region in three sub-belts. It is intriguing that the propeller belt is found at the same ring radius as the maximum of the brightness asymmetry of Saturn's A ring (Dones et al. 1993), the latter being a measure for the strength of the self-gravity wakes. If this is a coincidence or if the two phenomena are related is unclear at present.

Exterior to the Encke gap only a few (generally larger) propellers were found so far (Sremčević et al. 2007; Tiscareno et al. 2008; Burns et al. 2008). The largest propellers show clearly the theoretically expected incomplete gaps and moonlet induced wakes. Fluctuations in the ring's surface mass density may cause (via gravitational interaction) a stochastic migration of the moonlet (Burns et al. 2008) as seen in simulations (Lewis and Stewart 2009). A very similar effect (type III migration) was suggested for growing planetary embryos embedded in pre-planetary gas-dust disks (Masset and Papaloizou 2003; Papaloizou et al. 2007), offering a unique opportunity to study this type of migration in Saturn's rings.

In Cassini images of the F ring a pattern called "fans" was observed (Fig. 13.25). These "fans" are essentially the wake pattern induced by embedded moonlets in the dusty component of the F ring.

14.3.4 Dense Narrow Rings

Prominent ringlets in the Saturn system are the Titan ringlet (Porco et al. 1984) at $1.29R_S$ ($R_S = 60,330$ km is Saturn's radius), the Maxwell ringlet at $1.45R_S$ (Esposito et al. 1983; Porco et al. 1984), the Huygens ringlet at $1.95R_S$, and the ringlets in the Encke gap. Other locations are listed in Table II of French et al. and Tables 13.2 and 13.4. The most striking narrow ring of the Saturnian ring is perhaps the F ring, discussed in detail in Chapter 13. AQ10

14.3.4.1 Confinement of Narrow Rings

Goldreich and Tremaine proposed that narrow rings are confined in radius by gravitational torques from neighboring satellites (shepherding). The confinement is due to the transport of angular momentum, induced by disturbances created in the ring by the shepherd satellites. A formula for linear torques (adequate for small perturbations) was derived by Goldreich and Tremaine and nonlinear torques (also valid for large perturbations) were estimated by Borderies et al.

Voyager detected the satellites Prometheus and Pandora on orbits slightly interior and exterior to the F ring. It is clear that the gravitational perturbations of Prometheus induce a wealth of pronounced structures in this ring (Kolvoord et al. 1990; Murray et al. 2008; see also Chapter 13) and both satellites are probably involved in the shepherding. This shepherding role has been questioned (Showalter and Burns 1982; Cuzzi and Burns 1988) on the ground that the F ring seems not to be in torque balance between the two satellites. However, based on the available data an accurate determination of the mass distribution in the F ring is difficult, which would be necessary for the precise evaluation of the torque balance. On the other hand, evidence for perturbations induced in the F ring by Pandora (Porco et al. 2005; Murray 2007) would lend further support to the idea that Prometheus and Pandora act as shepherds of the F ring.

Stewart and Lewis offered an alternative view of the F ring confinement, involving a weakening of the outward flux of angular momentum. In a first phase, the particles migrate to Lindblad resonances, forming ringlets while in a second phase, the ringlets collide and partially merge. This explanation is consistent with results of their N-body simulations. The dynamics of the F ring and Prometheus and Pandora was further studied in Lewis and Stewart.

Hänninen and Salo; Hänninen and Salo found that narrow ringlets can form at isolated Lindblad resonances. Goldreich et al. explained such a single-sided shepherding

as a consequence of the net negative angular momentum flux (i.e. integrated over a streamline) promoted by satellite perturbations of the streamlines of the flow of particles. Lewis and Stewart (2005) showed that a surprisingly complex and variable structure can already arise from the perturbations exerted by one nearby eccentric moon on a narrow, self-gravitating ring of uni-sized particles. Using typical scales and elements for Prometheus and the F ring, their simulations develop many features similar to those seen in the F ring.

Dermott et al. (1980) proposed a confinement of a narrow ring by an embedded ring-moon forcing the particles in the ringlet area to revolve in horseshoe and tadpole orbits. The long-term behavior and the gravitational action of multiple moonlets in a narrow ringlet was studied by Spahn and Sponholz (1989; Spahn et al. 1992b) pointing to the existence of a kilometer-sized moonlet in the F ring's core (Spahn and Wiebicke 1989). Cassini experiments (Esposito et al. 2008; Murray et al. 2008) confirm moonlets populating the F ring which can migrate chaotically (Winter et al. 2007), driven by the shepherds and higher gravity moments due to Saturn's oblateness. If the ringlet contains a large fraction of dust (Showalter et al. 1992; Encke ringlets, F ring) the continuous loss of dust due to non-gravitational perturbations must be balanced by sources in the ringlets (e.g. small moonlets; Ferrari and Brahic 1997), replenishing the dusty material.

Rappaport studied the possible confinement of a large ring by a narrow ring located in a gap at $1.470 R_S$. She found that the torque exerted by the ringlet is able to confine the gap's inner edge, but not the outer edge. This suggests that either the gap's edges are, as the ringlet itself, confined by reversal of the viscous flux of angular momentum, or that one or several small satellites located within the gap are responsible for the confinement of the edges.

14.3.4.2 Rigid Precession

Most narrow rings are eccentric and/or inclined. Goldreich and Tremaine proposed that differential precession (due to the quadrupole moment of the planet) can be balanced by the effect of a ringlet's self-gravity, thus allowing a rigid precession of eccentric ringlets. The dynamics of narrow elliptical rings in the presence of eccentricity excitation by shepherd satellites, self-gravity and viscous forces was studied by Borderies et al. They find that the mean eccentricity of the ringlet is determined by a balance between viscous damping and excitation by the shepherd satellites, and the eccentricity gradient is positive. Due to viscous forces, the line of apsides of the inner and outer edges are not aligned in their model.

Chiang and Goldreich (2000) and Mosqueira and Estrada (2002) studied the effect of particle collisions on the interplay of the effects of planetary oblateness and self-gravity. They show that collisional forces felt by the material in the last $\sim$100 m of a $\sim$10 km wide ring can increase equilibrium ring masses by a factor up to $\sim$100, and can lead to apse alignment of the inner and outer ring edges, in accordance with Voyager radio measurements of the Uranian ε, α, and β rings. Papaloizou and Melita used a fluid dynamics approach to derive a condition for the steady maintenance of the eccentricity of a ring, which requires the external satellite torque to balance the dissipative effects due to collisions. Melita and Papaloizou further considered the case where the pattern frequency of the eccentric ringlet is in a secular resonance with an external satellite. Applying the results to the Titan ringlet (in a 1:0 resonance with Titan), they estimated the mean surface density of the ringlet.

14.3.4.3 Excitation of Eccentricities and Inclinations

Goldreich and Tremaine showed that torques exerted at a Lindblad resonance with a satellite excite eccentricities of the ring particles, while torques exerted at a corotation resonance damp eccentricities. If the corotation resonances are not saturated, these resonances win and the eccentricity of the ring decreases. If the corotation resonances are partially or fully saturated, then the Lindblad resonances win and the eccentricity of the ring increases.

The excitation of inclinations was studied by Borderies et al. Gravitational interaction of rings and satellites at vertical resonances produce a secular increase of their inclination until viscous dissipation leads to an equilibrium. Vertical resonances are similar to Lindblad resonances, involving inclination instead of eccentricity. However, there is no equivalent of the corotation resonances.

14.3.4.4 Viscous Overstability

Longaretti and Rappaport showed that spontaneous oscillations of viscous origin (overstabilities) can arise in a dense narrow ring (see also Papaloizou and Lin 1988). They found two possible regimes of instability, one in which the mean eccentricity of the ring decreases to a small but finite and nearly constant value, while internal modes of libration reach comparable amplitudes. In the other regime the mean eccentricity of the ring increases to a much larger asymptotic value, while internal librations are strongly reduced (though not fully damped). Wave like features in the Maxwell ringlet might be caused by this mechanism (Porco et al. 2005).

14.3.4.5 Ring Edges

Many ringlets have remarkably sharp edges. This can be explained by the reversal of angular momentum luminosity in

the regions of the rings which are strongly perturbed (see Borderies et al. 1982, 1983a, 1989). Angular momentum luminosity is the momentum flux integrated over a streamline, i.e. the rate at which angular momentum crosses the streamline. The perturbed streamlines oscillate with slightly different wavelengths $\lambda = 3\pi x$ (x is the modulus of the difference in semi-major axes of satellite and streamline) so that neighboring streamlines eventually intersect. The intersection occurs at quadrature, midway between periapsis and apoapsis. If the streamlines are sufficiently perturbed, the orbital angular velocity of the particles increases outward at the point of intersection (while for a circular orbit it would decrease). As a consequence, in this region the angular momentum associated with particle collisions flows inward rather than outward. Also, energy is dissipated and the streamline eccentricities are damped. Considering the total angular momentum flux over the 360° azimuth of the streamlines, the net torque due to the collisions between particles can balance the torque exerted by the satellite for a certain distortion of the streamline. A more complete analysis indicates that the balance of the energy dissipation and angular momentum transport occurs well before the hypothetical streamline crossing for $\tau \ll 1$ and close to it for $\tau \gg 1$. A sharp edge forms because the angular momentum balance is established over a few streamlines only. In this picture, the equivalent width of one streamline is the radial width corresponding to the excursions associated with the particle orbital eccentricities.

Hahn et al. (2009) revisited the streamline approach for a ring edge located at a Lindblad resonance with a perturbing satellite. Applying their model to the outer B ring edge, they point at difficulties in achieving the torque balance, unless a fairly high value of the rings bulk viscosity is assumed (see discussion on bulk viscosity in Section 14.1.2.2), or additional friction for the particles' motion is invoked. Shepelyansky et al. have shown that synchronization of the orbital phases of ring particles near the resonance may lead to a decreased collision frequency. As a result, diffusion of particles can be drastically suppressed, which helps to maintain a sharp ring edge.

14.4 Size Distribution and Spins of Ring Particles

Radio and stellar occultations at various wavelengths provide information about the size distribution of ring particles smaller than a few tens of meters, while the size distribution of ~100 m-sized moonlets can be inferred from observation of propeller structures (Section 14.3.3). The importance of accretion and fragmentation for the evolution of the size distribution is implied by the observed shapes and internal densities of small inner satellites, which is supported by dynamical studies (Section 14.4.1).

Oblique impacts between ring particles with rough and irregular surfaces lead inevitably to rotation (Section 14.4.2). Although the rotational states of ring particles are not directly observable, particle spins have been constrained indirectly from observations of the thermal emission from Saturn's rings made by ground-based telescopes, the Pioneer 11 infrared radiometer, Voyager's infrared interferometer spectrometer, and Cassini CIRS (see e.g., Cuzzi et al. 1984; Spilker et al. 2003, 2006). In principle, constraints on the dynamical behavior and physical properties of ring particles can be derived from the comparison of those observations and model calculations including particle spins.

14.4.1 Particle Size Distribution and Its Evolution

14.4.1.1 Particle Size Distribution Derived From Observations

The results of the Voyager 1 radio occultation experiments significantly advanced our knowledge about ring particle size distribution (Marouf et al. 1983, Chapter 15; Zebker et al. 1985, Chapter 15). In this experiment, the radio source onboard Voyager 1 was used to measure the radio opacity at two wavelengths (3.6 and 13 cm). A power-law distribution $n(R) = n(R_0)[R/R_0]^{-q}$ with $R_{\min} < 1$ cm and $R_{\max} \approx 1$ m was assumed, and constraints on the values of q and $n(R_0)$ were derived from the opacities. Also, measurements of the differential scattering cross section and integral inversion were used to derive a general size distribution over the range of $1 R 15$ m. Marouf et al. assumed a many-particle-thick model, while Zebker et al. allowed for a near monolayer system. The results imply that there exists an upper cutoff in the size distribution at $R \sim 5$ m. For centimeter-to-meter-sized particles $q \approx 3$ was found, with a slightly larger value for the C ring ($q \approx 3.1$), and slightly smaller in the Cassini Division and the A ring (~2.7–3.0; Chapter 15). A tendency of increasing q was also found from the inner to the outer A ring, which indicates a greater abundance of small particles in the outer A ring (Tyler et al. 1983). The observation that the optical depth is similar at visible and radio wavelengths suggests that sub-centimeter particles do not dominate the surface area. The Cassini RSS occultations support these earlier results (chapter by 15).

French and Nicholson derived the particle size distribution in Saturn's rings from ground-based observations of the 3 July 1989 stellar occultation of 28 Sgr, and the Voyager photopolarimeter (PPS) optical depth profile. They used the

PPS occultation data (Esposito et al. 1983) to estimate and then remove the directly transmitted signal from the 28 Sgr observations, and derived particle size distributions from the so obtained high SNR scattered light profiles at wavelengths of 3.9, 2.1, and 0.9 μm. Using a two-dimensional forward-scattering model with the many-particle-thick-layer approximation and a single power-law size distribution for each major ring region, they obtained values for q, $R_{\min}$, and $R_{\max}$ for each region, including the B ring, for which the Voyager radio occultation experiment was unable to derive the particle size distribution due to its high opacity. The results for q and $R_{\max}$ derived for the A and C rings were fairly consistent with those obtained by the Voyager radio occultation measurements, although the values of $R_{\max}$ obtained by French and Nicholson were somewhat larger ($R_{\max} = 10$m for the C ring, and 20 m for other locations). The values of $R_{\min}$ for the inner A ring and the B ring were as large as 30 cm, while a greater population of small particles with $R_{\min} = 1$ cm was suggested for the C ring and the outer A ring.

An independent estimate of the size of the largest particles was obtained by an analysis of the statistical properties of the Voyager PPS stellar occultation data by Showalter and Nicholson. Owing to the finite size of ring particles, the variance of the photon counts during stellar occultation can be significantly larger than expected from Poisson statistics. Showalter and Nicholson derived an expression for the noise in the PPS scan due to large particles, and used the measured noise to constrain their sizes. The excess variance depends on the fourth moment of the particle size distribution. Showalter and Nicholson expressed their results in terms of an effective radius defined by $R_{eff}^2 = \int_{R_{\min}}^{R_{\max}} R^4 n\,(R)\,dR / \int_{R_{\min}}^{R_{\max}} R^2 n\,(R)\,dR$, finding $R_{eff} \approx 2 - 10$ m in the main rings (Chapter 15). French and Nicholson calculated the values of R_{eff} defined above, using the size distribution derived from their observations, and found excellent agreement with the estimates by Showalter and Nicholson.

The surface mass densities estimated from the size distribution by French and Nicholson are much larger than those derived from studies of density and bending waves. Their large mass densities for the A and B rings ($q < 3$) reflect their inferred value of $R_{\max} \approx 20$ m. The disagreement may suggest that the largest particles with $R \approx R_{\max}$ actually represent loosely bound aggregates of meter-sized objects in gravitational wakes (French and Nicholson 2000). A smaller value of $R_{\max}$ would lead to smaller surface mass densities consistent with density and bending wave studies. Strong gravitational wakes can also affect the apparent particle size distribution, by enhancing the release of impact-debris or stirring up small particles (Sremčević et al. 2007, Sections 1.3 and 3.3; Robbins et al. 2009, Sections 1.3 and 3.3).

The number of particles larger than the upper cutoff of 5–20 m is much smaller than extrapolation of the $q \approx 3$ power-law would predict. The power-law index for moonlets with R10 m estimated from the analysis of propeller structures in the A ring (Section 14.3.3) is $q \approx 5$ (Tiscareno et al. 2006), $q \approx 6$ (Tiscareno et al. 2008), and $q \approx 9$–11 (Sremčević et al. 2007).

14.4.1.2 Accretion of Particles in the Roche Zone

The evolution of the size distribution due to gravitational accretion and fragmentation has been extensively studied in the context of accumulation of planetesimals in the protoplanetary disk (e.g., Wetherill and Stewart 1993; Weidenschilling et al. 1997). Planetary accretion occurs far outside the Sun's Roche limit, and the effect of tidal forces on the outcome of planetesimal collisions can be neglected. However, the tidal effect is significant in the Roche zone, where planetary rings are located. The Roche limit a_R, which is defined as

$$\frac{a_R}{r_{plan}} = 2.456 \left(\frac{\rho_{plan}}{\rho} \right)^{1/3}, \tag{14.83}$$

is the distance inside which no figure of hydrostatic equilibrium exists (e.g., Roche 1847; Chandrasekhar 1969), and is not the distance at which a planet's tidal force exceeds a satellite's gravitational attraction. Thus, gravitational accretion is possible in the Roche zone under certain conditions (e.g., Smoluchowski 1979, Chapter 17; Dobrovolskis and Burns 1980, Chapter 17; Davis et al. 1984, Chapter 17; Weidenschilling et al. 1984, Chapter 17).

The condition that the attraction between two radially aligned, synchronously rotating particles in contact with mass ratio μ exceeds the tidal force due to the planet is (e.g., Weidenschilling et al. 1984)

$$\frac{a}{r_{plan}} > \left(\frac{3\rho_{plan}}{\rho} \right)^{1/3} \frac{1 + \mu^{1/3}}{(1+\mu)^{1/3}}. \tag{14.84}$$

In terms of the ratio of the sum of the physical radii of the colliding particles to their mutual Hill radius denoted by r_p (or $r_h = r_p^{-1}$; Eq. 14.38), this condition reads $r_p < 1$ (or $r_h > 1$). Figure 14.17a shows the values of r_p in Saturn's rings, as a function of the distance from Saturn and the mass ratio of colliding particles; for icy particles around Saturn this condition gives $a > 126{,}000$ and 80,000 km for identical particles or for very differently sized particles, respectively. On the basis of this criterion, Weidenschilling et al. (1984) and Davis et al. argued that particle collisions should produce accretion in Saturn's rings, especially in the A ring, and that the rapid accretionary processes are counterbalanced by tidal disruption of the larger accreted aggregates, which they called "dynamic ephemeral bodies." Salo confirmed the formation of

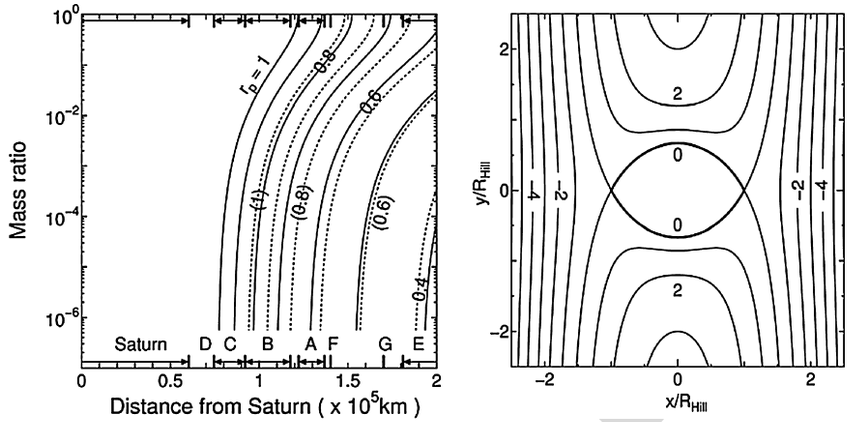

Fig. 14.17 (**a**) Contours of r_p as a function of the distance from Saturn and the mass ratio of colliding particles. Solid lines show the case with a particle internal density of $0.9\,\mathrm{g\,cm^{-3}}$ ($0.4\square \leq r_p\square \leq 1$, with an increment of 0.1), while the dotted lines represent the case with $0.5\,\mathrm{g\,cm^{-3}}$ ($0.5\square \leq r_p \leq \square 1$). The radial locations of Saturn's rings are also shown. (**b**) Contours of the Hill potential U for the $z = 0$ plane. Contour lines inside the Hill region are not shown

AQ11

gravitational wakes and aggregates in Saturn's rings by local N-body simulations (Section 14.1.3).

On the other hand, Ohtsuki derived accretion criteria for colliding particles from an energy perspective, considering both relative kinetic and potential energies under the Hill approximation in the three-body problem. The linearized equations of relative motion of the two particles in a local coordinate system rotating with the Keplerian angular velocity Ω are written as

$$\begin{aligned} \ddot{x} &= 2y\Omega + 3x\Omega^2 - \frac{G\,(m_1+m_2)\,x}{r^3} \\ \ddot{y} &= -2x\Omega - \frac{G\,(m_1+m_2)\,y}{r^3} \\ \ddot{z} &= -z\Omega^2 - \frac{G\,(m_1+m_2)\,z}{r^3} \end{aligned} \tag{14.85}$$

where the x-axis points radially outward, the y-axis in the direction of orbital motion, the z-axis is perpendicular to the x-y plane, and $r = \left(x^2+y^2+z^2\right)^{1/2}$. On the right-hand side of Eq. 14.85, the $2\dot{y}\Omega$ and $-\dot{x}\Omega$ terms represent Coriolis forces; $3x\Omega^2$ and $-z\Omega^2$ are the tidal terms; and those proportional to $1/r^3$ represent the mutual gravity between the two particles. Equation 14.85 hold a constant of motion

$$E = \frac{1}{2}\left(x^2+y^2+z^2\right) + U\,(x,y,z)\,, \tag{14.86}$$

where $U\,(x,y,z)$ is the Hill potential given as

$$U\,(x,y,z) = -\frac{3}{2}x^2\Omega^2 + \frac{1}{2}z^2\Omega^2 - \frac{G\,(m_1+m_2)}{r} + \frac{9}{2}R_{Hill}^2\Omega^2. \tag{14.87}$$

A constant $(9/2)\,R_{Hill}^2\Omega^2$ has been added so that U vanishes at the Lagrangian points $(x,y,z) = (\pm R_{Hill}, 0, 0)$. The contour lines of the Hill potential at the $z = 0$ plane are shown in Fig. 14.17b (see, e.g., Nakazawa and Ida 1988). The $U = 0$ surface defines the Hill sphere, which is actually lemon-shaped with a half-width of unity in the radial direction, 2/3 in the azimuthal direction, and $\approx$0.638 in the vertical direction. Since the Hill sphere is identical to the $U = 0$ surface and $U < 0$ inside the sphere, only particles with positive E can enter the sphere, and they cannot escape out of the sphere if their energy is reduced to negative values by an inelastic collision. Therefore, the criteria for gravitational accretion are (i) the relative position (x,y,z) must be inside the Hill sphere, and (ii) $E < 0$ after impact.

Gravitational accretion is inhibited at the radial locations close to the planet where $r_p > 1$ (or $r_h < 1$), while colliding pairs with an arbitrary mass ratio can become gravitationally bound in the outermost part of the ring system where $r_p \ll 1$ (or $r_h \gg 1$), if there is sufficient energy dissipation in a collision. In the intermediate region, gravitational accretion is possible for particles which differ greatly in mass, while like-sized particles overflow their mutual Hill sphere and cannot remain gravitationally bound. Numerical results of three-body orbital integration show that the capture probability decreases abruptly for $r_p \geq 0.7$, because particles overflow the Hill sphere in the azimuthal direction when $r_p > 2/3$ (Ohtsuki 1993, Fig. 14.18a). The capture probability increases when surface friction is taken into account, while it decreases significantly when the relative random velocity becomes comparable to or larger than the escape velocity (Ohtsuki 1993, Fig. 14.18b; Morishima and Salo 2004, Fig. 14.18b). Neglecting the tidal terms in the Hill potential, Ohtsuki obtained an analytic expression for

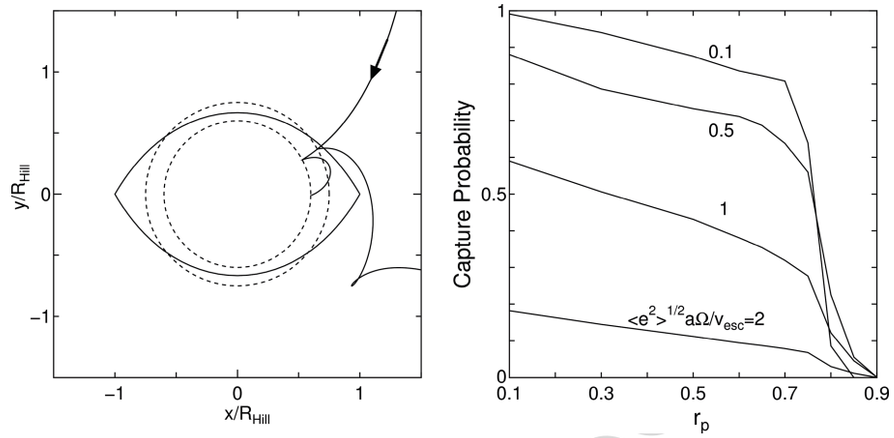

Fig. 14.18 (**a**) Examples of particle orbits leading to collision with targets of different values of r_p (0.6 and 0.75). In the case of $r_p = 0.6$, the orbit leads to accretion (i.e., E becomes negative) after two impacts, while the orbit in the case of $r_p = 0.75$ results in escape after the first collision (Redrawn from Ohtsuki). (**b**) Capture probability averaged over the Rayleigh distribution of particles' eccentricities and inclinations obtained by three-body orbital integration is shown as a function of r_p. $< e^2 >^{1/2} a\Omega/v_{esc}$ represents particles' random velocity scaled by their escape velocity. The values of the normal and tangential coefficients of restitution are 0.5 and 0.9, respectively

the capture probability in the case of $r_p \ll 1$ and relative random velocity larger than the escape velocity. Canup and Esposito derived a simple expression for the capture criterion by retaining the tidal terms and performing an angle-average (Chapter 17). The derived criteria are roughly consistent with the numerical results of Ohtsuki for low random velocities. Cohesive forces between Saturn's ring particles may extend the zone for particle accretion radially inward and allow small particles to be deposited on larger ones to form regolith layers (Albers and Spahn 2006).

In dense rings, collective effects among more than two particles are important (Salo 1992a, Section 1.3, 1995, Section 1.3). Using N-body simulation, Karjalainen and Salo examined the criterion for aggregate formation in detail. Results of their simulations with equal-sized particles in Saturn's rings with $\rho = 0.9\,\mathrm{g\,cm^{-3}}$, and a velocity-dependent normal coefficient of restitution, based on Bridges et al., showed that formation of transient aggregates should occur beyond $a \approx 137{,}000$ km and stable aggregates form beyond $a \approx 146{,}000$ km, respectively. The critical radial location for the formation of stable aggregates corresponds to $r_p \sim 0.84$ ($r_h \sim 1.2$), which is slightly larger than the afore mentioned $r_p \sim 0.7$ criterion based on three-body calculations. This indicates that gravitational accretion is facilitated by many-body effects, as compared to accretion between two solid bodies. Karjalainen and Salo also showed that the inclusion of the particles' surface friction and/or size distribution facilitates accretion, shifting the above accretion region by about 5,000 and 10,000 km, respectively. Karjalainen performed N-body simulations of impacts between gravitational aggregates in Saturn's rings, and found that impacts between aggregates, with mass ratios from 1 to 10, result on average in disruption, while net accretion typically should occur at $a > 145{,}000$ km. The shapes of the aggregates formed in simulations are well described with Roche ellipsoids, approaching spherical shapes as the distance increases (Karjalainen and Salo 2004).

Porco et al. noted that accretion is facilitated if under-dense ring particles accumulate around a high-density core, as compared to the case of accretion of low-density particles without core: under-dense particles are inferred from comparison between dynamical simulations and observational signatures of gravitational wakes (Section 14.1.3). The mean density of such an aggregate which has a high-density core decreases with increasing size due to accretion of particles. Therefore the size of the aggregate's Hill sphere grows more slowly than its physical size. As a result, accretion is halted when particles fill the aggregate's Hill sphere. Porco et al. analyzed Cassini images of Saturn's small inner satellites to derive their sizes, shapes, and mean densities. They found that the long axes of Pan, Daphnis, Atlas, and Prometheus agree within 15% with the long axis of the Hill sphere for a body of the given satellite mass and orbit. They also confirmed the above process of particle accretion around a high-density core using N-body simulation. Moreover, Cassini images revealed that Pan and Atlas have equatorial ridges, which may have formed by preferential accretion of ring particles onto the equatorial surfaces of already-formed satellites embedded in the rings (Charnoz et al. 2007, Chapter 17).

14.4.1.3 Processes and Models for Particle Size Evolution

Multiple processes must have been involved to produce the observed size distribution of ring particles and small

moonlets. Studies of the size evolution of asteroids through a collisional cascade show that a power-law $n(R)dR \propto R^{-q}dR$ with $q = 3.5$ is expected in steady state if the dependence of the critical specific energy for fragmentation on target size is neglected (e.g., Dohnanyi 1969; Williams and Wetherill 1994; Tanaka et al. 1996; Durda et al. 1998). Additional processes, including the tidally modified accretion in the Roche zone described above, are likely to play a role for the size evolution of ring particles. The role of satellite fragmentation and tidally modified accretion in the origin and evolution of ring systems is further discussed in Chapter 17.

Davis et al. and Weidenschilling et al. examined the evolution of the particle size distribution in a planetary ring, using a statistical simulation that includes accretion, rebound, as well as the collisional and tidal disruption of particles. They found that their simulation can reproduce the size distribution inferred from the Voyager observation (Marouf et al. 1983), if tidal disruption is assumed to occur at $R = 10$ m, producing large fragments and a shower of small particles with a power-law size distribution. Longaretti developed an analytic theory for the particle size distribution and argued that the upper cutoff can be explained by efficient collisional erosion of the large particles.

Esposito and Colwell and Colwell and Esposito; Colwell and Esposito (also Colwell et al. 2000) considered the evolution of the sizes of satellites and their fragments around Uranus and Neptune due to meteoroid impacts. Their simulations showed that once the initial disruption of a parent satellite occurs, subsequent disruptions of its fragments occur relatively quickly. Their earlier simulations, which used the critical impact energy for catastrophic fragmentation based on a scaling theory (e.g., Housen and Holsapple 1990), showed that many of the small moons of Uranus and Neptune have lifetimes against catastrophic disruption shorter than the age of the solar system (Colwell and Esposito 1992). These lifetimes are significantly longer when the criterion for catastrophic disruption based on the asteroid collisional evolution model of Durda et al. (1998) or from hydrodynamic impact simulations (Benz and Asphaug 1999) is used. Colwell et al. found that a model intermediate to that of the scaling theory and that of Durda et al. would allow the fragments from a 10–20 km radius parent satellite to produce a more steady population of rings, moonlet belts, and small moons.

Canup and Esposito considered the effect of accretion and performed numerical simulations of the accretional growth of a disrupted satellite. In the Roche zone where only bodies which differ greatly in mass can remain gravitationally bound, Canup and Esposito (1995) found that a fragmentation-produced debris distribution basically evolved into a bimodal population, with one element consisting of a swarm of small, high-velocity bodies and the other composed of a small number of large moonlets with low random velocities. Canup and Esposito applied a similar model to Saturn's G ring, and found that evolution from the disruption of a 1.5–3 km progenitor satellite can explain the G ring's particle and dust population inferred from observations (Showalter and Cuzzi 1993; Gurnett et al. 1983; Van Allen 1983). Barbara and Esposito performed simulations of collisional evolution of particles in the F ring, including accretion and fragmentation. They argued that collisions between moonlets (which themselves formed as a result of accretion) can explain the anomalous localized brightenings in the F ring observed by Voyager (Showalter 1998).

The size and spatial distributions of the 20–250 m radius moonlets, derived from the propeller structures observed in the A ring region by Cassini, also provide a clue to the evolution of the size distribution of rings and moonlets. As we mentioned before, the derived size distribution for propeller moons has a larger power-law index compared to $q \approx 3$ for ring particles with R10 m (Tiscareno et al. 2006, 2008; Sremčević et al. 2007). Moreover, Sremčević et al. found that the propeller structures are concentrated in a narrow 3,000-km-wide annulus at $a \approx 130{,}000$ km. On the basis of these observations, they proposed an explanation that such embedded moonlets are remnants of fragments of a ring-moon of Pan size or larger disrupted by a meteoroid impact. Large fragments produced by the disruption evolve by further shattering by meteoroid bombardment, explaining the steepened size distribution of the moonlets responsible for the propeller structures. They argue that the steepness of the moonlets' size distribution and their apparent lack in the rest of the A ring represent different phases of the moonlet destruction and subsequent evolution.

As we mentioned earlier, observations suggest $R \approx$ 0.1–30 cm as a minimum particle size depending on the radial location in Saturn's rings (French and Nicholson 2000). Poynting-Robertson drag (loss of orbital angular momentum by absorption and reemission of radiation) and plasma drag (angular momentum transfer due to physical collisions and/or long-range charged particle interactions between ring particles and ions and electrons tied to the planet's magnetic field) are the important mechanisms of removal of micrometer-sized ring particles Burns et al.

As another possible mechanism, the removal of small ring particles due to thermal torques has been recently proposed. The effect of thermal torques produced by the absorption and re-emission of sunlight from an asteroid's surface on its orbital evolution is called the Yarkovsky effect (e.g., Bottke et al. 2002). Similar effects on small particles in Saturn's rings, i.e. thermal torques due to Saturn shine and the torques due to illumination by the sun (the Yarkovsky–Schach effect) have been recently studied by Rubincam and Vokrouhlický et al. The removal of subcentimeter-sized particles due to thermal torques may help to explain the observed paucity of such small particles in Saturn's rings. However, frequent collisions of the small particles with large ring particles will

rapidly re-distribute any extra torque received by the small particles over the whole population. For this reason the evolution of the small particles, most sensitive to the Yarkovsky and Yarkovsky–Schach effects, cannot be considered independently from the the large particles. Further studies including the effects of particle collisions and resonances are needed to clarify such effects on the long-term orbital evolution of the ring particle size distribution.

14.4.2 Particle Spins

14.4.2.1 Dynamical Studies

For rings consisting of non-gravitating equal-sized particles on circular orbits undergoing inelastic collisions due to Kepler shear, the particles' rotation rate ω is expected to be on the order of the orbital angular velocity Ω (e.g., Weidenschilling et al. 1984). Detailed calculations, using N-body simulation, show that spin rates follow a Gaussian distribution with mean spin rate being slow prograde rotation with $\langle\omega\rangle/\Omega \sim 0.3$–$0.5$, both in cases of non-gravitating and gravitating particles (Salo 1987a, b, 1995; Richardson 1994; Ohtsuki and Toyama 2005). However, the dispersion of spins can be much larger, scaling as $\sqrt{\langle\Omega^2\rangle}/\Omega \propto c/R\Omega$, where the proportionality constant depends on the coefficient of tangential friction[7], ε_t. Besides friction, also small-scale deviations from spherical size are efficient in promoting particle spins (Salo 1987a, b).

Because of the additional energy dissipation due to surface friction, inclusion of rough surfaces and particle spins allow a large critical value (ε_{cr}) of the normal restitution coefficient for the thermal stability discussed in Section 14.1.1.3 (Salo 1987a, b; Araki 1988, 1991; Morishima and Salo 2006; Ohtsuki 2006a). The strength of surface friction also determines the ratio of the particles' rotational energy $E_{rot} = mR^2\langle\Omega^2\rangle/5$ (for a uniform sphere with mass m) and kinetic energy E_{kin}. In the non-gravitating case, this ratio in the equilibrium state is obtained analytically (Salo 1987a; Morishima and Salo 2006) as

$$\frac{E_{rot}}{E_{kin}} = \frac{2\,(1-\varepsilon_t)}{14-5\,(1-\varepsilon_t)},$$

which shows that equipartition between random motion and spins is not realized, unless surface friction is extremely strong (i.e. $\varepsilon_t = -1$). Compared to a system of smooth particles, the inclusion of energy dissipation due to friction slightly decreases the equilibrium velocity dispersion in the non-gravitating case as well as for gravitating particles in a low optical depth ring. In self-gravitating rings of larger optical depth, i.e. where gravitational wakes are formed, the additional energy dissipation due to surface friction facilitates the formation of gravitational wakes, and thus tends to slightly increase velocity dispersion (Salo 1995). However, such an effect is minor as compared to the major effect of self-gravity in dense rings.

As an extreme case of the rotational evolution due to collisions between particles with different sizes, the spin of a moonlet embedded in a ring of small equal-sized particles was studied in terms of three-body calculations and N-body simulations (Morishima and Salo 2004; Ohtsuki 2004a, b). Calculations show that the moonlet's rotation reaches an equilibrium state of slow prograde spin with $\langle\omega\rangle/\Omega \sim 0.3$–$0.5$ when ring particles are much smaller than the moonlet, while the moonlet can spin both in prograde and retrograde directions when the particle size is comparable to the moonlet size.

The spin state of ring particles with size distribution was examined in N-body simulations for various cases, including dense self-gravitating rings (Salo 1987b; Richardson 1994; Ohtsuki and Toyama 2005; Morishima and Salo 2006), while analytic approaches and numerical three-body calculations were used to study the size-dependence of rotation rates in low-optical depth rings (Ohtsuki 2005, 2006a, b). Results of these studies show that large particles spin slowly, with mean spin period comparable to the orbital period, and a spin dispersion which is much smaller than the mean, while small particles generally spin much faster, with a dispersion that considerably exceeds the mean.

In the case of an extended size distribution, the spin period was found to be roughly proportional to the particle size (Fig. 14.19). Rapidly spinning small particles have larger orbital inclinations than slowly spinning large particles (Salo and Karjalainen 2003; Ohtsuki 2005, 2006b; Morishima and Salo 2006); thus, the ring particles' rotational states have vertical heterogeneity. The spin axes of slowly spinning large particles tend to be aligned normally to the ring plane, while the small particles' spin axes are nearly randomly distributed (see Fig. 14.9 in Salo 1987b; Ohtsuki and Toyama 2005). Since in the case of a continuous size distribution the rotation frequency of the largest particles is on the order of Ω, and that of small particles is roughly inversely proportional to the particle radius, the values of the rotation rates of smaller particles depend on the size of the largest particles. The overall rotation rates also tend to increase slightly for stronger surface friction and/or a shallower size distribution of particles, but the R^{-1}-dependence of the rotation rates is insensitive to the values of these parameters (Ohtsuki 2005, Fig. 19, 2006b, Fig. 19; Morishima and Salo 2006, Fig. 19).

[7] ε_t is defined so that the tangential component of the relative velocity of the two contacting points is changed by a factor of ε_t ($-1\square \leq \varepsilon_t \leq \square 1$) due to collision. Perfectly smooth spheres have $\varepsilon_t = 1$ while perfectly rough spheres have $\varepsilon_t = -1$ (Araki and Tremaine, 1986).

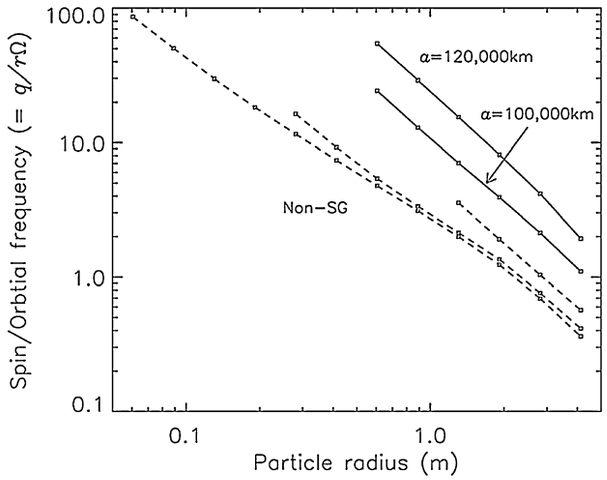

Fig. 14.19 Results of N-body simulations for the rotation rates of particles in units of orbital angular velocity (i.e., $q \equiv R\langle\Omega^2\rangle^{1/2}$), as a function of particle radius. Solid lines show results for self-gravitating particles at two different radial locations around Saturn ($\varepsilon_n = \varepsilon_t = 0.5$). Dashed lines represent results for non-gravitating particles with different widths of the particle size distribution (Morishima and Salo, 2006)

In the case of rings with low optical depth, the rate of change of the mean rotational energy of particles with mass m due to collisions with other particles with mass m' can be written as

$$\frac{dE_{rot}(m)}{dt} = \int n_s(m')\{C_{CS} + (E_{rot}(m') - E_{rot}(m))\, C_{RF}\}dm', \tag{14.88}$$

where C_{CS} and C_{RF} are the rate coefficients, which depend on the particles' relative random velocity and can be evaluated by three-body calculation (Ohtsuki 2005, 2006a). The first term in parentheses in the integrand represents energy exchange between random motion and rotation ('collisional stirring'), while the second term tends to equalize the mean rotational energy among particles with different sizes and to decrease the rotation rates of large particles ('rotational friction', by analogy with the dynamical friction term in the velocity evolution equation; see Eq.14.16). Because of the former effect, equipartition of rotational energy among particles with different sizes (which would imply $\langle\Omega^2\rangle^{1/2} \propto R^{-5/2}$) is not realized.

14.4.2.2 Relation to Observations of the Rings' Thermal Emission

While the primary heat source for the rings is the sunlight, thermal radiation and reflected sunlight from Saturn also contribute to the heating of the rings. Also, mutual heating between nearby particles can be significant when the ring is dense enough (Aumann and Kieffer 1973; Spilker et al. 2003). The response of ring particles to such heating depends on their physical and dynamical properties, including albedo, thermal inertia, and spin rates. Observations of the thermal response of the rings during and after eclipse suggest low thermal inertia of ring particles, with a thermal relaxation time of about one hour, i.e. about one tenth of an orbital period (e.g., Froidevaux et al. 1981; Spilker et al. 2003; Ferrari et al. 2005). In this case, particles with spin period much longer than the thermal relaxation time can be regarded as slow rotators, which radiate their thermal emission mainly from the face illuminated by the sunlight, while fast rotators with random spin orientations radiate over their whole surface area (Froidevaux 1981; Kawata 1983). Furthermore, in dilute rings, some fraction of fast rotators have their spin axes pointing nearly toward the Sun. The north and south sides of such a particle with respect to its spin axis can have a temperature contrast regardless of the rotation rate, if the interval of collisions that would change the spin orientation is longer than the thermal relaxation time (Morishima and Salo 2006).

Comparison between observations of the rings' thermal emission with model calculations provides constraints on physical properties as well as spin states and structure of the rings (e.g., Froidevaux 1981; Kawata 1983; Esposito et al. 1984; Spilker et al. 2003; Ferrari and Leyrat 2006). Cassini CIRS has acquired an extensive set of thermal measurements of Saturn's main rings for a number of different viewing geometries (Spilker et al. 2006; Leyrat et al. 2008; Altobelli et al. 2007). For example, the observed temperature decrease with increasing solar phase angle suggests that the rings include a population of slow rotators. However, the spin states of particles depend on their sizes, as mentioned above. Furthermore, the thermal emission of the rings likely depends on the particles' vertical distribution and the rate of vertical mixing as well as on the rings' fine structure, such as gravitational wakes in the A ring (Leyrat et al. 2008; Ferrari et al. 2009; Morishima et al. 2009a, b). Further studies using models that include such effects and detailed comparison with observations will provide unique constraints on physical and dynamical properties of ring particles.

14.5 Open Problems

Cassini has considerably advanced our understanding of the dynamics of Saturn's dense rings. Naturally, new questions arise and problems remain open.

An outstanding problem of ring dynamics remains the pronounced structure of the B ring, notably region B2 where the ring alternates between states that are practically opaque and states of moderate optical depth (see Chapter by 13, and

their Fig. 14.14). It seems clear that classical viscous instability will not work here, still, the fact that this instability would produce a bimodal pattern of optical depth is compelling. In this chapter we have shown how the stability properties of the rings can drastically depend on the elasticity of the ring particles. The study of the influence of a particle-size dependence of elastic properties on the ring dynamics has only started. In particular in an interplay with adhesion and self-gravity this might well lead to new types of instabilities (or modification of old ones) applicable to Saturn's rings.

There are several Cassini observations that point at local changes in the particle size distribution in perturbed ring regions. One example are the propellers, where the brightness of the propeller streaks relative to the surrounding ring is difficult to understand. A plausible explanation is the release of small particles, otherwise sticking on the large ring-particles, in those regions that are most perturbed. Another example are the halos around strong density waves observed in the A ring (Dones et al. 1993; Nicholson et al. 2008). They can be similarly interpreted as the effect of small particles locally released from the large ones where the density waves perturb the ring (Nicholson et al. 2008). The third example is the outermost region of the A ring outside the Keeler gap. There the amplitude of the ring's brightness asymmetry is very small, if any. This means that the self-gravity wakes either do not form here, or they are hidden by some process. One possibility is that the combined perturbations of the numerous resonances with Pandora and Prometheus in that region lead to a release of small particles, decreasing the contrast between the crests and troughs of self-gravity wakes, and, in this way, the amplitude of the brightness asymmetry. Altogether this implies that ring particles are loosely bound aggregates, as predicted by Davis et al. (1984; Weidenschilling et al. 1984). Their size is determined by a balance of coagulation and fragmentation, which in turn depends on the typical speed of particle collisions, so that a local increase in the velocity dispersion, induced by external perturbations, leads to a gradual breakup of the aggregates, changing the size distribution. The consequences of such a variable size distribution for the ring dynamics (e.g. properties of self-gravity wakes, density waves, or instabilities) has not been studied so far.

AQ12

One challenge for future study is a unified description of ring dynamics and self-gravity wakes. This might significantly change the conclusions drawn from uniform ring models using approximations of self-gravity. For example, the interaction self-gravity wakes with periodically expanding and contracting density waves might well lead to non-trivial effects on the dispersion relation and the damping of the wave. On the other hand the perturbed ring state in the density wave region can alter the properties of the wakes.

Another question is the relation between viscous overstability and density waves. In fact, spontaneous overstable waves and density waves obey the same dispersion relation. In the derivation of the formula for the damping of tightly wound waves, in the simple hydrodynamic treatment of Shu, the density dependence of the viscosity has been neglected. Such a term would, however, strongly modify the damping behavior of the wave in that model, as noted by Goldreich and Tremaine (1978b). Therefore, the viscosities fitted from that model should be taken with care. Future study could address the question if density waves can undergo an instability similar to the viscous overstability. If this is the case, then the resonance might even lead to such a strong perturbation of the ring that no regular density wave-train is seen. For instance the Janus/Epimetheus 2:1 and 4:3 resonances lead to pronounced density waves in the inner B ring and inner A ring, respectively, while it is a puzzle that the strong 3:2 resonance in the outer B ring does not produce a wave.

Acknowledgment This work was supported by DLR and DFG (JS and FS), NASA (KO), the CASSINI project (NR), and the Akademy of Finland (HS). We would like to thank the reviewers for their thorough and constructive reports and Larry Esposito for his comments on the manuscript.

References

Albers, N. and Spahn, F. (2006). The influence of particle adhesion on the stability of agglomerates in Saturn's rings. *Icarus*, 181:292–301.

Altobelli, N., Spilker, L., Pilorz, S., Brooks, S., Edgington, S., Wallis, B., and Flasar, M. (2007). C ring fine structures revealed in thermal infrared. *Icarus*, 191:691–701.

Araki, S. (1988). The dynamics of particle disks. II. Effects of spin degrees of freedom. *Icarus*, 76:182–198.

Araki, S. (1991). The dynamics of particle disks III. Dense and spinning particle disks. *Icarus*, 90:139–171.

Araki, S. and Tremaine, S. (1986). The dynamics of dense particle disks. *Icarus*, 65:83–109.

Aumann, H. H. and Kieffer, H. H. (1973). Determination of particle sizes in Saturn's rings from their eclipse cooling and heating curves. *Astrophys. J.*, 186:305–311.

Barbara, J. M. and Esposito, L. W. (2002). Moonlet collisions and the effects of tidally modified accretion in Saturn's F ring. *Icarus*, 160:161–171.

Benz, W. and Asphaug, E. (1999). Catastrophic disruptions revisited. *Icarus*, 142:5–20.

Binney, J. and Tremaine, S. (1987). *Galactic Dynamics*. Princeton, NJ, Princeton University Press, 1987, p 747.

Borderies, N., Goldreich, P., and Tremaine, S. (1982). Sharp edges of planetary rings. *Nature*, 299:209–211.

Borderies, N., Goldreich, P., and Tremaine, S. (1983a). Perturbed particle disks. *Icarus*, 55:124–132.

Borderies, N., Goldreich, P., and Tremaine, S. (1983b). The dynamics of elliptical rings. *Astron. J.*, 88:1560–1568.

Borderies, N., Goldreich, P., and Tremaine, S. (1984a). Excitation of inclinations in ring-satellite systems. *Astrophys. J.*, 284:429–434.

Borderies, N., Goldreich, P., and Tremaine, S. (1984b). Unsolved problems in planetary ring dynamics. In Greenberg, R. and Brahic, A., editors, *Planetary Rings*, pp. 713–734, Tucson Arizona, University of Arizona Press.

Borderies, N., Goldreich, P., and Tremaine, S. (1985). A granular flow model for dense planetary rings. *Icarus*, 63:406–420.

Borderies, N., Goldreich, P., and Tremaine, S. (1986). Nonlinear density waves in planetary rings. *Icarus*, 68:522–533.

Borderies, N., Goldreich, P., and Tremaine, S. (1989). The formation of sharp edges in planetary rings by nearby satellites. *Icarus*, 80:344–360.

Bottke, W. F., Vokrouhlický, D., Rubincam, D. P., and Broz, M. (2002). The effect of yarkovsky thermal forces on the dynamical evolution of asteroids and meteoroids. In Bottke, W. F. J., Cellino, A., Paolicchi, P., and Binzel, R. P., editors, *Asteroids III*, pp. 395–408, Tucson Arizona. University of Arizona Press.

Brahic, A. (1977). Systems of colliding bodies in a gravitational field. I – Numerical simulation of the standard model. *Astron. Astrophys.*, 54:895–907.

Bridges, F., Hatzes, A., and Lin, D. (1984). Structure, stability and evolution of Saturn's rings. *Nature*, 309:333–338.

Bridges, F., Supulver, K. D., Lin, D., Knight, R., and Zafra, M. (1996). Energy loss and sticking mechanisms in particle aggregation in planetesimal formation. *Icarus*, 123:422–435.

Brilliantov, N. V. and Pöschel, T. (2004). *Kinetic Theory of Granular Gases*. Oxford, Oxford University Press, 2004, 340 p.

Brilliantov, N., Spahn, F., Hertzsch, J.-M., and Pöschel, T. (1996). Model for collisions in granular gases. *Phys. Rev. E*, 53:5382–5392.

Brilliantov, N. V., Albers, N., Spahn, F., and Pöschel, T. (2007). Collision dynamics of granular particles with adhesion. *Phys. Rev. E*, 76(5):051302.

Burns, J. A., Showalter, M. R., and Morfill, G. E. (1984). The ethereal rings of Jupiter and Saturn. In Greenberg, R. and Brahic, A., editors, *Planetary Rings*, pp. 200–272, Tucson Arizona. University of Arizona Press.

Burns, J. A., Tiscareno, M. S., Spitale, J., Porco, C. C., Cooper, N. J., and Beurle, K. (2008). Giant propellers Outside the Encke gap in Saturn's rings. In *AAS/Division for Planetary Sciences Meeting Abstracts*, volume 40 of *AAS/Division for Planetary Sciences Meeting Abstracts*, page 30.07.

Camichel, H. (1958). Mesures photométriques de Saturne et de son anneau. *Annales d'Astrophysique*, 21:231–242.

Canup, R. M. and Esposito, L. W. (1995). Accretion in the Roche zone: Co-existence of rings and ringmoons. *Icarus*, 113:331–352.

Canup, R. M. and Esposito, L. W. (1997). Evolution of the G ring and the population of macroscopic ring particles. *Icarus*, 126:28–41.

Chandrasekhar, S. (1969). *Ellipsoidal Figures of Equilibrium*. New Haven, Yale University Press.

Chapman, S. and Cowling, T. G. (1970). *The Mathematical Theory of Non-Uniform Gases. An Account of the Kinetic Theory of Viscosity, Thermal Conduction and Diffusion in Gases*. Cambridge, Cambridge, University Press, 1970, 3rd edn.

Charnoz, S., Brahic, A., Thomas, P., and Porco, C. (2007). The equatorial ridges of Pan and Atlas: Terminal accretionary ornaments? *Science*, 318:1622–1624.

Chiang, E. I. and Goldreich, P. (2000). Apse alignment of narrow eccentric planetary rings. *Astrophys. J.*, 540:1084–1090.

Colombo, G., Goldreich, P., and Harris, A. W. (1976). Spiral structure as an explanation for the asymmetric brightness of Saturn's A ring. *Nature*, 264:344–345.

Colwell, J. E. (2003). Low velocity impacts into dust: results from the COLLIDE-2 microgravity experiment. *Icarus*, 164:188–196.

Colwell, J. E. and Esposito, L. W. (1992). Origins of the rings of Uranus and Neptune: I. Statistics of satellite disruptions. *J. Geophys. Res.*, 97:10227–10241.

Colwell, J. E. and Esposito, L. W. (1993). Origins of the rings of Uranus and Neptune: II. Initial conditions and ring moon populations. *J. Geophys. Res.*, 98:7387–7401.

Colwell, J. E. and Taylor, M. (1999). Low-velocity microgravity impact experiments into simulated regolith. *Icarus*, 138:241–248.

Colwell, J. E., Esposito, L. W., and Bundy, D. (2000). Fragmentation rates of small satellites in the outer solar system. *J. Geophys. Res.*, 105:17589–17599.

Colwell, J. E., Esposito, L. W., and Sremčević, M. (2006a). Self-gravity wakes in Saturn's A ring measured by stellar occultations from Cassini. *Geophys. Res. Lett.*, 33:L07201.1–L07201.4

Colwell, J. E., Esposito, L. W., Sremčević, M., Stewart, G. R., and McClintock, W. E. (2007). Self-gravity wakes and radial structure of Saturn's B ring. *Icarus*, 190:127–144.

Colwell, J. E., Esposito, L. W., and Stewart, G. R. (2006b). Density waves observed by Cassini stellar occultations as probes of Saturn's rings. In Mackwell, S. and Stansbery, E., editors, *37th Annual Lunar and Planetary Science Conference*, volume 37 of *Lunar and Planetary Inst. Technical Report*, p. 1221.

Colwell, J. E., Cooney, J. H., Esposito, L. W., and Sremčević, M. (2009). Density waves in Cassini UVIS stellar occultations. 1. The Cassini Division. *Icarus*, 200:574–580.

Cooke, M. L. (1991). *Saturn's Rings: Photometric Studies of the C Ring and Radial Variation in the Keeler Gap*. Ph.D. thesis, AA (Cornell University, Ithaca, NY).

Cuzzi, J. N. and Burns, J. A. (1988). Charged particle depletion surrounding Saturn's F ring – Evidence for a moonlet belt? *Icarus*, 74:284–324.

Cuzzi, J. N. and Durisen, R. H. (1990). Bombardment of planetary rings by meteoroids – General formulation and effects of Oort Cloud projectiles. *Icarus*, 84:467–501.

Cuzzi, J. N. and Scargle, J. D. (1985). Wavy edges suggest moonlet in Encke's gap. *Astrophys. J.*, 292:276–290.

Cuzzi, J. N., Burns, J. A., Durisen, R. H., and Hamill, P. M. (1979a). The vertical structure and thickness of Saturn's rings. *Nature*, 281:202–204.

Cuzzi, J. N., Durisen, R. H., Burns, J. A., and Hamill, P. (1979b). The vertical structure and thickness of Saturn's rings. *Icarus*, 38:54–68.

Cuzzi, J. N., Lissauer, J. J., and Shu, F. H. (1981). Density waves in Saturn's rings. *Nature*, 292:703–707.

Cuzzi, J. N., Lissauer, J. J., Esposito, L. W., Holberg, J. B., Marouf, E. A., Tyler, G. L., and Boischot, A. (1984). Saturn's rings: Properties and processes. In Greenberg, R. and Brahic, A., editors, *Planetary Rings*, pp. 73–199, Tucson Arizona, University of Arizona Press.

Daisaka, H. and Ida, S. (1999). Spatial structure and coherent motion in dense planetary rings induced by self-gravitational instability. *Earth Planets Space*, 51:1195–1213.

Daisaka, H., Tanaka, H., and Ida, S. (2001). Viscosity in a dense planetary ring with self-gravitating particles. *Icarus*, 154:296–312.

Davis, D. R., Weidenschilling, S. J., Chapman, C. R., and Greenberg, R. (1984). Saturn ring particles as dynamic ephemeral bodies. *Science*, 224:744–747.

Dermott, S. F., Murray, C. D., and Sinclair, A. T. (1980). The narrow rings Jupiter, Saturn and Uranus. *Nature*, 284:309–313.

Dilley, J. (1993). Energy loss in collisions of icy spheres: Loss mechanism and size-mass dependence. *Icarus*, 105:225–234.

Dilley, J. and Crawford, D. (1996). Mass dependence of energy loss in collisions of icy spheres: An experimental study. *J. Geophys. Res.*, 101:9267–9270.

Dobrovolskis, A. R. and Burns, J. A. (1980). Life near the Roche limit: Behavior of ejecta from satellites close to planets. *Icarus*, 42:422–441.

Dohnanyi, J. S. (1969). Collisional model of asteroids and their debris. *J. Geophys. Res.*, 74:2531–2554.

Dones, L., Cuzzi, J. N., and Showalter, M. R. (1993). Voyager Photometry of Saturn's A Ring. *Icarus*, 105:184–215.

Dones, L. and Porco, C. C. (1989). Spiral density wakes in Saturn's A ring? *Bull. American Astron. Soc.*, 21:929.

Duncan, M., Quinn, T., and Tremaine, S. (1989). The long-term evolution of orbits in the solar system – A mapping approach. *Icarus*, 82:402–418.

Dunn, D. E., Molnar, L. A., Niehof, J. T., de Pater, I., and Lissauer, J. J. (2004). Microwave observations of Saturn's rings: anisotropy in directly transmitted and scattered saturnian thermal emission. *Icarus*, 171:183–198.

Dunn, D. E., de Pater, I., and Molnar, L. A. (2007). Examining the wake structure in Saturn's rings from microwave observations over varying ring opening angles and wavelengths. *Icarus*, 192:56–76.

Durda, D. D., Greenberg, R., and Jedicke, R. (1998). Collisional models and scaling laws: A new interpretation of the shape of the main-belt asteroid size distribution. *Icarus*, 135:431–440.

Durisen, R. H. (1984). Transport effects due to particle erosion mechanisms. In Greenberg, R. and Brahic, A., editors, *Planetary Rings*, pages 416–446, Tucson Arizona, University of Arizona Press.

Durisen, R. H. (1995). An instability in planetary rings due to ballistic transport. *Icarus*, 115:66–85.

Durisen, R. H., Cramer, N. L., Murphy, B. W., Cuzzi, J. N., Mullikin, T. L., and Cederbloom, S. E. (1989). Ballistic transport in planetary ring systems due to particle erosion mechanisms. I – Theory, numerical methods, and illustrative examples. *Icarus*, 80:136–166.

Durisen, R. H., Bode, P. W., Cuzzi, J. N., Cederbloom, S. E., and Murphy, B. W. (1992). Ballistic transport in planetary ring systems due to particle erosion mechanisms. II – Theoretical models for Saturn's A- and B-ring inner edges. *Icarus*, 100:364–393.

Esposito, L. W. and Colwell, J. E. (1989). Creation of the Uranus rings and dust bands. *Nature*, 339:605–607.

Esposito, L. W., Borderies, N., Goldreich, P., Cuzzi, J. N., Holberg, J. B., Lane, A. L., Pomphrey, R. B., Terrile, R. J., Lissauer, J. J., Marouf, E. A., and Tyler, G. L. (1983). Eccentric ringlet in the Maxwell gap at 1.45 Saturn radii Multi-instrument Voyager observations. *Science*, 222:57–60.

AQ13 Esposito, L. W., Ocallaghan, M., Simmons, K. E., Hord, C. W., West, R. A., Lane, A. L., Pomphrey, R. B., Coffeen, D. L., and Sato, M. (1983). Voyager photopolarimeter stellar occultation of Saturn's rings. *J. Geophys. Res.*, 88:8643–8649.

Esposito, L. W., Cuzzi, J. N., Holberg, J. B., Marouf, E. A., Tyler, G. L., and Porco, C. C. (1984). Saturn's rings: Structure, dynamics, and particle properties. In Greenberg, R. and Brahic, A., editors, *Planetary Rings*, pages 463–544, Tucson Arizona, University of Arizona Press.

Esposito, L. W., Colwell, J. E., Larsen, K., McClintock, W. E., Stewart, A. I. F., Hallett, J. T., Shemansky, D. E., Ajello, J. M., Hansen, C. J., Hendrix, A. R., West, R. A., Keller, H.-U., Korth, A., Pryor, W. R., Reulke, R., and Yung, Y. L. (2005). Ultraviolet imaging spectroscopy shows an active saturnian system. *Science*, 307:1251–1255.

Esposito, L. W., Meinke, B. K., Colwell, J. E., Nicholson, P. D., and Hedman, M. M. (2008). Moonlets and clumps in Saturn's F ring. *Icarus*, 194:278–289.

Ferrari, C. and Brahic, A. (1997). A and clumps in the Encke division of Saturn's rings. *Planet. Space Sci.*, 45:1051–1067.

Ferrari, C., Galdemard, P., Lagage, P. O., Pantin, E., and Quoirin, C. (2005). Imaging Saturn's rings with CAMIRAS: thermal inertia of B and C rings. *Astron. Astrophys.*, 441:379–389.

Ferrari, C. and Leyrat, C. (2006). Thermal emission of spherical spinning ring particles: the standard model. *Astron. Astrophys.*, 447:745–760.

Ferrari, C., Brooks, S., Edgington, S., Leyrat, C., Pilorz, S., and Spilker, L. (2009). Structure of self-gravity wakes in Saturn's A ring as measured by Cassini CIRS. *Icarus*, 199:145–153.

Franklin, F. A., Cook, A. F., Barrey, R. T. F., Roff, C. A., Hunt, G. E., and de Rueda, H. B. (1987). Voyager observations of the azimuthal brightness variations in Saturn's rings. *Icarus*, 69:280–296.

French, R. G. and Nicholson, P. D. (2000). Saturn's rings II: Particle size inferred from stellar occultation data. *Icarus*, 145:502–523.

French, R. G., Nicholson, P. D., Cooke, M. L., Elliot, J. L., Matthews, K., Perkovic, O., Tollestrup, E., Harvey, P., Chanover, N. J., Clark, M. A., Dunham, E. W., Forrest, W., Harrington, J., Pipher, J., Brahic, A., Grenier, I., Roques, F., and Arndt, M. (1993). Geometry of the Saturn system from the 3 July 1989 occultation of 28 SGR and Voyager observations. *Icarus*, 103:163–214.

French, R. G., Salo, H., McGhee, C. A., and Dones, L. (2007). HST observations of azimuthal asymmetry in Saturn's rings. *Icarus*, 189:493–522.

Froidevaux, L. (1981). Saturn's rings: Infrared brightness variation with solar elevation. *Icarus*, 46:4–17.

Froidevaux, L., Matthews, K., and Neugebauer, G. (1981). Thermal response of Saturn's ring paricles during and after eclipse. *Icarus*, 46:18–26.

Goertz, C. K. (1984). Formation of Saturn's spokes. *Adv. Space Res.*, 4:137–141.

Goertz, C. K. and Morfill, G. (1988). A new instability of Saturn's rings. *Icarus*, 74:325–330.

Goertz, C. K., Morfill, G. E., Ip, W. H., Grün, E., and Havnes, O. (1986). Electromagnetic angular momentum transport in Saturn's rings. *Nature*, 320:141–143.

Goldreich, P. and Lynden-Bell, D. (1965). II. Spiral arms as sheared gravitational instabilities. *Mon. Not. R. Astron. Soc.*, 130:125–+ .

Goldreich, P. and Tremaine, S. (1978a). The excitation and evolution of density waves. *Astrophys. J.*, 222:850–858.

Goldreich, P. and Tremaine, S. (1978b). The formation of the Cassini division in Saturn's rings. *Icarus*, 34:240–253.

Goldreich, P. and Tremaine, S. (1978c). The velocity dispersion in Saturn's rings. *Icarus*, 34:227–239.

Goldreich, P. and Tremaine, S. (1979a). Precession of the epsilon ring of Uranus. *Astron. J.*, 84:1638–1641.

Goldreich, P. and Tremaine, S. (1979b). The excitation of density waves at the Lindblad and corotation resonances by an external potential. *Astrophys. J.*, 233:857–871.

Goldreich, P. and Tremaine, S. (1979c). Towards a theory for the Uranian rings. *Nature*, 277:97–99.

Goldreich, P. and Tremaine, S. (1980). Disk–satellite interactions. *Astrophys. J.*, 241:425–441.

Goldreich, P. and Tremaine, S. (1981). The origin of the eccentricities of the rings of Uranus. *Astrophys. J.*, 243:1062–1075.

Goldreich, P., Rappaport, N., and Sicardy, B. (1995). Single sided shepherding. *Icarus*, 118:414–417.

Gresh, D. L., Rosen, P. A., Tyler, G. L., and Lissauer, J. J. (1986). An analysis of bending waves in Saturn's rings using Voyager radio occultation data. *Icarus*, 68:481–502.

Gurnett, D. A., Grün, E., Gallagher, D., Kurth, W. S., and Scarf, F. L. (1983). Micron-sized particles detected near Saturn by the Voyager plasma wave instrument. *Icarus*, 53:236–254.

Hahn, J. M. (2007). The secular evolution of a close ring-satellite system: The excitation of spiral bending waves at a nearby gap edge. *Astrophys. J.*, 665:856–865.

Hahn, J. M. (2008). The secular evolution of a close ring-satellite system: the excitation of spiral density waves at a nearby gap edge. *Astrophys. J.*, 680:1569–1581.

Hahn, J. M., Spitale, J. N., and Porco, C. C. (2009). Dynamics of the sharp edges of broad planetary rings. *ArXiv e-prints, accepted by ApJ, 2009*. AQ14

Hämeen-Anttila, K. A. (1975). Statistical mechanics of Keplerian orbits. *Astrophys. Space Sci.*, 37:309–333.

Hämeen-Anttila, K. A. (1976). Statistical mechanics of Keplerian orbits. II – Dispersion in particle size. *Astrophys. Space Sci.*, 43:145–174.

Hämeen-Anttila, K. A. (1977a). Statistical mechanics of Keplerian orbits. III – Perturbations. *Astrophys. Space Sci.*, 46:133–154.

Hämeen-Anttila, K. A. (1977b). Statistical mechanics of Keplerian orbits. IV. *Astrophys. Space Sci.*, 51:429–437.

Hämeen-Anttila, K. A. (1978). An improved and generalized theory for the collisional evolution of Keplerian systems. *Astrophys. Space Sci.*, 58:477–519.

Hämeen-Anttila, K. A. (1981). Quasi-equilibrium in collisional systems. *Earth Moon Planets*, 25:477–506.

Hämeen-Anttila, K. A. (1982). Saturn's rings and bimodality of Keplerian systems. *Earth Moon Planets*, 26:171–196.

Hämeen-Anttila, K. A. (1984). Collisional theory of non-identical particles in a gravitational field. *Earth Moon Planets*, 31:271–299.

Hämeen-Anttila, K. A. and Salo, H. (1993). Generalized theory of impacts in particulate systems. *Earth Moon Planets*, 62:47–84.

Hänninen, J. and Salo, H. (1994). Collisional simulations of satellite Lindblad resonances. 2: Formation of narrow ringlets. *Icarus*, 108:325–346.

Hänninen, J. and Salo, H. (1995). Formation of isolated narrow ringlets by a single satellite. *Icarus*, 117:435–438.

Hatzes, A., Bridges, F., Lin, D., and Sachtjen, S. (1991). Coagulation of particles in Saturn's rings: Measurements of the cohesive force of water frost. *Icarus*, 89:113–121.

Hatzes, A., Bridges, F. G., and Lin, D. N. C. (1988). Collisional properties of ice spheres at low impact velocities. *Mon. Not. R. Astron. Soc.*, 231:1091–1115.

Hedman, M. M., Nicholson, P. D., Salo, H., Wallis, B. D., Buratti, B. J., Baines, K. H., Brown, R. H., and Clark, R. N. (2007). Self-gravity wake structures in Saturn's A ring revealed by Cassini VIMS. *Astron. J.*, 133:2624–2629.

Hertz, H. (1882). Über die beröhrung fester elastischer körper. *J. f. Reine Angew. Math.*, 92:156.

Higa, M., Arakawa, M., and Maeno, N. (1996). Measurements of restitution coefficients of ice at low temperatures. *Planet. Space Sci.*, 44:917–925.

Higa, M., Arakawa, M., and Maeno, N. (1998). Size dependence of restitution coefficients of ice in relation to collision strength. *Icarus*, 133:310–320.

Holberg, J. B. (1982). Identification of 1980S27 and 1980S26 resonances in Saturn's A ring. *Astron. J.*, 87:1416–1422.

Holberg, J. B., Forrester, W. T., and Lissauer, J. J. (1982). Identification of resonance features within the rings of Saturn. *Nature*, 297:115–120.

Horn, L. J. and Cuzzi, J. N. (1996). Characteristic wavelengths of irregular structure in Saturn's B ring. *Icarus*, 119:285–310.

Housen, K. R. and Holsapple, K. A. (1990). On the fragmentation of asteroids and planetary satellites. *Icarus*, 84:226–253.

Ip, W.-H. (1983). Collisional interactions of ring particles – The ballistic transport process. *Icarus*, 54:253–262.

Johnson, K., Kendall, K., and Roberts, A. (1971). Surface energy and the contact of elastic solids. *Proc. R. Soc. Lond. A*, 324:301.

Julian, W. H. and Toomre, A. (1966). Non-axisymmetric responses of differentially rotating disks of stars. *Astrophys. J.*, 146:810–827.

Karjalainen, R. (2007). Aggregate impacts in Saturn's rings. *Icarus*, 189:523–537.

Karjalainen, R. and Salo, H. (2004). Gravitational accretion of particles in Saturn's rings. *Icarus*, 172:328–348.

Kawata, Y. (1983). Infrared brightness temperature of Saturn's rings based on the inhomogeneous multilayer assumption. *Icarus*, 56:453–464.

Kevorkian, J. and Cole, J. (1996). *Multiple Scale and Singular Perturbation Methods*. Springer.

Kolvoord, R. A., Burns, J. A., and Showalter, M. R. (1990). Periodic features in Saturn's F ring – Evidence for nearby moonlets. *Nature*, 345:695–697.

Lane, A., Hord, C., West, R., Esposito, L., Coffeen, D., Sato, M., Simmons, K., Pomphrey, R., and Morris, R. (1982). Photopolarimetry from Voyager 2: Preliminary results on Saturn, Titan, and the rings. *Science*, 215:537–543.

Latter, H. N. and Ogilvie, G. I. (2006). The linear stability of dilute particulate rings. *Icarus*, 184:498–516.

Latter, H. N. and Ogilvie, G. I. (2008). Dense planetary rings and the viscous overstability. *Icarus*, 195:725–751.

Latter, H. N. and Ogilvie, G. I. (2009). The viscous overstability, nonlinear wavetrains, and finescale structure in dense planetary rings. *Icarus*, in press, March 2009. AQ15

Lewis, M. C. and Stewart, G. R. (2005). Expectations for Cassini observations of ring material with nearby moons. *Icarus*, 178:124–143.

Lewis, M. C. and Stewart, G. R. (2007). Collisional simulations of the F ring with Prometheus and Pandora. In *AAS/Division for Planetary Sciences Meeting Abstracts*, volume 39, page 26.08.

Lewis, M. C. and Stewart, G. R. (2009). Features around embedded moonlets in Saturn's rings: The role of self-Gravity and particle size distributions. *Icarus*, 199:387–412.

Leyrat, C., Ferrari, C., Charnoz, S., Decriemb, J., Spilker, L. J., and Pilorz, S. (2008). Spinning particles in Saturn's C ring from mid-infrared observations: Pre-Cassini mission results. *Icarus*, 196: 625–641.

Lightman, A. P. and Eardley, D. M. (1974). Black holes in binary systems: Instability of disk accretion. *Astrophys. J. Lett.*, 187:L1+ . AQ16

Lin, D. N. C. and Bodenheimer, P. (1981). On the stability of Saturn's rings. *Astrophys. J. Lett.*, 248:L83–L86.

Lissauer, J. J. (1984). Ballistic transport in Saturn's rings – an analytic theory. *Icarus*, 57:63–71.

Lissauer, J. J. (1985). Bending waves and the structure of Saturn's rings. *Icarus*, 62:433–447.

Lissauer, J. J., Shu, F. H., and Cuzzi, J. N. (1981). Moonlets in Saturn's rings. *Nature*, 292:707–711.

Lissauer, J. J., Goldreich, P., and Tremaine, S. (1985). Evolution of the Janus-Epimetheus coorbital resonance due to torques from Saturn's rings. *Icarus*, 64:425–434.

Longaretti, P.-Y. (1989). Saturn's main ring particle size distribution: An analytic approach. *Icarus*, 81:51–73.

Longaretti, P.-Y. and Borderies, N. (1986). Nonlinear study of the Mimas 5:3 density wave. *Icarus*, 67:211–223.

Longaretti, P.-Y. and Rappaport, N. (1995). Viscous overstabilities in dense narrow planetary rings. *Icarus*, 116:376–396.

Lukkari, J. (1981). Collisional amplification of density fluctuations in Saturn's rings. *Nature*, 292:433–435.

Lumme, K. and Irvine, W. M. (1976). Azimuthal brightness variations of Saturn's rings. *Astrophys. J. Lett.*, 204:L55–L57.

Lynden-Bell, D. and Kalnajs, A. (1972). On the generating mechanism of spiral structure. *Mon. Not. R. Astron. Soc.*, 157:1–30.

Marouf, E., Rappaport, N., French, R., McGhee, C., and Anabtawi, A. (2006). Azimuthal variability of radial structure of Saturn's rings observed by Cassini radio occultations. In *36th COSPAR Scientific Assembly*, volume 36 of *COSPAR, Plenary Meeting*, pages 2806–+.

Marouf, E. A., Tyler, G. L., Zebker, H. A., Simpson, R. A., and Eshleman, V. R. (1983). Particle size distributions in Saturn's rings from Voyager 1 radio occultation. *Icarus*, 54:189–211.

Masset, F. S. and Papaloizou, J. C. B. (2003). Runaway migration and the formation of hot Jupiters. *Astrophys. J.*, 588:494–508. AQ17

Melita, M. D. and Papaloizou, J. C. B. (2005). Resonantly forced eccentric ringlets: Relationships between surface density, resonance location, eccentricity and eccentricity-gradient. *Cel. Mech. Dyn. Astron.*, 91:151–171.

Morfill, G. E., Fechtig, H., Grün, E., and Goertz, C. K. (1983). Some consequences of meteoroid impacts on Saturn's rings. *Icarus*, 55:439–447.

Morishima, R. and Salo, H. (2004). Spin rates of small moonlets embedded in planetary rings: I. Three-body calculations. *Icarus*, 167: 330–346.

Morishima, R. and Salo, H. (2006). Simulations of dense planetary rings IV. Spinning self-gravitating particles with size distributions. *Icarus*, 181:272–291.

AQ18 Morishima, R., Salo, H., and Ohtsuki, K. (2009a). A Multi-layer model for thermal infrared emission of Saturn's rings: Basic formulation and implications for Earth-based observations. *Icarus*, in press.

AQ19 Morishima, R., Salo, H., Ohtsuki, K., Spilker, L., and Altobelli, N. (2009b). Dynamics and particle properties of Saturn's rings inferred from thermal infrared emission. Submitted to *Icarus*.

Mosqueira, I. (1996). Local simulations of perturbed dense planetary rings. *Icarus*, 122:128–152.

Mosqueira, I. and Estrada, P. R. (2002). Apse alignment of the Uranian rings. *Icarus*, 158:545–556.

Murray, C. D. (2007). F Ring objects and ring history. *AGU Fall Meeting Abstracts*.

Murray, C. D., Beurle, K., Cooper, N. J., Evans, M. W., Williams, G. A., and Charnoz, S. (2008). The determination of the structure of Saturn's F ring by nearby moonlets. *Nature*, 453:739–744.

Nakazawa, K. and Ida, S. (1988). Hill's approximation in the three-body problems. *Prog. Theor. Phys. Suppl.*, 96:167–174.

Nicholson, P. D., French, R. G., Campbell, D. B., Margot, J.-L., Nolan, M. C., Black, G. J., and Salo, H. J. (2005). Radar imaging of Saturn's rings. *Icarus*, 177:32–62.

Nicholson, P. D., Hedman, M. M., Clark, R. N., Showalter, M. R., Cruikshank, D. P., Cuzzi, J. N., Filacchione, G., Capaccioni, F., Cerroni, P., Hansen, G. B., Sicardy, B., Drossart, P., Brown, R. H., Buratti, B. J., Baines, K. H., and Coradini, A. (2008). A close look at Saturn's rings with Cassini VIMS. *Icarus*, 193:182–212.

Ohtsuki, K. (1992). Equilibrium velocities in planetary rings with low optical depth. *Icarus*, 95:265–282.

Ohtsuki, K. (1993). Capture probability of colliding planetesimals: Dynamical constraints on accretion of planets, satellites, and ring particles. *Icarus*, 106:228–246.

Ohtsuki, K. (1999). Evolution of particle velocity dispersion in a circumplanetary disk due to inelastic collisions and gravitational interactions. *Icarus*, 137:152–177.

Ohtsuki, K. (2004a). Formulation and analytic calculation for the spin angular momentum of a moonlet due to inelastic collisions of ring particles. *Earth Planets Space*, 56:909–919.

Ohtsuki, K. (2004b). On the rotation of a moonlet embedded in planetary rings. *Icarus*, 172:432–445.

Ohtsuki, K. (2005). Rotation rates of particles in Saturn's rings. *Astrophys. J.*, 626:L61–L64.

Ohtsuki, K. (2006a). Rotation rate and velocity dispersion of planetary ring particles with size distribution. I. Formulation and analytic calculation. *Icarus*, 183:373–383.

Ohtsuki, K. (2006b). Rotation rate and velocity dispersion of planetary ring particles with size distribution. II. Numerical simulation for gravitating particles. *Icarus*, 183:384–395.

Ohtsuki, K. and Emori, H. (2000). Local N-body simulations for the distribution and evolution of particle velocities in planetary rings. *Astron. J.*, 119:403–416.

Ohtsuki, K. and Toyama, D. (2005). Local N-body simulations for the rotation rates of particles in planetary rings. *Astron. J.*, 130:1302–1310.

Papaloizou, J. C. B. and Lin, D. N. C. (1988). On the pulsational overstability in narrowly confined viscous rings. *Astrophys. J.*, 331: 838–860.

Papaloizou, J. C. B. and Melita, M. D. (2005). Structuring eccentric-narrow planetary rings. *Icarus*, 175:435–451.

Papaloizou, J. C. B., Nelson, R. P., Kley, W., Masset, F. S., and Artymowicz, P. (2007). Disk-planet interactions during planet formation. In Reipurth, B., Jewitt, D., and Keil, K., editors, *Protostars and Planets V*, pages 655–668.

Petit, J. M. and Hénon, M. (1987). A numerical simulation of planetary rings. I. Binary encounters. *Astron. Astrophys.*, 173:389–404.

Petit, J. M. and Hénon, M. (1988). A numerical simulation of planetary rings. III – Mass segregation, ring confinement, and gap formation. *Astron. Astrophys.*, 199:343–356.

Porco, C., Nicholson, P. D., Borderies, N., Danielson, G. E., Goldreich, P., Holberg, J. B., and Lane, A. L. (1984). The eccentric Saturnian ringlets at 1.29 R(s) and 1.45 R(s). *Icarus*, 60:1–16.

Porco, C., Thomas, P., Weiss, J. W., and Richardson, D. C. (2007). Saturn's small inner satellites: Clues to their origins. *Science*, 318:1602–1607.

Porco, C. C., Baker, E., Barbara, J., Beurle, K., Brahic, A., Burns, J. A., Charnoz, S., Cooper, N., Dawson, D. D., Del Genio, A. D., Denk, T., Dones, L., Dyudina, U., Evans, M. W., Giese, B., Grazier, K., Helfenstein, P., Ingersoll, A. P., Jacobson, R. A., Johnson, T. V., McEwen, A., Murray, C. D., Neukum, G., Owen, W. M., Perry, J., Roatsch, T., Spitale, J., Squyres, S., Thomas, P., Tiscareno, M., Turtle, E., Vasavada, A. R., Veverka, J., Wagner, R., and West, R. (2005). Cassini Imaging Science: Initial results on Saturn's rings and small satellites. *Science*, 307:1226–1236.

Porco, C. C., Weiss, J. W., Richardson, D. C., Dones, L., Quinn, T., and Throop, H. (2008). Simulations of the dynamical and light-scattering behavior of Saturn's rings and the derivation of ring particle and disk properties. *Astron. J.*, 136:2172–2200.

Rappaport, N. (1998). Ring–ringlet interactions. *Icarus*, 132:36–42.

Rappaport, N. J., Longaretti, P.-Y., French, R. G., Marouf, E. A., and McGhee, C. A. (2009). A procedure to analyze nonlinear density waves in Saturn's rings using several occultation profiles. *Icarus*, 199:154–173.

Resibois, P. and DeLeener, M. (1977). *Classical Kinetic Theory of Fluids*. Wiley, New York.

Richardson, D. (1994). Tree code simulations of planetary rings. *Mon. Not. R. Astron. Soc.*, 269:493–511.

Robbins, S. J., Stewart, G. R., Lewis, M. C., Colwell, J. E., and Sremčević, M. (2009). Estimating the masses of Saturn's A and B rings from high-optical depth N-body simulations and stellar ocuultations. Submitted to *Icarus*. AQ20

Roche, R. A. (1847). Acad. des scis et Lettres de Montpelier. *Mem. de la Section des Sciences*, 1:243–262.

Rosen, P. A. and Lissauer, J. J. (1988). The Titan-1:0 nodal bending wave in Saturn's Ring C. *Science*, 241:690–694.

Rosen, P. A., Tyler, G. L., and Marouf, E. A. (1991a). Resonance structures in Saturn's rings probed by radio occultation. I – Methods and examples. *Icarus*, 93:3–24.

Rosen, P. A., Tyler, G. L., Marouf, E. A., and Lissauer, J. J. (1991b). Resonance structures in Saturn's rings probed by radio occultation. II – Results and interpretation. *Icarus*, 93:25–44.

Rubincam, D. P. (2006). Saturn's rings, the Yarkovsky effects, and the ring of fire. *Icarus*, 184:532–542.

Safronov, V. S. (1969). Evolution of the protoplanetary cloud and the formation of the earth and planets. *Nauka*, NASA TTF-677.

Salo, H. (1987a). Collisional evolution of rotating, non-identical particles. *Moon Planets*, 38:149–181.

Salo, H. (1987b). Numerical simulations of collisions between rotating particles. *Icarus*, 70:37–51.

Salo, H. (1991). Numerical simulations of dense collisional systems. *Icarus*, 92:367–368.

Salo, H. (1992a). Gravitational wakes in Saturn's rings. *Nature*, 359:619–621.

Salo, H. (1992b). Numerical simulations of dense collisional systems. II. Extended distribution of particle sizes. *Icarus*, 96:85–106.

Salo, H. (1995). Simulations of dense planetary rings. III. Self-gravitating identical particles. *Icarus*, 117:287–312.

Salo, H. (2001). Numerical simulations of the collisional dynamics of planetary rings. In Pöschel, T. and Luding, S., editors, *Granular Gases*, volume 564 of *Lecture Notes in Physics, Berlin Springer Verlag*, pages 330–349.

Salo, H. and Karjalainen, R. (2003). Photometric modeling of Saturn's rings. I. Monte Carlo method and the effect of nonzero volume filling factor. *Icarus*, 164:428–460.

Salo, H. and Lukkari, J. (1982). Self-gravitation in Saturn's rings. *Moon Planets*, 27:5–12.

Salo, H. J. and Schmidt, J. (2007). Release of impact-debris in perturbed ring regions: Dynamical and photometric simulations. In *Bulletin of the American Astronomical Society*, volume 38 of *Bulletin of the American Astronomical Society*, pages 425–+ .

AQ21 Salo, H. and Schmidt, J. (2009). N-body simulations of viscous instability of planetary rings. Submitted to *Icarus*.

Salo, H., Schmidt, J., and Spahn, F. (2001). Viscous overstability in Saturn's B ring: I. Direct simulations and mesurement of transport coefficients. *Icarus*, 153:295–315.

Salo, H., Karjalainen, R., and French, R. G. (2004). Photometric modeling of Saturn's rings. II. Azimuthal asymmetry in reflected and transmitted light. *Icarus*, 170:70–90.

Schmidt, J. and Salo, H. (2003). A weakly nonlinear model for viscous overstability in saturn's dense rings. *Phys. Rev. Lett.*, 90(6):061102.

Schmit, U. and Tscharnuter, W. (1995). A fluid dynamical treatment of the common action of self-gravitation, collisions, and rotation in Saturn's B-ring. *Icarus*, 115:304–319.

Schmit, U. and Tscharnuter, W. (1999). On the formation of the fine–scale structure in Saturn's B ring. *Icarus*, 138:173–187.

Schmidt, J., Salo, H., Spahn, F., and Petzschmann, O. (2001). Viscous overstability in Saturn's B ring: II. Hydrodynamic theory and comparison to simulations. *Icarus*, 153:316–331.

Seiß, M., Spahn, F., Sremčević, M., and Salo, H. (2005). Structures induced by small moonlets in satrun's rings: Implications for the cassini mission. *Geophys. Res. Lett.*, 32:doi:10.1029/2005GL022506.

Shan, L.-H. and Goertz, C. K. (1991). On the radial structure of Saturn's B ring. *Astrophys. J.*, 367:350–360.

AQ22 Shepelyansky, D. L., Pikovsky, A. S., Schmidt, J., and Spahn, F. (2009). Synchronization mechanism of sharp edges in rings of saturn. *Mon. Not. Royal Astron. Soc.* in press.

Showalter, M., Pollack, J., Ockert, M., Doyle, L., and Dalton, J. (1992). A photometric study of saturn's f ring. *Icarus*, 100:394–411.

Showalter, M. R. (1991). Visual detection of 1981S13, Saturn's eighteenth satellite, and its role in the Encke gap. *Nature*, 351:709–713.

Showalter, M. R. (1998). Detection of centimeter-sized meteoroid impact events in Saturn's F ring. *Science*, 282:1099–1102.

Showalter, M. R. and Burns, J. A. (1982). A numerical study of Saturn's F-ring. *Icarus*, 52:526–544.

Showalter, M. R. and Cuzzi, J. N. (1993). Seeing ghost: Photometry of Saturn's G ring. *Icarus*, 103:124–143.

Showalter, M. R. and Nicholson, P. D. (1990). Saturn's rings through a microscope: Particle size constraints from the Voyager PPS Scan. *Icarus*, 87:285–306.

Showalter, M. R., Cuzzi, J. N., Marouf, E. A., and Esposito, L. W. (1986). Satellite'wakes' and the orbit of the Encke Gap moonlet. *Icarus*, 66:297–323.

Shu, F. H. (1984). Waves in planetary rings. In Greenberg, R. and Brahic, A., editors, *Planetary Rings*, pages 513–561, Tucson Arizona, University of Arizona Press.

Shu, F. H., Cuzzi, J. N., and Lissauer, J. J. (1983). Bending waves in Saturn's rings. *Icarus*, 53:185–206.

Shu, F. H. and Stewart, G. R. (1985). The collisional dynamics of particulate disks. *Icarus*, 62:360–383.

Shu, F. H., Yuan, C., and Lissauer, J. J. (1985b). Nonlinear spiral density waves – an inviscid theory. *Astrophys. J.*, 291:356–376.

Shu, F. H., Dones, L., Lissauer, J. J., Yuan, C., and Cuzzi, J. N. (1985a). Nonlinear spiral density waves – Viscous damping. *Astrophys. J.*, 299:542–573.

Shukhman, I. (1984). Collisional dynamics of particles in Saturn's rings. *Sov. Astron.*, 28:574–585.

Smith, B. A., Soderblom, L., Batson, R., Bridges, P., Inge, J., Masursky, H., Shoemaker, E., Beebe, R., Boyce, J., Briggs, G., Bunker, A., Collins, S. A., Hansen, C. J., Johnson, T. V., Mitchell, J. L., Terrile, R. J., Cook, A. F., Cuzzi, J., Pollack, J. B., Danielson, G. E., Ingersoll, A., Davies, M. E., Hunt, G. E., Morrison, D., Owen, T., Sagan, C., Veverka, J., Strom, R., and Suomi, V. E. (1982). A new look at the Saturn system: The Voyager 2 images. *Science*, 215:505–537.

Smoluchowski, R. (1979). The rings of Jupiter, Saturn and Uranus. *Nature*, 280:377–378.

Spahn, F. and Sponholz, H. (1989). Existence of moonlets in Saturn's rings inferred from the optical depth profile. *Nature*, 339:607–608.

Spahn, F. and Sremčević, M. (2000). Density patterns induced by small moonlets in Saturn's rings? *Astron. Astrophys.*, 358:368–372.

Spahn, F. and Wiebicke, H. J. (1989). Long-term gravitational influence of moonlets in planetary rings. *Icarus*, 77:124–134.

Spahn, F., Greiner, J., and Schwarz, U. (1992a). Moonlets in Saturn's rings. *Advances Space Res.*, 12:141–147.

Spahn, F., Saar, A., Schmidt, S., and Schwarz, U. (1992b). The influence of various moonlets on the optical depth profile in planetary rings. *Icarus*, 100:143–153.

Spahn, F., Petit, J. M., and Bendjoya, P. (1993). The gravitational influence of satellite Pan on the radial distribution of ring-particles in the region of the Encke-division in Saturn's a ring. *Celest. Mech. Dyn. Astron.*, 57:391–402.

Spahn, F., Scholl, H., and Hertzsch, J. M. (1994). Structures in planetary rings caused by embedded moonlets. *Icarus*, 111:514–535.

Spahn, F., Schmidt, J., Petzschmann, O., and Salo, H. (2000). Stability analyses of a Keplerian disk of granular grains: influence of thermal diffusion. *Icarus*, 145:657–660.

Spilker, L., Ferrari, C., Cuzzi, J. N., Showalter, M., Pearl, J., and Wallis, B. (2003). Saturn's rings in the thermal infrared. *Planet. Space Sci.*, 51:929–935.

Spilker, L. J., Pilorz, S., Lane, A. L., Nelson, R. M., Pollard, B., and Russell, C. T. (2004). Saturn A ring surface mass densities from spiral density wave dispersion behavior. *Icarus*, 171:372–390.

Spilker, L. J., Pilorz, S. H., Wallis, B. D., Pearl, J. C., Cuzzi, J. N., Brooks, S. M., Altobelli, N., Edgington, S. G., Showalter, M., Flasar, F. M., Ferrari, C., and Leyrat, C. (2006). Cassini thermal observations of Saturn's main rings: Implications for particle rotation and vertical mixing. *Planet. Space Sci.*, 54:1167–1176.

Sremčević, M., Spahn, F., and Duschl, W. (2002). Density structures in perturbed thin cold disks. *Mon. Not. R. Astron. Soc.*, 337:1139–1152.

Sremčević, M., Schmidt, J., Salo, H., Seiß, M., Spahn, F., and Albers, N. (2007). A belt of moonlets in Saturn's A ring. *Nature*, 449:1019–1021.

Stewart, G. R. and Lewis, M. C. (2005). Why Saturn's F Ring Breaks up into Multiple Ringlets. In *Bulletin of the American Astronomical Society*, volume 37, page 528.

Stewart, G. R., Lin, D. N. C., and Bodenheimer, P. (1984). Collision-induced transport processes in planetary rings. In Greenberg, R. and Brahic, A., editors, *Planetary Rings*, pages 447–512, Tucson Arizona, University of Arizona Press.

Supulver, K. D., Bridges, F. G., and Lin, D. N. C. (1995). The coefficient of restitution of ice particles in glancing collisions: Experimental results for unfrosted surfaces. *Icarus*, 113:188–199.

Supulver, K. D., Bridges, F. G., Tiscareno, S., Lievore, J., and Lin, D. N. C. (1997). The sticking properties of water frost produced under various ambient conditions. *Icarus*, 129:539–554.

Tanaka, H., Inaba, S., and Nakazawa, K. (1996). Steady-state size distribution for the self-similar collision cascade. *Icarus*, 123:450–455.

Tanaka, H., Ohtsuki, K., and Daisaka, H. (2003). A new formulation of the viscosity in planetary rings. *Icarus*, 161:144–156.

Thompson, W. T., Lumme, K., Irvine, W. M., Baum, W. A., and Esposito, L. W. (1981). Saturn's rings – Azimuthal variations, phase curves, and radial profiles in four colors. *Icarus*, 46:187–200.

Thomson, F. S., Marouf, E. A., Tyler, G. L., French, R. G., and Rappoport, N. J. (2007). Periodic microstructure in Saturn's rings A and B. *Gephys. Res. Lett.*, 34:L24203.1–L24203.6

AQ23 Tiscareno, M. S., Burns, J. A., Hedman, M. M., Porco, C. C., Weiss, J. W., Murray, C. D., and Dones, L. (2006). Observation of "propellers" indicates 100-metre diameter moonlets reside in Saturn's a-ring. *Nature*, 440:648–650.

Tiscareno, M. S., Nicholson, P. D., Burns, J. A., Hedman, M. M., and Porco, C. C. (2006). Unravelling temporal variability in Saturn's spiral density waves: Results and predictions. *Astrophys. J. Lett.*, 651:L65–L68.

Tiscareno, M. S., Burns, J. A., Nicholson, P. D., Hedman, M. M., and Porco, C. C. (2007). Cassini imaging of Saturn's rings: II. A wavelet technique for analysis of density waves and other radial structure in the rings. *Icarus*, 189:14–34.

Tiscareno, M. S., Burns, J. A., Hedman, M. M., and Porco, C. C. (2008). The population of propellers in Saturn's A ring. *Astron. J.*, 135:1083–1091.

Toomre, A. (1964). On the gravitational stability of a disk of stars. *Astrophys. J.*, 139:1217–1238.

Toomre, A. (1981). What amplifies the spirals. In Fall, S. M. and Lynden-Bell, D., editors, *Structure and Evolution of Normal Galaxies*, pages 111–136.

Toomre, A. (1991). Gas-hungry Sc spirals. In Wielen, R., editor, *Dynamics and Interactions of Galaxies*, pages 292–303. Springer, Berlin.

Toomre, A. and Kalnajs, A. J. (1991). Spiral chaos in an orbiting patch. In Sundelius, B., editor, *Dynamics of Disc Galaxies*, pages 341–358. Almquist-Wiksell, Göteborg.

Tremaine, S. (2003). On the origin of irregular structure in Saturn's rings. *Astron. J.*, 125:894–901.

Trulsen, J. (1972). Numerical simulation of jetstreams,1: The three-dimensional case. *Astrophys. Space Sci.*, 17:241–262.

Tyler, G. L., Marouf, E. A., Simpson, R. A., Zebker, H. A., and Eshleman, V. R. (1983). The microwave opacity of Saturn's rings at wavelengths of 3.6 and 13 cm from Voyager 1 radio occultation. *Icarus*, 54:160–188.

Van Allen, J. A. (1983). Absorption of energetic protons by Saturn's ring G. *J. Geophys. Res.*, 88:6911–6918.

Vokrouhlický, D., Nesvorný, D., Dones, L., and Bottke, W. F. (2007). Thermal forces on planetary ring particles: application to the main system of Saturn. *Astron. Astrophys.*, 471:717–730.

Ward, W. R. (1981). On the radial structure of Saturn's rings. *Geophys. Res. Lett.*, 8:641–643.

Ward, W. R. and Cameron, A. G. W. (1978). Disc evolution within the Roche limit. In *Lunar and Planetary Institute Conference Abstracts*, volume 9 of *Lunar and Planetary Inst. Technical Report*, pages 1205–1207.

Weidenschilling, S. J., Chapman, C. R., Davis, D. R., and Greenberg, R. (1984). Ring particles: Collisional interactions and physical nature. In Greenberg, R. and Brahic, A., editors, *Planetary Rings*, pages 367–415, Tucson Arizona, University of Arizona Press.

Weidenschilling, S. J., Spaute, D., Davis, D. R., Marzari, F., and Ohtsuki, K. (1997). Accretional evolution of a planetesimal swarm. 2. The terrestrial zone. *Icarus*, 128:429–455.

Wetherill, G. W. and Stewart, G. R. (1993). Formation of planetary embryos: Effects of fragmentation, low relative velocity, and independent variation of eccentricity and inclination. *Icarus*, 106: 190–204.

Williams, D. and Wetherill, G. (1994). Size distribution of collisionally evolved asteroidal populations: Analytical solution for self-similar collision cascade. *Icarus*, 107:117–128.

Winter, O. C., Mour<006>o, D. C., Giuliatti Winter, S. M., Spahn, F., and da Cruz, C. (2007). Moonlets wandering on a leash-ring. *Mon. Not. R. Astron. Soc.*, 380:L54–L57.

Wisdom, J. (1980). The resonance overlap criterion and the onset of stochastic behavior in the restricted three-body problem. *Astron. J.*, 85:1122–1133.

Wisdom, J. and Tremaine, S. (1988). Local simulations of planetary rings. *Astron. J.*, 95:925–940.

Zebker, H. A., Marouf, E. A., and Tyler, G. L. (1985). Saturn's rings: Particle size distributions for thin layer models. *Icarus*, 64:531–548.

AUTHOR QUERIES

AQ1. Please provide department name for all authors if appropriate.
AQ2. Please provide the missing data.
AQ3. Please check if the sentence edited is correct.
AQ4. Please check if the inserted years are correct.
AQ5. Please check if the "?" deleted is correct.
AQ6. Please check if "model (2.2)" refers to Eq. 14.2.
AQ7. Part labels missing in figure. Please check.
AQ8. Please check the missing chapter no in figure citation.
AQ9. Please check the figure twelve propeller.
AQ10. Please specify the chapter number.
AQ11. Please check part label is missing in Figs. 14.17 and 14.18.
AQ12. Please check the place of opening paranthesis comes here is ok.
AQ13. "Esposito et al. 1983" is listed twice in the reference list. Please check and update them in the text citation also.
AQ14. Please provide further details.
AQ15. Please update the Ref. Latter and Ogilvie.
AQ16. Please provide the missing page number.
AQ17. Please update page range for Ref. Masset and Papaloizou
AQ18. Please update the Ref. Morishima et al. (2009a).
AQ19. Please update the Ref. Morishima et al. (2009b).
AQ20. Please update the Ref. Robbins et al.
AQ21. Please update the Ref. Salo and Schmidt, J. (2009).
AQ22. Please update the Ref. Shepelyansky (2009).
AQ23. "Tiscareno et al. 2006" is listed twice in the reference list. Please check and update in the text cross reference also